SURFACE METEOROLOGY AND TROPOSPHERIC CLOUD NEAR ROSS ISLAND IN ANTARCTICA

BEN JOLLY

A thesis submitted in partial fulfillment of the requirements for the Degree of Doctor of Philosophy in Physics

Department of Physics and Astronomy
College of Science
University of Canterbury

2016

ABSTRACT

This thesis presents a series of studies into cloud and surface weather conditions present near Ross Island in Antarctica to investigate local-scale meteorology in the area and explore connections with larger scale atmospheric processes. Technical work on the development of specialist, low-cost, portable weather stations (SNOWWEB) is described with results and corresponding analyses from two successful field seasons presented. Covering the Austral summers of 2013/14 and 2014/15, both deployments utilized 15 to 20 weather stations over areas in the order of hundreds of square kilometers. A third-party classification product derived from surface-level winds in ERA-Interim is used to provide synoptic context for these deployments and link results to an analysis of the combined radar (CloudSat) and lidar (CALIPSO) cloud product over the Ross Ice Shelf and southern Ross Sea.

Located at the north-western corner of the Ross Ice Shelf - due south of New Zealand - the topography around Ross Island is complex and substantial. This creates associated complex interactions with air flow in the region, particularly near the surface, as winds flowing north over the large and featureless ice shelf encounter the terrain. A large-scale network of automated weather stations (AWS) exists over the greater Ross Ice Shelf area with good coverage for mesoscale studies, however logistical constraints limit the number that can be deployed and maintained with a paucity of observations at the local scale. SNOWWEB is a system of low-cost weather stations easy to transport and very quick to deploy designed to augment existing AWS observations. Substantial technical development of SNOWWEB occurred during the course of this thesis, with improvements to physical design and wireless networking capabilities presented. SNOWWEB observations were found to match well with those from nearby existing AWS during two summer season deployments near Ross Island, with results from the network as a whole showing coherent spatial structure in wind, temperature, and pressure fields.

One SNOWWEB deployment covered the northern and western edges of White Island immediately south-east of Ross Island. Observations showed the interaction of a Ross Ice Shelf airstream (RAS) southerly storm event with the complex terrain of the deployment area, including a resulting small but intense gap wind. There was also a substantial dampening effect on the diurnal temperature cycle over the SNOWWEB network during the RAS that was not observed on the ice shelf. These observations were used for a case study validation of the Antarctic Mesoscale Predic-

tion System (AMPS). While AMPS forecast the larger scale winds and temperature well, it did not predict the gap wind or the suppression of the diurnal cycle.

A subsequent SNOWWEB deployment to the east of Ross and White islands over the Ross Ice Shelf for a longer duration allowed a more in-depth validation of AMPS conducted using self-organizing maps (SOMs). A combined SNOWWEB/AMPS dataset was created to train a single SOM which then classified each dataset independently, allowing a direct comparison between the classification time-series. AMPS was found to perform well during high wind periods, however problems arose during low wind periods when synoptic forcing was weak. AMPS was able to forecast the periods themselves well, but the actual wind speeds correlated very poorly at the local scale near complex terrain. Model grid length and initialization data were likely contributors given the scale and complexity of the area, though model grid length probably played a role as well. Known problems with cloud modeling and associated effects on the radiation budget would also have had an increased effect. The spatial density of SNOWWEB stations was extremely helpful when validating high resolution output from AMPS.

Finally, observations from the CloudSat and CALIPSO satellites were used to quantify cloud incidence over the Ross Ice Shelf and Ross Sea using a series of existing synoptic weather regimes (Coggins regimes) also used during earlier SNOWWEB analyses. Cloud appeared to be sensitive to moisture transport, with higher incidence during summer and autumn when sea ice extent is lower and open ocean closer to the study area. The western Ross Ice Shelf had the lowest cloud incidence, though a persistent cloud signature was found along the Transantarctic Mountains. Weather regimes associated with high surface wind speeds and intense synoptic forcing produced more cloud over the ice shelf with a link to the RAS, however periods of minimal forcing still resulted in substantial amounts of cloud at low altitudes. A link was also found between the RAS and low-level cloud over the Ross Sea during winter, likely a result of interactions with the Ross Ice Shelf Polynya.

Deputy Vice-Chancellor's Office
Postgraduate Office

UNIVERSITY OF CANTERBURY
Te Whare Wānanga o Waitaha
CHRISTCHURCH NEW ZEALAND

Co-authorship Form

This form is to accompany the submission of any thesis that contains research reported in co-authored work that has been published, accepted for publication, or submitted for publication. A copy of this form should be included for each co-authored work that is included in the thesis. Completed forms should be included at the front (after the thesis abstract) of each copy of the thesis submitted for examination and library deposit.

Please indicate the chapter/section/pages of this thesis that are extracted from co-authored work and provide details of the publication or submission from which the extract comes:

Chapter 4, A VALIDATION OF AMPS USING SELF-ORGANIZING MAPS AND SNOWWEB, *accepted by Monthly Weather Review, 2016 (Jolly et al., 2016).*

Please detail the nature and extent (%) of contribution by the candidate:

Ben Jolly was the lead author of this article; contribution 80%.

Certification by co-authors:

If there is more than one co-author then a single co-author can sign on behalf of all.

The undersigned certifies that:

- the above statement correctly reflects the nature and extent of the PhD candidate's contribution to this co-authored work;
- in cases where the candidate was the lead author of the co-authored work he or she wrote the text.

Name:	Signature:	Date:
ADRIAN MCDONALD		30/6/2016

Deputy Vice-Chancellor's Office
Postgraduate Office

UNIVERSITY OF CANTERBURY
Te Whare Wānanga o Waitaha
CHRISTCHURCH NEW ZEALAND

Co-authorship Form

This form is to accompany the submission of any thesis that contains research reported in co-authored work that has been published, accepted for publication, or submitted for publication. A copy of this form should be included for each co-authored work that is included in the thesis. Completed forms should be included at the front (after the thesis abstract) of each copy of the thesis submitted for examination and library deposit.

Please indicate the chapter/section/pages of this thesis that are extracted from co-authored work and provide details of the publication or submission from which the extract comes:

Chapter 2, SNOWWEB - A WIRELESS NETWORK OF ANTARCTIC WEATHER STATIONS, *based on work presented by Ben Jolly at the Eighth IEEE Workshop on Practical Issues in Building Sensor Network Applications 2013 (IEEE SenseApp 2013) and published in the peer-reviewed proceedings (Jolly et al., 2013).*

Please detail the nature and extent (%) of contribution by the candidate:

Ben Jolly was the lead author of this article; contribution 70%.

Certification by co-authors:

If there is more than one co-author then a single co-author can sign on behalf of all.

The undersigned certifies that:

- the above statement correctly reflects the nature and extent of the PhD candidate's contribution to this co-authored work;
- in cases where the candidate was the lead author of the co-authored work he or she wrote the text.

Name:	Signature:	Date:
ADRIAN MCDONALD		30/6/2016

ACKNOWLEDGMENTS

I would like to thank my supervisor, Adrian McDonald, for offering me this amazing opportunity and taking me on as a PhD student. I really appreciate the support, advice, and encouragement over the years. I also want to thank Andreas Willig and Wolfgang Rack, my associate supervisors, for their advice and encouragement at various stages throughout this work. Several other staff and students at the University of Canterbury also provided helpful input at various stages, most notably Jack Coggins, Peyman Zawar-Reza, and Marwan Katurgi, for which I am extremely grateful. Thank you also to those students who shared the Atmospheric Physics office with me and for all the varied and interesting discussions we had: Simon Parsons, Simon Fullick, Madeleine Smith, Fraser Dennison, Ethan Dale, and Alex Schuddeboom among others.

The technical staff at the Department of Physics and Astronomy, particularly Graeme Plank, Matthew Pannell, and Geoff Graham, played an integral role in designing and building the physical and electronic hardware of the SNOWWEB weather stations that provided much of the data used in this thesis. Their generous contribution to field work and helpful advice have also been very much appreciated. Thanks also go to those who traveled to Antarctica to help with station deployment and retrieval, all of whom worked hard under sometimes challenging conditions: Jack Coggins, Graeme Plank, Iman Soltanzadeh, Matt Pannell, Orlon Petterson, and Ethan Dale.

Special thanks go to John Cassano at the University of Colorado at Boulder for collaborating with us on several occasions, contributing advice toward the paper that constitutes Chapter 5. I had the privilege of spending a week on the Ross Ice Shelf with John, Melissa Nigro (also from UC Boulder), and 'Suz the Mountaineer' which provided many memorable moments. Thanks also to Matthew Lazzara from the University of Wisconsin at Madison for collaborating on the same paper and providing the AWS observational dataset (NSF grant numbers ANT-0944018, ANT-1245663, ANT-0943952, and ANT-1245737). I appreciate the work of the Byrd Polar Research Center at Ohio State University and the National Center for Atmospheric Research for developing, running, and providing output from AMPS (retrieved from both the NCAR/UCAR FTP server and the Earth System Grid). The free availability of data from these two significant research programs had a substantial impact on the work presented in this thesis.

This thesis would not have been possible without the Department of Physics and Astronomy at the University of Canterbury awarding me a departmental scholarship, nor without a postgraduate scholarship awarded by Antarctica New Zealand and funded by Kelly Tarlton's Sea Life Aquarium

- I am extremely grateful for the opportunity that both of these awards provided me. Additionally, work presented in Chapter 4 was partially supported by a grant from the New Zealand Antarctic Research Institute. I would like to thank Antarctica New Zealand for significant logistical support, as well as all the staff at Scott Base I have met and worked with during four seasons of research. Without their considerable support and advice the field work would not have progressed as well as it did (or sometimes at all), and the downtime on base would not have been nearly as entertaining.

I owe a debt of gratitude to my friends - many of whom I met at Canterbury and have already been mentioned - as well as my family for their support and advice, both academic and life, throughout this project. I particularly want to acknowledge my parents, Coby and Peter, who have both offered so much encouragement.

Most importantly, I want to thank my wife Anne-Maree. You were there before the beginning and supported me all the way, through times when others may have given up. You have read most of this thesis at least twice and your feedback and eye for detail have been greatly appreciated. Despite the broken promises and missed deadlines you still offered your love and support, and I will always be incredibly grateful for that.

CONTENTS

LIST OF FIGURES

LIST OF TABLES

ACRONYMS

AGL above ground level

AMPS Antarctic Mesoscale Prediction System

AMRC University of Wisconsin Antarctic Meteorological Research Center

AODV ad-hoc on-demand distance vector

API application program interface

APS application support

ASL above mean sea level

AWARE Atmospheric Radiation Measurement: West Antarctic Radiation Experiment

AWS automatic weather station

CALIOP Cloud-Aerosol LIdar with Orthogonal Polarization

CALIPSO Cloud-Aerosol Lidar and Infrared Pathfinder Satellite Observations

DJF December-January-February

EAIS East Antarctic Ice Sheet

ECMWF European Centre for Medium-Range Weather Forecasts

ESN environmental sensor network

IGY International Geophysical Year

ISCCP International Satellite Cloud Climatology Project

JJA June-July-August

MAM March-April-May

MISR Multi-angle Imaging SpectroRadiometer

MODIS MOderate Resolution Imaging Spectroradiometer

MSLP mean sea level pressure

NRMSD normalized root-mean-square difference

NWP numerical weather prediction

PGF pressure gradient force

RAS Ross Ice Shelf airstream

RIS Ross Ice Shelf

RMSD root-mean-square difference

RSLP relative sea level pressure

SLP sea level pressure

SNC strong northern cyclonic

SOM self-organizing map

SON September-October-November

SWS SNOWWEB weather station

TAM Transantarctic Mountains

USAP United States Antarctic Program

UTC coordinated universal time

UWAAWS University of Wisconsin-Madison Antarctic automatic weather station

VFM vertical feature mask

WAIS West Antarctic Ice Sheet

WNC weak northern cyclonic

WRF Weather Research and Forecasting

WS weak synoptic

WSC weak southern cyclonic

WSN wireless sensor network

1

INTRODUCTION

Antarctica, situated about the South Pole, is a permanently and almost completely ice-covered continent. During the austral winter, the continent is shrouded in darkness for months at a time, while in the summer the high levels of incoming solar radiation are predominantly reflected back into space by the high albedo of the frozen surface. These effects ensure temperatures are consistently well below freezing during the winter, and below (or in some northern places close to) freezing during the summer (King and Turner, 1997). The long, dark, winter aids in the generation of sea ice around the coast, a process that more than doubles the surface area of Antarctic ice during that time (Parkinson and Cavalieri, 2012). The are two major ice sheets that cover the Antarctic continent: the East Antarctic Ice Sheet (EAIS) and the West Antarctic Ice Sheet (WAIS) (Figure 1.1). These are extremely thick, up to two to four kilometers in places (King and Turner, 1997), and join to form a dome of ice that is offset from the South Pole but almost zonally symmetric. A dominant driver of Antarctic climate is the surface temperature inversion (Ball, 1960; Phillpot and Zillman, 1970; Connolley, 1996), formed when radiative heat loss from the surface exceeds incoming radiation (normally a combination of insolation and down-welling longwave radiation from clouds) (King and Turner, 1997). This reduces air temperatures at the surface so they become cooler than those further aloft, causing an anomalously positive vertical temperature gradient. As the air cools it becomes dense and negatively buoyant with two important effects: firstly it forms a very stable layer of the atmosphere that actively resists positive vertical displacement, and secondly, if this occurs over a slope, it creates a horizontal temperature gradient that encourages the air to flow down the slope - similar to water flowing down a hill. The wind that occurs as a result is commonly referred to as a 'katabatic' wind, and it dominates the surface wind regime of Antarctica (Parish and Bromwich, 1991, 1998; Parish and Cassano, 2003). This has a significant impact on global climate, with a net outflow at the surface level inducing a net inflow at higher altitudes (James, 1989; Parish, 1992; Parish and Bromwich, 1998) driving the polar circulation cell which has a large influence on the circumpolar trough - a band of mean low pressure in the Southern Ocean encircling Antarctica. Baroclinic instability at the border between the cold Antarctic air and

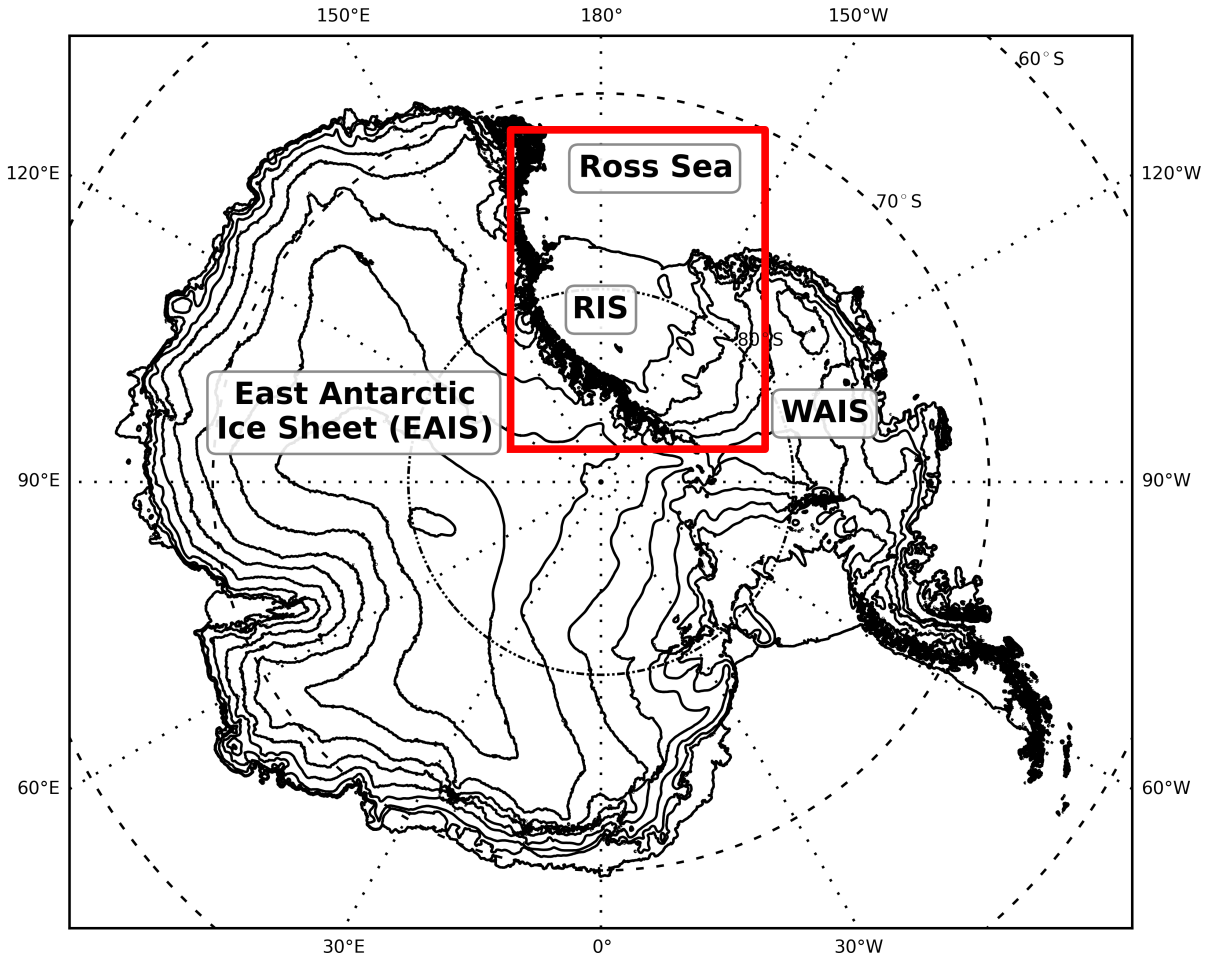

Figure 1.1: Antarctica, with the greater Ross Ice Shelf/Ross Sea region highlighted. Contour levels are 500 m.

warmer mid-latitude air is the main driver behind the significant level of storm activity in the southern hemisphere (King and Turner, 1997).

The Ross Ice Shelf (RIS) (Figure 1.2) is a thick and very large (487,000 km^2) sheet of floating and grounded permanent ice. Approximately 900 km wide at its northern edge, it flows from the Antarctic interior, fed by both the EAIS and WAIS, into the Ross Sea. Positioned due south of New Zealand between 77° and 86°S, it straddles the Anti-meridian (180°E/W) and is situated well within the Antarctic circle. Ross Island, located at the north-eastern corner of the RIS as highlighted in Figure 1.2 and depicted in Figure 1.3, features two major research stations that are staffed year-round and provide support for a significant number of researchers - Scott Base (New Zealand) and McMurdo Station (United States of America). The RIS is almost completely flat with most of it located below 150 m ASL. It is bordered by the Transantarctic Mountains (TAM), rising sharply to approximately 2 km ASL and forming a substantial barrier with the EAIS behind. The RIS is a significant confluence zone for katabatic winds from the EAIS and

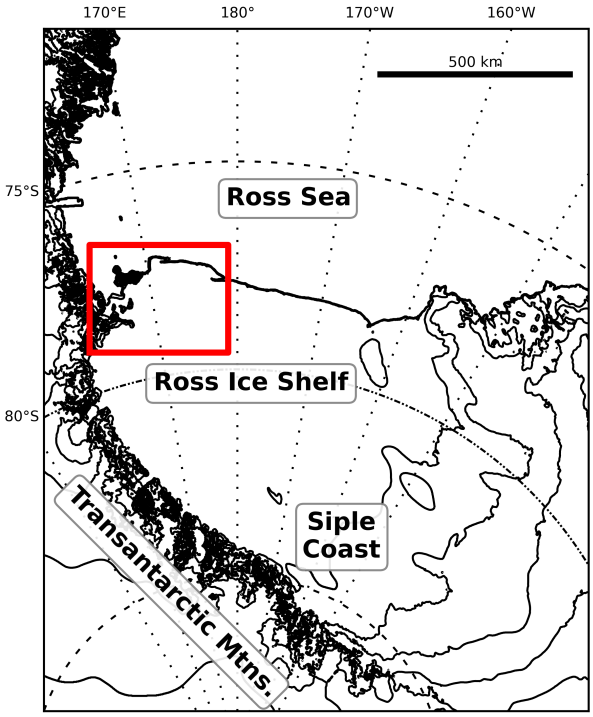

Figure 1.2: The Ross Ice Shelf (RIS) and adjacent Ross Sea (enlargement for box in Figure 1.1). Ross Island is visible at the north-western edge of the RIS at approximately 77.5°S, 167.5°E. Contour levels are 100 m until 500 m ASL, then 500 m.

WAIS (Parish and Bromwich, 1987; Bromwich, 1989; Breckenridge et al., 1993; Bromwich et al., 1994; Bromwich and Liu, 1996) which help to drive a significant low-level air stream known as the Ross Ice Shelf airstream (RAS) (Parish et al., 2006). This is an extreme variation of the nearly ubiquitous southerly wind regime that exists over the RIS (Savage and Stearns, 1985; Parish et al., 2006; Seefeldt and Cassano, 2012), with sustained high southerly winds flowing from the base of the roughly triangular ice shelf out into the Ross Sea. The RAS has a significant impact of human activity at both Scott Base and McMurdo Station on Ross Island, manifesting as a large southerly storm with high winds, blowing snow, and often low cloud that is capable of bringing most outdoor operations to a halt for days at a time.

Another significant driver for RAS events is the barrier wind regime (Schwerdtfeger, 1984) along the TAM, created by synoptic cyclones in the Ross Sea directing air toward the TAM that is unable to overcome the barrier (Seefeldt and Cassano, 2012; Coggins et al., 2014; Nigro and Cassano, 2014a). Instead, the air 'piles up' and creates a high-pressure zone at the foot of the TAM, with a corresponding pressure gradient force (PGF) directed perpendicular to and away from the mountains inducing approximately geostrophic barrier-parallel flow (a 'barrier wind'). Nigro and Cassano (2014a) provide further analysis of RAS events that shows the barrier-parallel flow is sometimes induced not by a cyclone in the Ross Sea but by the difference in potential temperature

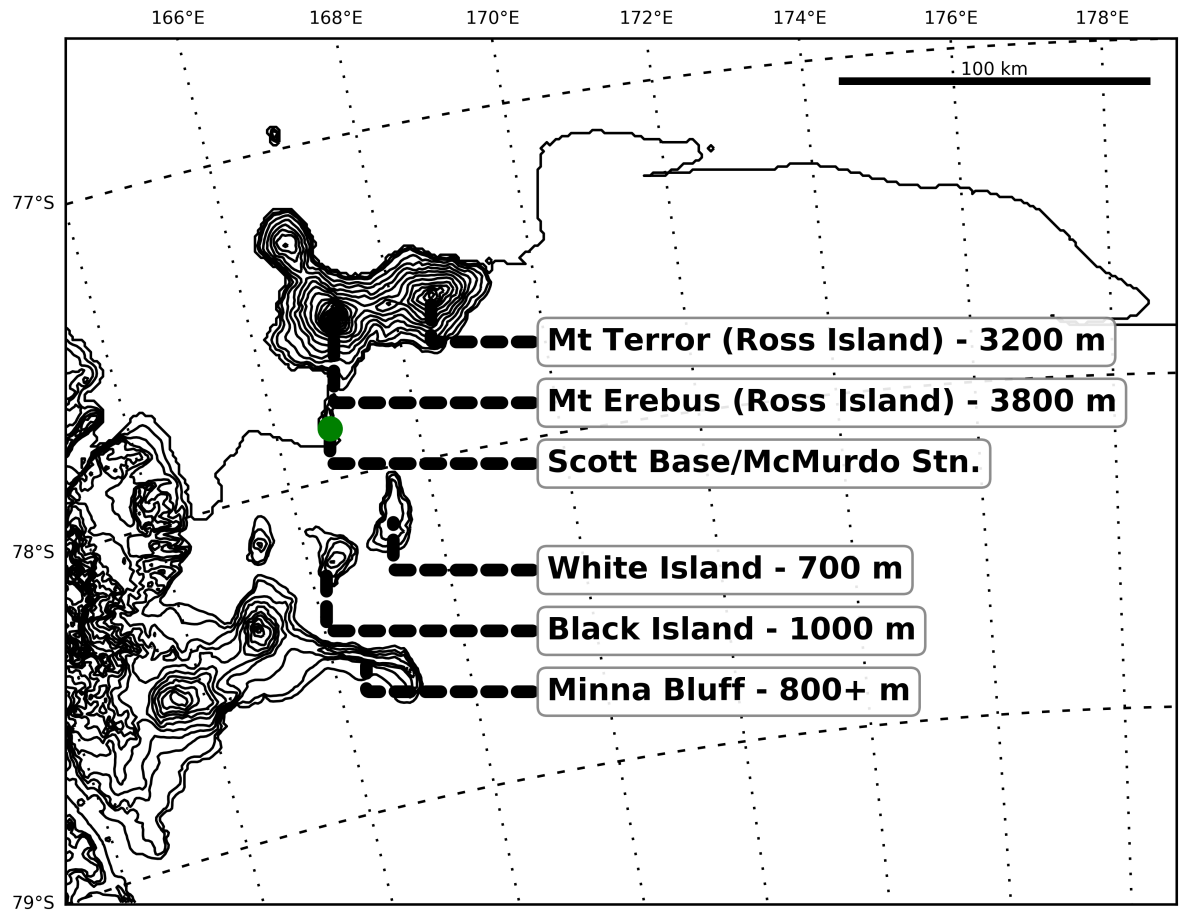

Figure 1.3: Ross Island and surrounds (enlargement for box in Figure 1.1) including White Island, Black Island, and Minna Bluff - maximum heights of each labeled feature are included in brackets. Scott Base (NZ) and McMurdo Station (USA) are located at the tip of Hut Point Peninsula on Ross Island (marked with green dot). Contours are at 0 m, 100 m, and 250 m followed by 250 m increments.

between the EAIS behind the TAM, and the RIS, adding a major source of forcing more consistent than the Ross Sea cyclones.

The topography of the greater Ross Island area in Figure 1.3 produces interesting effects as it interacts with the southerly winds, and RAS events, as they move northward along the TAM. Minna Bluff to the south is the first point of contact, rising almost vertically to at least 800 m above the ice shelf it often acts to shelter White Island (~700 m ASL), Black Island (~1000 m ASL), and Ross Island (between 1500 and 3800 m ASL) from the oncoming wind (Savage and Stearns, 1985; Seefeldt et al., 2003; Monaghan et al., 2005). Sometimes, however, the southerly winds are strong enough to overcome the barrier of Minna Bluff resulting in very high winds at Black Island and often Scott Base and McMurdo Station, with downslope windstorms producing damaging wind speeds (Powers, 2007; Steinhoff et al., 2008; Chenoli et al., 2012). Beyond Minna Bluff, White

Island and Black Island provide some additional blocking for winds with a more substantial easterly component, though the gap between them (known as 'Herbie Alley') is known for high wind speeds. Ross Island is known to provide a significant source of blocking for most wind that reaches it, with 'Windless Bight' on its southern edge marking the persistent windward high pressure stagnation zone that develops during southerly winds (O'Connor and Bromwich, 1988; Seefeldt et al., 2003; Monaghan et al., 2005; Coggins et al., 2013, among others). The diversion of air around Ross Island is responsible for the prevailing north-easterly wind at Scott Base and McMurdo Station, where winds already slowed by interaction with the stagnation zone get turned again by the relatively low-profile Hut Point Peninsula. It is worth noting that, at almost every other location in the vicinity bar Windless Bight and parts of Hut Point Peninsula, the prevailing wind direction is southerly.

Antarctic clouds play an important role in the surface climate, contributing significant amounts of down-welling long-wave radiation that warm the surface (King and Turner, 1997) and block the formation of temperature inversions. For a continent whose mean wind field is defined by katabatic flows driven by inversions, clouds can have a large impact on the climate (Bromwich et al., 2012; Lawson and Gettelman, 2014). Due to the lack of liquid water over most of the Antarctic continent, advection and moisture transport plays a large role in the moisture budget of the atmosphere over Antarctica (Tietäväinen and Vihma, 2008), with seasonal links between cloud and sea ice and therefore moisture availability (Comiso and Stock, 2001). Cloud composition also plays an important role in the radiation budget over Antarctica and the Southern Ocean, with ice clouds reflecting and absorbing less solar radiation (Scott and Lubin, 2014; Lawson and Gettelman, 2014). Despite their importance, there is a lack of knowledge when it comes to cloud over Antarctica and the Southern Ocean (Haynes et al., 2011; Bromwich et al., 2012; Chubb et al., 2013; Lawson and Gettelman, 2014) with ground- and air-based studies expensive and logistically difficult to conduct (Lachlan-Cope, 2010).

Satellite observations provide a method of expanding knowledge of Antarctic cloud without relying on model or reanalysis data, with three of the NASA A-Train satellites providing particularly popular datasets - CloudSat (Marchand et al., 2008), CALIPSO (Liu et al., 2009), and Terra (MODIS/MISR). CloudSat and CALIPSO (Cloud-Aerosol Lidar and Infrared Pathfinder Satellite Observations) have 'active' sensors, where the sensor-platform emits radio-waves (CloudSat) or laser pulses (CALIPSO) and measures the reflected returns as points along a track, while MODIS features passive multi-spectral imaging sensors that capture a range of bands from visible light to thermal infra-red as two-dimensional imagery. Some difficulties exist distinguishing cloud over snow and ice with MODIS and other passive satellite sensors (Frey et al., 2008), however the active sensors on both CloudSat and CALIPSO are able to determine the altitude of observed features which is very useful for cloud detection. These sensors have their own drawbacks, for ex-

ample the radar on CloudSat experiences difficulties with ground clutter close to surface level and the lidar on CALIPSO is sometimes unable to penetrate higher-level thick clouds to see beneath them. To mitigate these, a combined product has been produced from both satellite platforms (2B-GEOPROF-LIDAR - Mace et al., 2009; Mace and Zhang, 2014), using the lidar on CALIPSO to increase the resolving power of the radar on CloudSat and sense un-obscured and low-level cloud with greater accuracy while still retaining penetration ability. Data from CloudSat, CALIPSO, and MODIS has been used over the Antarctic, with Adhikari et al. (2012) conducting a seasonal analysis over the entire continent plus the Southern Ocean. They found an increase of cloud during summer, mainly driven by low-level cloud, with the Amundsen/Bellingshausen Sea experiencing the highest cloud incidence and the Antarctic Plateau the lowest.

Physical observations of any sort in Antarctica are considerably more difficult to undertake than in most parts of the world, with frequent high winds that persist for days to weeks, very low temperatures, ice riming, and blowing snow providing significant challenges. Meteorological observations are arguably harder again given instrumentation must be fully exposed to the elements by definition. The only settlements on the continent are (relatively small) research bases that are spread sporadically over a very large area, typically near the coastline. A complete lack of transport infrastructure makes most observation stations reachable only by air, ship, or multiple days of ground travel. The travel range of helicopters is also a limiting factor, meaning that many remote stations must be visited by fixed-wing aircraft (Lazzara et al., 2012) - further limiting deployment locations as sufficient landing space must be found (and obstacles such as *sastrugi* can make otherwise flat areas unsuitable). As a result, the number of permanent observation stations is low given the size of the continent. It was during the International Geophysical Year (IGY) of 1957-58 activities, where several permanently manned bases were established, that long term meteorological monitoring began. It was around this time that the first automatic weather station (AWS) was being tested in Antarctica, part of what would expand to the University of Wisconsin-Madison Antarctic automatic weather station (UWAAWS) network (Lazzara et al., 2012). Currently acquiring observations from almost 70 AWS, the UWAAWS network is the largest and most comprehensive single dataset of meteorological observations available in Antarctica. Maintaining and expanding this network is logistically challenging, with most stations requiring annual or bi-annual visits to check, maintain, and often raise equipment (due to snow accumulation), however the resulting dataset is extremely valuable as the lone source of long-term distributed observations for many areas including the RIS. Almost every study referenced in this document that incorporates surface-level data in the general RIS uses data from the UWAAWS network.

Due to the difficulties of building and maintaining a network of AWS, spatial coverage even over the RIS (close to the Ross Island research bases) is still not optimal. Observations beyond ground-level are even more limited, with a single 30 m tower (Alexander Tall Tower - see Lazzara

et al., 2012) and regular radiosonde launches from McMurdo Station the only consistent sources (some manned and un-manned aerial measurements are made on a campaign basis). To fill the void in available physical observations, model and reanalysis outputs are often used. A very popular model dataset is output from the Antarctic Mesoscale Prediction System (AMPS) (Powers et al., 2012) - a numerical weather prediction (NWP) system running twice-daily forecasts for the forecasters at McMurdo Station. AMPS currently uses the Weather Research and Forecasting (WRF) model with specific polar improvements (Polar WRF) developed by the Polar Meteorology Group of the Byrd Polar Research Center at Ohio State University. The base model domain covers Antarctica, the Southern Ocean, and some areas further north including New Zealand, part of Australia, the southern tip of South America and the southern tip of South Africa with a 30 km grid spacing and 61 vertical levels (plus 60 half-levels). Further nested domains exist, including a 10 km grid over the Antarctic continent down to a 1.1 km grid over a ~600 x ~700 km area centered on Black Island (Fig. 1.3)(Manning, 2015). AMPS output is popular with researchers as it comprises a rich dataset that is known to be reasonably accurate at the synoptic- and meso-scales (Nigro et al., 2011; Bromwich et al., 2013) that is freely available.

The ERA-Interim reanalysis (Dee et al., 2011) is another popular data source that is reliable over the Ross Sea and RIS (Bracegirdle, 2013; Coggins et al., 2014). It uses global-scale forecast models to process multiple observation sources (local and remotely-sensed), producing a gridded output over the entire globe. The available grid spacing is low at 0.75° x 0.75°with a temporal resolution of 3-hourly (surface) or 6-hourly (upper-atmosphere) which limits it applicability to small-scale studies, however at larger scales it is an excellent data source. Coggins et al. (2014) used 33 years of 10 m wind output from the ERA-Interim reanalysis to produce a synoptic-scale climatology of surface conditions the RIS/Ross Sea region. They defined 20 classes using the *k*-means clustering technique that were grouped into 5 regimes that broadly represent varying extremes of wind speed and pressure gradient over the area. This output was subsequently used by Coggins and McDonald (2015) to successfully quantify the effects of the Amundsen Sea Low - an area of low mean atmospheric pressure over the Southern Ocean (Raphael et al., 2016) - on surface winds over the RIS and Ross Sea.

An alternative cluster method to *k*-means is the self-organizing map (SOM) - a form of artificial neural network (Kohonen, 1990). SOMs work by defining a two-dimensional space consisting of one-dimensional 'nodes', where each node may be a flattened multi-dimensional array. The SOM space is then trained by an unsupervised learning algorithm that modifies the nodes to best fit an input training dataset. The result being a set of 'classes' that can be used to describe the training dataset. The main advantage of the SOM approach is that it is objective and repeatable, even when the SOM space is randomly initialized. SOMs are very effective tools for developing climatologies (Hewitson and Crane, 2002; Reusch et al., 2005; Sheridan and Lee, 2011) and investigating weather

patterns and extremes (Seefeldt and Cassano, 2012; Nigro and Cassano, 2014a; Cassano et al., 2015). Classification schemes in general provide a promising approach to model validation, where model performance can be assessed by weather pattern instead of by year, season, or case study. Nigro et al. (2011) (SOMs) and Coggins et al. (2014) (*k*-means clustering) both showed that it is possible that large biases may be overlooked by using a more traditional seasonal or annual approach compared to weather patterns.

The overall aim of this thesis is *to investigate local-scale meteorology near Ross Island and explore connections with larger scale atmospheric processes*. An essential tool for obtaining *in-situ* observations to inform this investigation is the SNOWWEB weather station (SWS) (Coggins et al., 2013; Jolly et al., 2013), a low-cost weather station designed to withstand Antarctic conditions while being easy to deploy and retrieve in large numbers. To achieve the aim, four objectives were defined to guide research work and technical development:

1. to further development of the SNOWWEB system of weather stations, such that they may be deployed over a large area with good wireless communication;
2. to use SNOWWEB to investigate surface-level conditions in the complex terrain near Ross Island;
3. to validate the finest model grid output of AMPS using high resolution observational datasets created by SNOWWEB deployments;
4. and to determine three-dimensional cloud structure over the RIS during given surface conditions so as to better understand the weather as experienced on the ground.

Chapter 2 covers Objective 1, detailing the technical aspects of the station design and documenting the development process. It also presents technical results from three deployments over three Antarctic summer seasons. The first season was a 'proof-of-concept' of a new generation of hardware and software following on from the previous work of Coggins et al. (2013) and, while technically successful, did not produce enough data for physical analysis. The author's primary technical role within the SNOWWEB project was the design and implementation of new station firmware. Analysis of observations from the second season are presented in Chapter 3, along with corresponding analysis of AMPS data over the same time period to meet Objective 2. The third season was the most ambitious and ultimately the most successful, with a detailed analysis and comparison with AMPS output using a novel application of SOMs presented in Chapter 4 covering Objective 3. This chapter is also an 'accepted' (at time of writing) paper in the American Meteorological Society journal 'Monthly Weather Review' (Jolly et al., 2016). Chapter 5 steps back from Ross Island and incorporates a wider view of the RIS to cover Objective 4, with analysis of the combined 2B-GEOPROF-LIDAR dataset from the CloudSat and Cloud-Aerosol Lidar and Infrared Pathfinder Satellite Observations (CALIPSO) satellites. A data-source present over all three chapters is a clas-

sification time-series of ERA-Interim 10 m winds created by Coggins et al. (2014), extended by the original author to cover the deployment periods presented in this thesis. The regimes are used in chapters 3 and 4 to bring a well-summarized synoptic-scale perspective to otherwise local (lower-meso-) scale studies, and in Chapter 5 to create a common reference point to which the results of the cloud analysis can be tied, increasing the relevance of all three chapters to one another. All chapters are formatted as paper drafts, with extended introductions containing relevant literature and previous work specific to that chapter.

2

SNOWWEB - A WIRELESS NETWORK OF ANTARCTIC WEATHER STATIONS

INTRODUCTION

The harsh weather and remote nature of Antarctica creates challenging conditions for collecting *in situ* observations of any nature. The two most common tools for observing atmospheric conditions in Antarctica are currently remote sensing via satellite, and the automatic weather station (AWS). Satellite-based remote sensing is effective for specific properties such as cloud cover and surface temperature, however is unable to measure wind vectors and cannot provide the continuous data records that AWS are capable of. While AWS are effective at providing continuous observations of any number of surface conditions, they provide only point data with large numbers required to obtain adequate spatial coverage. Due to high logistical costs there are currently fewer than 200 AWS covering the entirety of Antarctica - an area approximately half again as big as the entire United States of America - the majority of which are incorporated into the University of Wisconsin-Madison Antarctic automatic weather station (UWAAWS) dataset (Lazzara et al., 2012). These AWS consist of a robust collection of environmental sensors mounted on a guyed mast and powered by a combination of solar panels and large battery banks. Each station records observations locally then relay them via satellite modem to a central server. Stations are typically permanent and often provide a data record over many years. While records are mostly contiguous, many stations experience occasional outages as maintenance visits are sometimes years apart and the environmental challenges are significant.

The SNOWWEB project (Coggins et al., 2013) began six years ago in an effort to create a reusable network of weather stations that could be used to temporarily 'fill in' holes in the larger UWAAWS network on a campaign-basis to further investigate surface-level atmospheric dynamics. The driving design goals of SNOWWEB are to create weather stations that are easy to deploy and retrieve, light-weight for easy air transport, low cost, able to communicate wirelessly with a base station in real time, and robust enough to withstand Antarctic weather conditions. Many SNOWWEB sta-

tions should be able to be deployed to an area of tens to hundreds of square kilometers to gather large amounts of meteorological data in high spatial and temporal resolution and report it back to a base station in real time. Since inception, SNOWWEB hardware has been tested in Antarctica multiple times which has allowed the design to be continuously improved and as a result it has become increasingly robust. SNOWWEB is now in its third major generation with an additional two minor revisions, and all design goals mentioned above have been met.

A significant difficulty with developing devices that will be deployed to Antarctica is that, once they are deployed, there is very little chance to re-visit them until they are retrieved at the end of the field campaign. Typically a team will fly to Antarctica, deploy equipment to the field over a period of a week or more, then return home leaving the stations for months at a time with no chance of personally revisiting them in the event of failure. Even if a station is within 20-30km of a research base it may be impossible for base support personnel to visit the station within a reasonable time-frame due to weather conditions. Nonetheless, the ability to monitor the network operation in real-time is a pre-requisite to have any chance to carry out repair or maintenance operations while the measurement campaign is on-going.

Given the enormous expense of mounting a field campaign, it is critical that equipment performs as expected. To ensure this happens, it is important to assess achievable station and transmission reliability through experiments in the field so that choices of equipment and network deployment in future campaigns can be better informed. This chapter addresses the physical and firmware design aspects of SNOWWEB, with chapters 3 and 4 presenting the data collected over two field seasons, 2013/14 and 2014/15.

RELATED PROJECTS

The concept of using the wireless sensor network (WSN) for environmental monitoring has been one of the key drivers in their genesis (Corke et al., 2010; Hart and Martinez, 2006; Martinez et al., 2006, 2004; Barrenetxea et al., 2008; Talzi et al., 2007). This process has gained traction after the ratification of the IEEE 802.15.4 standard in 2003 - newer versions have appeared in 2006 and 2011 (IEEE, 2011) - and of the complementary ZigBee (Organization, 2006) standard in 2006. The commercial availability of 'plug and play' type components like the XBee module (Inc, 2010) has made it increasingly easier to deploy sensor networking technology (Liu et al., 2012).

It is worth noting, at this point, the distinction between a WSN and an environmental sensor network (ESN). An ESN is a network of sensors that may be, but not necessarily are, wirelessly connected to form a WSN. Examples of different types of ESN include Antarctic ozone monitoring stations with no wireless connectivity (Bauguitte et al., 2009), UWAAWS with periodic

connectivity via satellite modem (Lazzara et al., 2012), GLACSWEB glacial monitoring stations with periodic local wireless connectivity (Martinez et al., 2004), 'freewave'-equipped UWAAWS (Lazzara et al., 2012), SensorScope (Barrenetxea et al., 2008), and PermaSense (Talzi et al., 2007) that connect short range wireless mesh networks to remote servers via a GPRS-enabled sink, and animal monitoring systems with unpredictable sporadic connectivity between mobile units and static base stations (Corke et al., 2010; Juang et al., 2002). Each example comes with its own set of unique challenges, power requirements and operating costs.

The work of Bauguitte et al. (2009) and Lazzara et al. (2012) offers valuable insights into power requirements versus power availability over the Antarctic winter months for real-world scenarios. When deploying equipment over winter there are often minimum temperature requirements for scientific instruments, electronics and batteries (particularly when charging) which require the use of heaters, a very expensive exercise with regard to power consumption. Both networks rely on extensive banks of lead-acid batteries (up to 2.4 kWh for Bauguitte et al. (2009)) to supply sufficient power through the dark winter months which are recharged via solar panels over the summer months. In addition, the stations described in Bauguitte et al. (2009) utilise small vertical-axis wind turbines to augment the battery banks during winter. However, the overall energy contribution of these turbines varies greatly between stations and is dependent on wind conditions at each site. Additionally, the turbines used had relatively low output ratings (5 W) compared to station power draw (up to 5 W when sampling) and storage (1.2 kWh to 2.4 kWh). These factors mean that the apparent contribution of wind power to the overall system was low, whereas the solar panels used were more than capable of supplying enough power (40 W rating) given sufficient sunlight. While the stations in Bauguitte et al. (2009) have no wireless connectivity, the UWAAWS stations in Lazzara et al. (2012) utilize a variety of satellite modem providers including Argos and Iridium.

While not strictly Antarctic-related, the GLACSWEB (Martinez et al., 2004), PermaSense (Talzi et al., 2007), and SensorScope (Barrenetxea et al., 2008) wirelessly-enabled ESNs all share at least some similarities in design and purpose with SNOWWEB. GLACSWEB is used to monitor glacier movement and ice conditions with each station communicating with several wireless sensors embedded in the ice below them, as well as with a base station further down the valley in which they are located. Each station communicates directly with a base station, there is no mesh networking required. The PermaSense project monitors permafrost inside rock faces in the Swiss Alps and consists of permanent stations mounted on vertical rock faces with probes buried up to 1 m into the cliff face. It uses multi-hop mesh networking to link all nodes with a GPRS-enabled base station. SensorScope is probably the most similar to SNOWWEB and consists of low-cost wirelessly connected (mesh) weather stations that may be temporarily deployed in relatively harsh environments.

SNOWWEB is distinct from these projects in several ways, perhaps the most obvious being the scale of deployments. SNOWWEB was designed to capture surface-level observations at high spatial resolution, however the term 'high resolution' is subjective and depends on context. In the case of SNOWWEB, this means inter-node distances typically in the order of 3 km to 10 km - much further than most mesh networks. SNOWWEB has also been extensively optimized for rapid and simple deployment with minimally trained personnel in very challenging conditions for a low unit cost. The SNOWWEB project is fortunate in its timing in that during the development phase an off-the-shelf WSN transceiver that met all the project requirements with regard to range, power use, unit price and usability became available. Being able to exploit the XBee Pro S2B transceiver dramatically reduced the complexity of the system design and significantly reduced development time for the wireless networking capabilities.

SNOWWEB STATION DESIGN

Overview

Currently, SNOWWEB stations are designed to be deployed in late spring and retrieved in late summer or early autumn. Power solutions related to winter operation used by others and outlined above (wind turbines and battery banks) are unsuitable for incorporation into the SNOWWEB design for following reasons; wind turbines would at least double the component cost of a station, significantly reducing the number that could be built and deployed to a given area which goes against the fundamental goal of SNOWWEB to provide distributed measurements over a large area. Further, the addition of a wind turbine would likely still not be sufficient without additional, heavy, batteries. Finally, a vertical-axis wind turbine of the same design as the ones used by Bauguitte et al. (2009) was trialled over a winter season with limited success. The station sporadically reported during dark winter months when wind levels were sufficient, however by the time that station was retrieved the bearings in the wind turbine had significantly degraded to the point where it was useless.

The alternative solution, battery banks, presents large logistical problems. Currently, each station along with the required tools for assembly may be comfortably carried by two people to reach positions where vehicle access is not possible. Additionally, two stations easily fit into a sled towed by a snowmobile and up to six may fit into a helicopter. The addition of two 100+ ampere-hour (Ah) lead-acid batteries per station (the estimated capacity required to run a station through the dark winter months) would quintuple the weight per station. This would necessitate the use of vehicles for transportation and would all but rule out the mass deployment of SNOWWEB stations by helicopter as weight is a significant factor when using this mode of transport. Transporting these

batteries to Antarctica would also come at great logistical cost as 40 of these batteries (sufficient for 20 stations) would equate to well over 1 ton of additional equipment to be airlifted from Christchurch, New Zealand.

Physical design

Most SNOWWEB stations employ a 'guyed-mast' design (Fig. 2.1) over areas with significant permanent snow cover (the majority of Antarctica), where a mast is made of modular sections for easy height adjustment to enable differential temperature measurements or increase the height of the antenna to overcome line-of-sight issues. There is also a tripod design (Fig. 2.2) that can be deployed on areas covered by rocks or hard ice. The tripod base is relatively heavy at approximately 20 kg which, when coupled with wide feet that may be buried in snow, covered in rocks, or attached to ice screws, and can eliminate the need to tie the station down with guy wires. Some effort has gone into minimizing the different types, and complexity, of fasteners used to assemble each SNOWWEB station. As a result, only three tools are required for field deployment: a 13 mm socket driver attached ot a battery drill, a 13 mm spanner, and a screwdriver. The sensor booms are t-shaped with folding arms and are pre-assembled with sensors in place to minimize the effort required in the field (two u-bolts clamp it to the mast with additional 13 mm bolts to lock the folding arms in place).

The electronics enclosure is a vertically-mounted section of PVC pipe fitted with a glued cap at the top and a screw cap at the bottom. The SNOWWEB electronics and all external connectors are mounted on this screw cap such that they may be removed from the enclosure by simply unscrewing the cap. The electronics board (Fig. 2.3)is half as long as the enclosure with the remaining length allowing for a 5 dBi whip antenna to be mounted directly to the XBee's RPSMA connector; however the design also includes an externally accessible 'N-type' co-axial connector that is joined to the XBee by a short internal 'pig-tail'. The solar panel connector is wired such that, when connected, it acts as a power switch for the entire station. The major advantage of this is that the enclosure can be sealed prior to transport and simply attached to the mast before screwing in the sensor and solar panel connectors at which point it activates.

Each SNOWWEB station weighs less than 15 kg and, with the effort put into the physical design, takes approximately 20 minutes for a team of three to deploy. Retrieval time is about 15 minutes as factors such as boom alignment do not need to be considered. This makes SNOWWEB ideal for helicopter-based deployments as five to six stations will fit in a medium-sized helicopter such as an AS350 'A-Star' or 'Squirrel' along with a three person team (plus the pilot). Depending on travel time, a standard five-station deployment will take around four hours, meaning twenty stations can be deployed over two full days of field work.

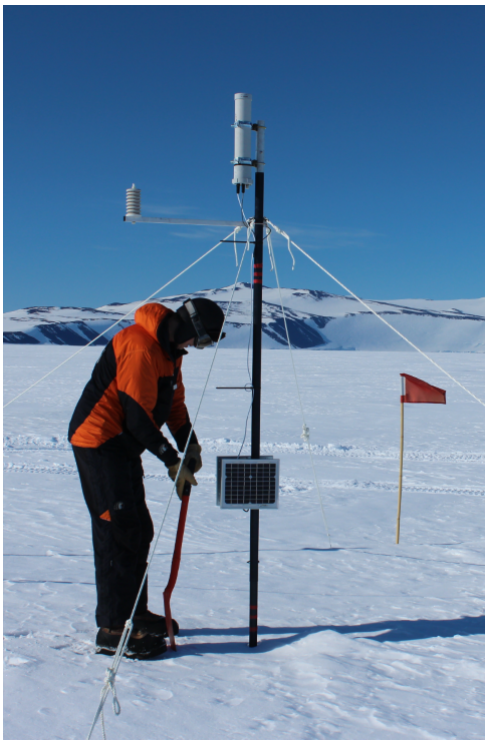

Figure 2.1: A SNOWWEB station in Antarctica (guyed mast design)

Figure 2.2: A SNOWWEB station in Antarctica (tripod design)

Electronic hardware

Each SNOWWEB station is controlled by an ATmega128 micro-controller (Corporation, 2011) running custom firmware written in 'C'. Data packets and error messages are sent via UART to an

XBee Pro S2B module and logged to an on-board microSD card. A Ublox LEA-6T GPS module communicates via the ATmega's second UART port and features an active Geohelix antenna. This is used for both time keeping (ensuring all stations are completely synchronized) and recording raw carrier-phase GPS data for post-processing. Each station is powered by a single 10 W solar panel that charges two lithium-ion cells via an on-board charging circuit. Together these cells supply 7.2 V with approximately 3 Ah of capacity. Current capacity is sufficient for at least 24 hours of operation without any solar input at a 10 s sampling rate with live reporting via the XBee and continuous 1 s logging of raw GPS data. The total current draw from the solar panel is approximately 30 mA at 20 V, or 600 mW, without batteries connected. With batteries connected and charging, typical current draw has been observed at approximately 200 mA or 4 W. Using a 10 W solar panel ensures the station is supplied with sufficient power for a longer duration when the sun angle is not optimal. In fact, when stations are deployed on a 100% ice-covered surface, the solar panel is often exposed to enough diffuse solar radiation to power the station electronics regardless of sun location. The hardware limits of the ATmega128 microcontroller have not yet been reached and it is able to support additional sensors communicating via I^2C, SPI, or wirelessly if the sensor is equipped with another XBee Pro S2B.

Sensors

Environmental information is captured by several sensors attached to each SNOWWEB station, some of which are optional depending on the station's intended function. All stations are equipped with a Bosch Sensortec BMP085 atmospheric pressure (piezo-resistive) sensor (Bosch Sensortec, 2009) located inside the electronics enclosure on the main circuit board (not shown in Figure 2.3). An external SHT75 temperature (band-gap) sensor and relative humidity (capacitive) sensor package (Sensiron, 2011) mounted in a generic plastic 'stacked plate'-style radiation shield attached to an aluminum boom is used to measure air temperature - the relative humidity reported by the sensor was not deemed reliable enough in Antarctic conditions. Wind speed and direction are measured by an NRG Maximum #40H three-cup anemometer (Hall Effect transducer) and an NRG #200P wind vane (potentiometer), both constructed from black Lexan polycarbonate plastic and mounted on an separate aluminium boom to the temperature sensor. The Hall Effect transducer produces digital pulses for each revolution of the anemometer that are timed by one of the Atmega128 onboard timers to determine the frequency which is converted to wind speed following the manufacturer's calibrations. The wind vane potentiometer output is read using a 10-bit analog to digital converter onboard the Atmega128. Rated resolution and accuracy values obtained from manufacturer datasheets for each sensor are provided in Table 2.1. A recent comparison between SNOWWEB observations and those from nearby UWAAWS is presented in Section 2.7.4.2.

Figure 2.3: Main SNOWWEB circuit board.

Table 2.1: SNOWWEB Sensors

Property	Sensor	Resolution	Abs. (Rel.) Accuracy
Wind Speed	NRG #40H Cup	-	0.5 ms^{-1}
Wind Direction	NRG #200P Vane	1°	5 (1) °
Temperature	SHT75	0.01 K	1.0 (0.1) K
Rel. Humidity	SHT75	0.05 pp	2 (0.1) pp
Pressure	BMP085	0.01 hPa	1.5 (0.5) hPa

Network hardware

During the initial development phase of the earliest SNOWWEB hardware iteration - undertaken before the current research project - the XBee Series 1 transceiver developed by Digi International was trialled with custom mesh networking code. Difficulties with this approach and further changes to other hardware components lead to the Series 1 transceivers being scrapped in favor of the XBee Pro S2B (Inc, 2010) - common to medical monitoring and home automation applications - with the built-in Digi International implementation of the ZigBee protocol including some proprietary enhancements. The XBee Pro S2B module operates at a frequency of 2.4 GHz with a rated transmit power of 63 mW (+18 dBm) and a power draw of 390 mW when transmitting, 160 mW when the receiver is active (normal router idle). This unit was chosen as its on-board micro-controller and implementation of the ZigBee stack simplifies firmware requirements and reduces the processing load on the micro-processor, where all network-related tasks can be offloaded to the XBee unit. The primary disadvantage of this approach is users are required to essentially treat the XBee as a 'black box', with limited tools available for debugging and diagnostics when problems arise, however this was considered acceptable given the benefits of simplicity afforded.

A large variety of antennae have been utilized in the field, including a 5 dBi omni-directional whip antenna (32° vertical beam width) mounted directly to the XBee inside the enclosure, a 10 (15) dBi omni-directional antenna with 12° (9°) vertical beam width mounted on top of the weather station mast. All of these antennae are 'monopole' antennae. The coordinator XBee at the base station is typically connected to one of the 15 dBi omni-directional antennae. A drawback of using the 15 dBi antennae is the extremely tight vertical beam width which means antenna mounts must be absolutely vertical. However combining these antennae with lower-gain antennae featuring higher vertical beam widths is often a good compromise between range (reliable communication between 15 dBi and 5 dBi antennae has been observed over distances greater than 10 km) and the need to align the station masts exactly and have them remain aligned for the duration of the deployment.

NETWORK DESIGN

Overview

The ZigBee standard has been created by an industry consortium - the ZigBee alliance - and the first version was published in 2006 (Organization, 2006). It covers the networking and application layers of the OSI reference model, the underlying wireless transmission technology is provided by the IEEE 802.15.4 physical layer and medium access control standard (IEEE, 2011). At the

network layer, ZigBee can support the star, tree, and mesh network topologies by utilizing three different types of 'nodes'. The first, a ZigBee 'coordinator', is responsible for starting a network and determining its major configuration parameters (the operating frequency for example). The second, a ZigBee 'router', is capable of connecting to other ZigBee routers (and the coordinator) and passing data to/from all other node types to aid in forming tree or mesh networks. Finally, a ZigBee 'device' associates itself with a close-by ZigBee router or coordinator and communicates solely with that node. In a tree network all ZigBee routers form a routing tree that is rooted in the coordinator, and simple tree-routing is used. In a mesh network, more general routing based on the ad-hoc on-demand distance vector (AODV) protocol (Perkins and Royer, 1999) is used, but the standard provides some optimizations to allow for efficient data collection in cases where most data flows from sensors (routers and/or devices) to the sink (coordinator). In a typical network, device nodes contain sensors and router nodes are solely tasked with routing messages to and from the coordinator. The coordinator stores or pre-processes the data and makes it available for further processing. In terms of transmission reliability, ZigBee uses two different mechanisms: the IEEE 802.15.4 MAC layer can be instructed to perform a number of retransmissions on a hop-by-hop basis. Additionally, the ZigBee application support layer can carry out end-to-end retransmissions, automatically handling acknowledgments and retries up to a certain point.

In the case of SNOWWEB stations, the large majority of traffic flow is from each station to the coordinator with occasional control messages sent from the coordinator to either individual stations or as general broadcasts. A major deviation from the 'typical' design is that SNOWWEB does not feature any 'device' nodes. Instead, all stations are designated as 'routers' in order to make deployment easier and to increase the robustness of the network ('routers' will act as intermediaries and pass messages between each other whereas 'devices' will not). The XBee Pro S2B implementation uses mesh routing and implements optimizations for data collection scenarios where most traffic is from sensors to the sink.

Role of the coordinator

For SNOWWEB, the ZigBee coordinator is connected to a standard desktop PC. In addition to the roles defined by the ZigBee standard, the coordinator serves as a data collector and command-and-control machine for the SNOWWEB stations, providing a link between the stations and the outside world via the Internet if a connection is available. If the coordinator is connected to the Internet it will upload incoming data either in real time or periodically along with summaries of network statistics. It is also possible to control the network remotely via messages left on another server that is periodically polled. For example, individual stations can be instructed to sleep in order to save power, or their sampling rate could be modified (both are examples of adaptive

sampling). In order to better facilitate the flow of information from the stations to the coordinator, the coordinator periodically sends a 'many-to-one' route request broadcast to the other XBees in order to force them to update their routing tables to take changing network conditions into account. This helps to maintain network connectivity.

Role of a SNOWWEB station

All stations in the SNOWWEB network are generally configured as routers as opposed to end nodes. This eliminates the need to build, power and deploy/retrieve extra routing stations while keeping all stations functionally identical. Deployments are typically planned with the safety of the deployment team and the capture of interesting meteorological observations as the first priorities. This often results in long chains of nodes in straight lines as keeping to existing tracks is safer, faster, and often still fits in with the science objectives. Obviously this type of deployment pattern is not ideally suited to mesh networking, however the stations are arranged such that their areas of coverage overlap sufficiently to allow the failure of every second node (but not two nodes in a row).

Overseer algorithm

In previous field seasons, extended communication outages have been observed . One of the causes was identified as stations leaving the network and not returning again, often coinciding with an outage at the coordinator. Unfortunately, coordinator uptime may not always be guaranteed over an extended time-frame in Antarctica as the power supply at research stations may sometimes fail. As such, it is important that SNOWWEB stations are able to fully recover from coordinator failures. A partial solution is integrated into the XBee in the form of a network watchdog timer which forces an XBee to re-join a network if it does not receive any communication from a coordinator within a given period of time. This solution is too simplistic for ideal SNOWWEB operation as station report times, and therefore coordinator replies, are configurable and subject to change. In addition, the retransmission mechanism in the XBees, consisting of both the four MAC-layer retransmissions per hop and three end-to-end re-transmissions, is not sufficient to cover a network outage longer than four to five seconds. To mitigate against both issues an application layer algorithm has been implemented which is capable of resetting XBee modules (both a hard reset and a network parameter reset) and buffering messages so they survive longer network outages (exact time is dependent on sampling rate). This is referred to as the 'Overseer' algorithm and is depicted in Figure 2.4. It runs on the micro-controller in each SNOWWEB station.

This algorithm was coded in 'C' and integrated with existing station code on-board the SNOW-WEB micro-controller. It includes a rolling buffer in memory sufficient for six data packets (as dictated by available RAM). Each packet is passed to the buffer and then tagged for transmission. The XBee application program interface (API) packet specification (which is essentially the application support (APS) interface (Inc, 2010)) includes a 'unique identifier' byte in the header which allows easy tracking of a given packet and determine if it was successfully transmitted. Once a success/fail message is received from the APS, the corresponding packet is either tagged for re-transmission or its buffer space is used for a new packet. Re-transmission attempts are made once every second. If there have been more than two failed re-transmissions in a row then a 'network reset' command is sent to the XBee and the program waits for a response indicating the XBee successfully re-joined the network (10 s time-out). Regardless, the failed re-transmission counter is reset. If this entire process fails then it is assumed there has been a critical network failure and the XBee is turned off to save power. Every hour the main routine resets any failure flags and re-initializes any components that have reported problems. This will include the XBee unit if it has reported a critical network failure, ensuring that the station will keep trying to re-join the network automatically. If all six buffer places are occupied by packets in need of re-transmission, and a new packet arrives from the application, the oldest is pushed out of the buffer.

Pre-deployment testing

Extensive field testing was carried out at both the Birdlings Flat (43.821°S, 172.687°E) and Cass (43.046°S, 171.768°E) research stations run by the University of Canterbury. The topography of both sites is ideal for testing wireless network configurations as they are surrounded by an expanse of flat land that is relatively secure and away from major population centers. A mix of minor and major topographical features, along with vegetation and combined with the use of low-gain antennae, allowed the opportunity to test the reliability and robustness of various deployment patterns. The shortcomings of the 2.4 GHz frequency in this application were evident (and exploited) during this process as the simple act of moving a station behind a low bush could force it off the network unless another station was either within sight or very close by.

Anomalous network behavior observed during the 2013/14 deployment in Section 2.6 could not be recreated at either test site before the 2014/15 deployment described in Section 2.7. This is despite stations facing more challenging atmospheric conditions (high humidity and rain) and far longer deployment times.

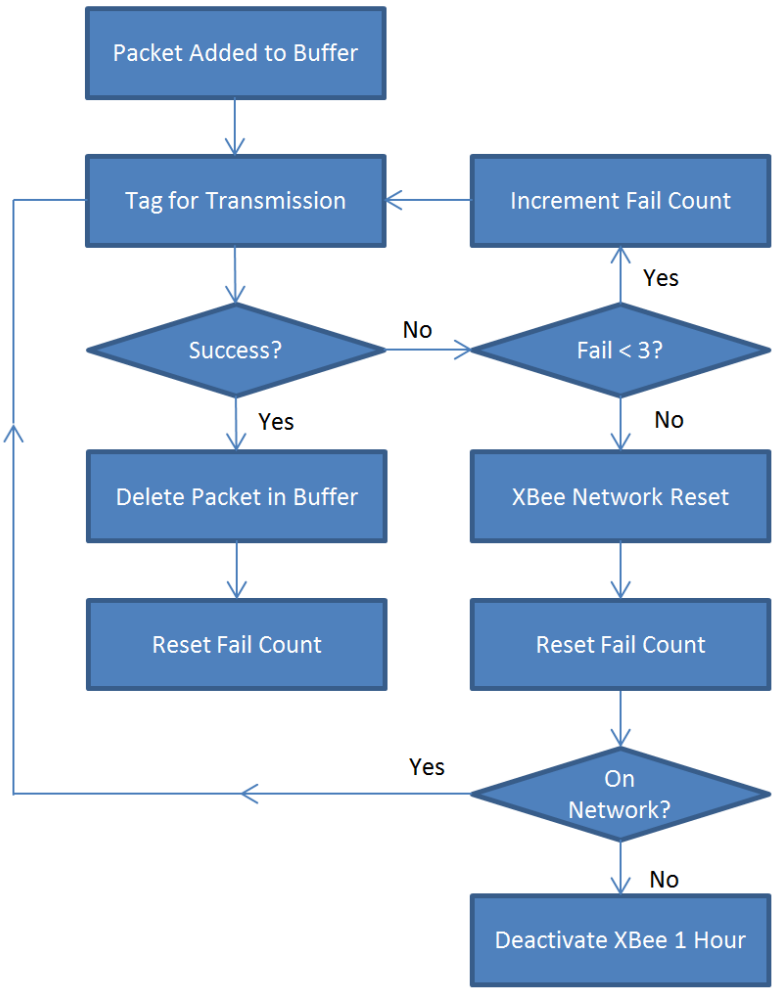

Figure 2.4: Flow diagram of Overseer algorithm logic.

SNOWWEB 2012/13 - TEST DEPLOYMENT

The first SNOWWEB deployment for this research was primarily for *in situ* testing of equipment and software. Twelve stations were deployed and left in the field for almost two weeks to test functionality under typical Antarctic summer conditions (sub-zero temperatures and 24-hour sunlight) as well as wireless network performance in the field. Of these, nine were part of the main network testing group and three were deployed in an opposite direction for measuring ice movement using their on-board GPS. No communication was expected from these three as a combination of distance and antenna choice meant that successful transmissions were unlikely, however all were set up to transmit regardless to investigate how the firmware would respond to extended network outages. One of these stations, fitted with a 15 dBi omni-directional antenna, did successfully transmit a significant amount of information back to the coordinator over a link distance greater than 10 km.

At the end of the deployment, just before the stations were retrieved, several 'stress tests' were carried out to determine how SNOWWEB would respond under abnormal network conditions (high sampling and report rates, station outages, *etc*). Most stations functioned as expected, with three of the nine stations in the primary test group experiencing non-fatal complications due to hardware failures and human error, none of which were directly attributable to the Antarctic environment. The other three stations from the 'ice movement' group functioned as expected, or better in the case of the station that successfully communicated with the coordinator. In light of the 2013/14 deployment (next section), further details on this deployment are no longer relevant but may be found in the paper by Jolly et al. (2013).

SNOWWEB 2013/14 - FIRST LARGE-SCALE DEPLOYMENT

Overview

The first large-scale SNOWWEB deployment, the observations from which form the focus of Chapter 3, occurred in the area around White Island to study the effect of the surrounding complex topography on localized flows - refer to Figure 2.5 for a map. This area is particularly useful to study because it encompasses the main airfields (Pegasus and Willie Field) used by the United States Antarctic Program (USAP) and Antarctica New Zealand, as well as the research stations 'McMurdo Station' and 'Scott Base'. There is a significant amount of human activity in this region so understanding the local dynamical processes and evaluating the forecast skill of current models in the area is potentially very valuable.

Seventeen SNOWWEB stations were available for this deployment. Of these, nine were equipped with a full set of sensors measuring wind speed, direction, temperature, relative humidity, and atmospheric pressure. The remaining eight did not have wind sensors, but still measured temperature, relative humidity, and pressure.

Station placement

The exact positioning of SNOWWEB stations was influenced by the following criteria: meteorological value of the entire network, inter-station distance, total area covered, sensor configuration of available stations, and proximity to known access routes. Optimizing inter-station distance and total area covered is a minimization/maximization problem. In order to maintain a high spatial resolution and enable robust wireless communications, inter-station distance needs to be small. Yet in order to maximize network coverage, inter-station distance should be large. There is a limit

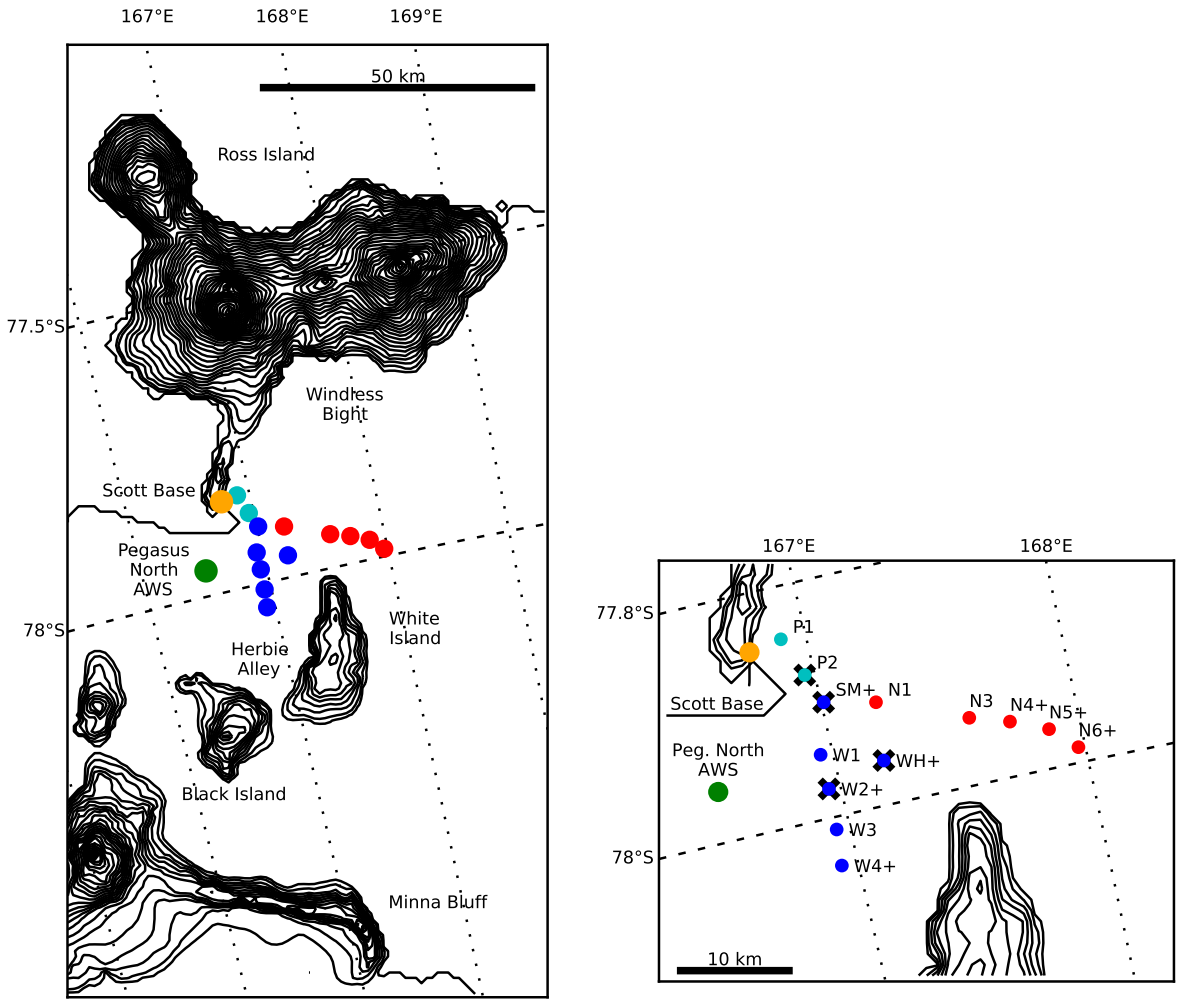

(a) Greater Ross Island region

(b) Black (left) and White (right) Islands

Figure 2.5:

Map of greater Ross Island region (a) and SNOWWEB deployment (b).

(a) shows Ross Island (top) with Hut Point Peninsula extending southward, White Island (middle), Black Island (mid-left), Mount Discovery (bottom-left) and Minna Bluff (bottom). Pegasus North AWS (belonging to the UWAAWS network) is annotated, all other markers indicate the position of SNOWWEB stations.

(b) is an enlargement of the deployment in (a) with stations labeled. Stations beginning with 'W' or 'S' form the 'west' string and stations beginning with 'N' form the 'north' string (blue and red markers respectively). Cyan markers denote a small string of stations known as 'Pegasus'. Black crosses indicate the station malfunctioned after ~11 days, while the '+' symbol in station names indicates the presence of wind sensors. 'Pegasus North' UWAAWS is represented by the labeled green marker. Station N2(+) failed immediately and is not shown for clarity. Orange indicates Scott Base where the SNOWWEB network 'coordinator' was located.

which aids the selection of distance that is the 'area of influence' of a single station. Placing stations too closely together will result in redundant measurements (as the meteorological conditions each station observes will be very similar), however placing them too far apart will not capture

the spatial variability sufficiently. There is a lack of high resolution observational data in the area so Antarctic Mesoscale Prediction System (AMPS) model, and satellite thermal, data were used as part of the decision-making process. Ultimately the limiting factor was the range of wireless communications, where the maximum stable link distance was determined to be 10 km. To ensure redundancy in wireless transmission inter-station distance was set to 5 km to allow for individual station failures.

A more detailed overview of the meteorology of the target area, and why this is interesting, is discussed alongside the results from this deployment in Chapter 3. Sensor configuration (whether or not wind speed and direction sensors were available) was a limiting factor and choosing where to deploy wind sensors involved a level of expert opinion and assessment of model data. Stations with wind sensors were positioned in areas where large wind vector gradients were expected. With regard to individual station placement, the meteorological value of each location was also considered - where the probable wind and temperature gradients between each station would ideally be maximized for the given distance. This was partially constrained by logistical and safety requirements that required the deployment team stay close to established trails where possible and avoid certain areas such as airfields and heavily crevassed regions. Fortunately, existing routes in the area were positioned such that placing stations along them with 5 km spacing would produce interesting, rather than redundant, meteorological data. Three existing routes were utilized which split the network into three named parts: 'Pegasus' Road with the 'PEG' prefix, the route to Black Island with the 'WEST' prefix, and the South Pole Traverse route with the 'NORTH' prefix. The one exception to staying on established trails was a 10 km off-trail traverse beginning from the 'six mile' marker (the site of SM station) and stretching toward the tip of White Island. A single station (WH) was placed at the end to observe wind flow around the northern edge of the island.

Final station placement is shown in Figure 2.5b, which is itself an enlargement of Figure 2.5a. One location, W2, is the site of a 'double station' with two SNOWWEB stations (W2 and W2b) deployed on the same mast. W2 is position 2 m above the ground with all available sensors and W2b is positioned 4 m above the ground with temperature and pressure sensors only, in order to gather observations of the vertical temperature profile. Two stations are shown (Fig. 2.5b) as full red circles and not labeled as they either experienced catastrophic failure or were poorly placed (see Section 2.6.3). One station - CRATERHILL - is not shown or labeled for clarity is it is located on a hill very close to Scott Base but approximately 250 m above it. This position was identified as ideal for potentially capturing flow over Hut Point Peninsula as well as providing an excellent vantage point for routing network traffic from the ice shelf.

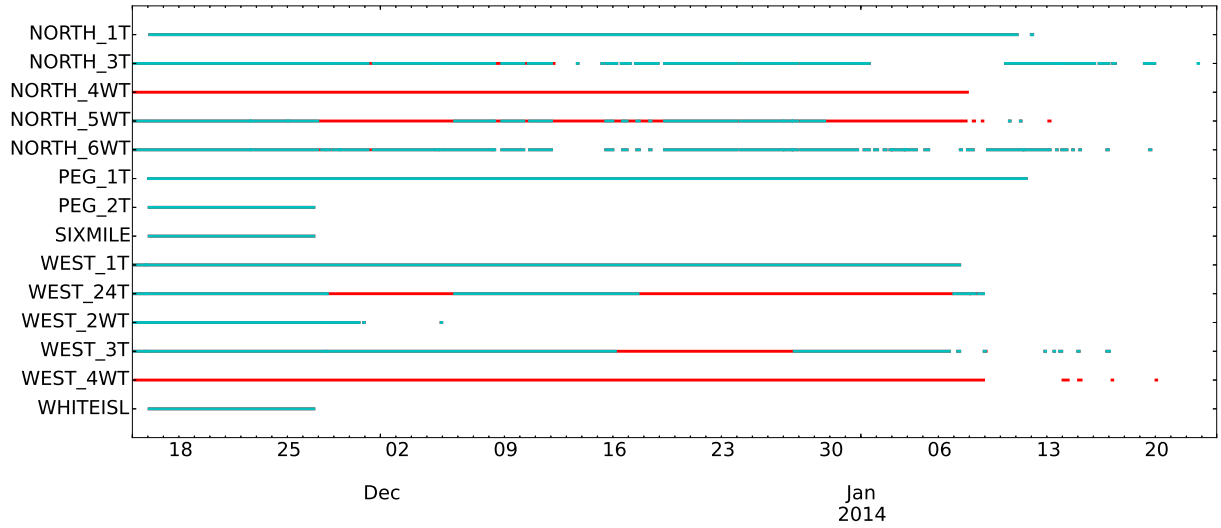

Figure 2.6: Total station uptime (red) with wireless transmissions overlaid (cyan) for 2013/14 season.

Table 2.2: Station uptime and wireless transmission success rates, where uptime is the percentage of observations recorded by the on-board SD card relative to the maximum possible for the time period (entire deployment period from 2013-11-15 0000 UTC to 2014-01-24 0000 UTC). Wireless transmission rates are the percentage of packets recorded by the coordinator that were also present on the on-board SD card. Values greater than 100% are possible in the event of an SD card failure but were not observed this season.

Station	Uptime	Trans.	Station	Uptime	Trans.	Station	Uptime	Trans.
N1	79.7%	98.2%	P2	80.8%	99.1%	W1	76.1%	94.6%
N3	64.4%	80.3%	P1	15.2%	98.3%	W2b	77.8%	29.2%
N4	76.6%	0.0%	SM	15.1%	98.4%	W2	20.8%	85.6%
N5	76.5%	46.4%	WH	15.1%	83.3%	W3	75.6%	69.3%
N6	61.1%	86.9%				W4	78.3%	0.0%

Deployment report

General overview

The SNOWWEB deployment lasted from approximately the 15th of November 2013 to the 24th of January 2014 - deployment and retrieval took multiple days so exact dates vary between stations. Fourteen stations produced usable data, two produced unusable data, and one suffered an un-

Table 2.3: Distances between deployed SNOWWEB nodes in kilometers. Underlined values coincide with dominant routing links. Refer to Figure 2.5b for station locations, wireless links are not displayed on that figure for clarity. Station names have been shortened to reduce table size, where 'C' represent the 'coordinator' at Scott Base, 'CH' represents the `CRATERHILL` relay station positioned on a hill close to, and overlooking, Scott Base (not shown in deployment map), and 'SM' and 'WI' represent the SM and WH SNOWWEB stations respectively.

	SNOWWEB Node Number														
	C	CH	P1	P2	SM	WI	W1	W2	W3	W4	N1	N3	N4	N5	N6
C	-														
CH	1.2	-													
P1	3.2	3.9	-												
P2	5.6	6.8	4.0	-											
SM	8.3	9.6	7.1	3.1	-										
WI	16.1	17.3	14.8	10.9	7.8	-									
W1	11.6	12.8	11.4	7.6	4.9	5.9	-								
W2	14.7	15.9	14.7	10.9	8.1	5.8	3.3	-							
W3	18.4	19.5	18.5	14.7	11.9	7.8	7.1	3.8	-						
W4	21.7	22.8	21.9	18.1	15.3	10.6	10.5	7.2	3.4	-					
N1	12.7	13.9	10.6	7.1	4.9	5.5	7.1	9.2	12.4	15.6	-				
N3	21.4	22.5	19.0	15.9	13.7	8.9	14.3	14.7	16.2	18.2	8.8	-			
N4	25.1	26.3	22.7	19.6	17.5	12.2	17.9	18.0	19.0	20.6	12.6	3.8	-		
N5	28.8	30.0	26.4	23.3	21.2	15.7	21.4	21.3	21.9	23.1	16.3	7.5	3.7	-	
N6	31.9	33.1	29.5	26.4	24.1	18.2	24.1	23.6	23.8	24.7	19.3	10.5	6.8	3.2	-

known technical fault where it stopped recording and transmitting very shortly after deployment. The two stations that produced unusable data were named `CRATERHILL` and `TEMP_R_RWV`, with the former rendered unusable except as a network repeater after it was repeatedly blown over. While this station was often re-righted by staff and scientists from Scott Base, the original northward

orientation was not preserved and instrumentation was destroyed. TEMP_R_RWV was positioned in a poor observational area as part of initial testing and could not be re-positioned within the available time so its data is ignored. Despite damage to its sensors, CRATERHILL was still useful as a network routing location and so is included in routing data, but TEMP_R_RWV is not mentioned further.

For unknown reasons, three stations only recorded data for the first 255 hours (10.6 days). One failed after 351 hours (14.6 days), while the nine remaining stations continued for over 55 days. Of these, two had occasional gaps in the data recorded while seven had mostly contiguous data records. Most stations had completely ceased recording around the 7th to the 10th of January. Some of the outages that occurred in January were caused by stations falling over as their anchoring systems melted out of the ice due to very warm conditions. The overall up-time and reliability figures are presented in Figure 2.6 and Table 2.2. The sub-optimal uptime of all stations was investigated but no cause was found. All SNOWWEB stations were using the exact same firmware binary and while there were two, subtly different, versions of hardware present there appears to be no correlation between hardware version and station failure. Time constraints, combined with the relatively long period required for faults to occur, as well as the somewhat limited logging capability of the micro-controllers have all hampered further investigation. However, particular suspicion has fallen on the third-party code library used to write to the 'FAT' file systems on the SD cards. In an effort to eliminate the problems faced by this deployment, hardware and firmware changes were made to SNOWWEB before the 2014/15 deployment. These changes were made by another party for a related project and a summary is presented in Section 2.7.4.2.

Sensor Performance

The sensors performed well with favorable comparisons between SNOWWEB stations and nearby UWAAWS which are presented in greater detail in Chapter 3 (Section 3.2.2). Due to the shorter timescales involved in this deployment, a more detailed assessment is presented from the subsequent deployment in Section 2.7.4.2 below.

Network performance

Distances between all stations are presented in Table 2.3, with common wireless links underlined (refer to Figure 2.5 for spatial distribution patterns - links are not shown in this figure for readability). The links displayed in the table are obtained by the PC attached to the coordinator XBee and reflect the routing table of the coordinator XBee. This routing table is constructed from the replies received after the coordinator XBee broadcasts a 'many-to-one' route request packet to the entire network and should reflect the current state of the network at that time. Links displayed

account for at least 10% of all traffic through that station's XBee unit, with a minimum cut-off of 15000 route records (where route record packets are received approximately every 10 s), and thus could be deemed robust. Some of the links reported in this table are over suspiciously large distances, with the largest between N6 and CRATERHILL measuring 33.1 km. Anecdotal reports of range tests by others achieving similar distances mention the use of directional antennae but these results have not been published. Factors that may help to explain this reported route are: the rated gain of 15 dBi for each antenna, the high transmit power and receiver sensitivity of the XBees, the fact that CRATERHILL is situated on a hill at least 250 m above the level of N6, the extremely low humidity of Antarctic air, and the complete lack of any vegetation with all surfaces between the two nodes comprised of extremely deep hard-packed snow (predominantly) or bare volcanic rock. Regardless, further tests with a sole focus on the range capability of the XBee Pro S2B units are required as these were not possible within the time and logistical constraints present during the deployment.

Regardless of the validity of the reported routes, a large amount of data was successfully transmitted from most SNOWWEB stations, as indicated in Table 2.2 and by Figure 2.6. Values are shown as a percentage of observations recorded to the SD card, where the SD card is assumed to be the reliable source. If the SD card failed it was possible for the XBee to continue reporting data (this behavior was observed during the 2012/13 test deployment), which would result in a success rate higher than 100%. Overall, transmission success rates were high when stations were close to the coordinator, reducing with range and when lower gain antennae were used. In particular, P2 and N1 had excellent success rates which were sustained over a long period of time. Nine stations had a success rate of 80% or higher, with three more featuring varying success rates between approximately 30% and 70%. Two stations, N4 and W4, did not successfully transmit any data to the coordinator. Both of these stations featured 5 dBi antennae and were over 20 km from the coordinator so direct communication was impossible. By design, the mesh network formed by the XBee units should have accommodated these stations by relaying messages through nearby stations which had better antennae and more reliable data links, however this appears not to have happened. A point of commonality between the majority of links shown in Table 2.3 (links are underlined) is that one of the end points is located on solid ground - either the coordinator(C) or Crater Hill relay station (CH). All other stations were located on an ice sheet, which is a thick slab of compacted snow and ice tens to hundreds of meters thick. Snow is a poor electrical conductor, and it is possible that the ground planes for the monopole antennae were insufficient. This may have distorted the beam pattern such that station-to-station communications were less reliable, therefore these links would be less likely. The presence of multi-hop routes to other stations shows that the XBee units were correctly configured (all XBees had identical configurations except for a unique 'name' given to them), and successful tests back in New Zealand did not raise any concerns around possible scaling issues. Because it was not seen as a significant problem during

this deployment, the possible issue with inter-station communication on the ice shelf was not addressed until after the following season's deployment when it experienced an almost total failure of network communications (see Section 2.7.4.3).

Hardware performance

Despite some challenging wind conditions, all stations stayed standing until the middle of January. At this point, under considerably warmer temperatures than expected, all of the `WEST` stations, bar W1, fell over after their anchors melted out of the snow. Two more stations, P2 and P1, were also affected by melting snow and likely would have fallen had they been retrieved later in the season. All other stations on the ice shelf had no mechanical problems and their rigging was still secure before they were removed. As mentioned earlier, `CRATERHILL` was blown over (onto rocks) multiple times during the deployment. Remarkably, the wind sensors withstood the first incidents, however were eventually broken as was the external 15 dBi fiberglass antenna. `CRATERHILL` was deployed on top of 'Crater Hill' and was therefore exposed to extremely high winds. Utilizing the tripod design, its legs were secured using stakes driven into rocky permafrost which, while initially sufficient, later melted free as the summer progressed. If SNOWWEB stations are again deployed onto rocky terrain with significant permafrost then additional measures must be taken to secure them.

SNOWWEB 2014/15 - MAIN DEPLOYMENT

Overview

Following the success of the 2013/14 deployment, further funding was secured for another SNOWWEB deployment during the summer season of 2014/15. The main aim of this deployment was to investigate how Ross Ice Shelf airstream (RAS) events and southerly storms in general affect sea ice production in the Ross Sea, namely via the Ross Sea polynya. Investigating sea ice is beyond the scope of the research discussed here, however this deployment was still a valuable source of data for Chapter 4 that validates AMPS output for the duration of the summer deployment. The area of deployment for this season was much larger than in 2013/14 and was situated on the Ross Ice Shelf to the east of the McMurdo Ice Shelf, the site of previous SNOWWEB deployments. The stations were well situated to investigate wind coming from and around Minna Bluff and how this interacted with Ross Island.

Hardware and firmware changes

The 2014/15 deployment featured a new version of hardware and firmware along with a different network architecture. Instead of forming one large network reporting to a coordinator, twenty stations were split into four networks of four to six stations which were placed in separate areas, where one node of each network was designated as a 'sink' and would record the data of all the others along with its own. The other stations would both record their data locally and send it to the sink, relaying any data packets received from neighbors. This topology was not compatible with the existing network design so a simpler XBee Pro Series 1 module was used instead without built-in mesh networking capability.

Station placement

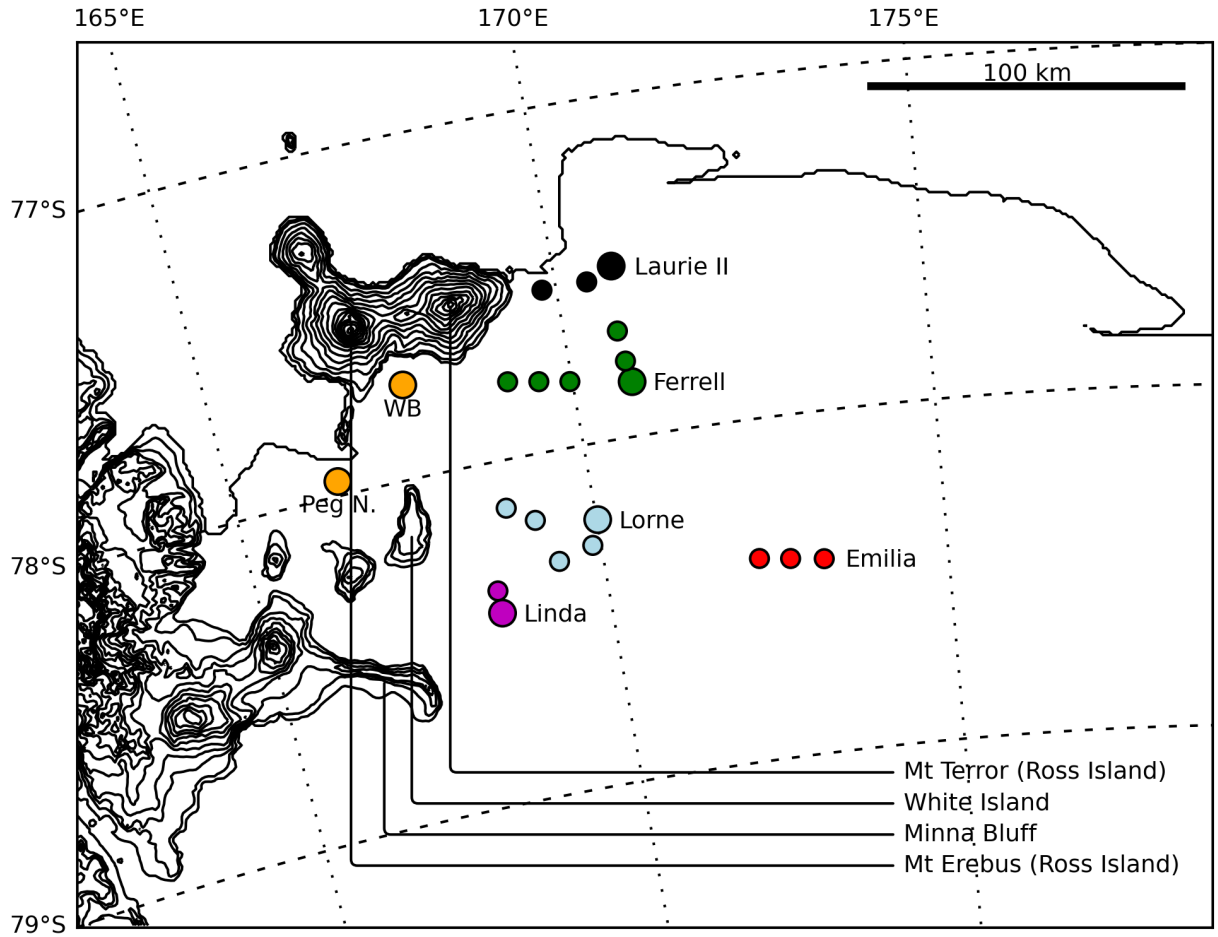

Figure 2.7: Map of 2014/15 SNOWWEB deployment on the Ross Ice Shelf. Blue markers are SNOWWEB stations, magenta represents existing UWAAWS stations - important units are named.

Table 2.4: Station uptime, where uptime is the percentage of observations recorded by the on-board SD card relative to the maximum possible for the time period. Wireless transmission rates are not shown as successful wireless transmissions were negligible.

Station	Uptime	Station	Uptime	Station	Uptime	Station	Uptime
Emilia_1	99.7%	Ferrell_1	99.2%	Laurie_1	99.9%	Linda_1	99.9%
Emilia_2	99.9%	Ferrell_2	99.8%	Laurie_2	99.9%	Linda_2	0.0%
Emilia_3	99.7%	Ferrell_3	99.9%	Laurie_3	99.9%	Linda_3	99.9%
Emilia_4	99.9%	Ferrell_4	0.0%	Laurie_4	99.9%	Linda_4	99.9%
Emilia_5	99.6%	FuelDump	99.9%	Laurie_5	99.9%	Linda_5	99.8%

Inter-station separation was set at approximately 10 km on this occasion, as results from the 2013/14 season showed reliable links were possible over distances greater than 20 km. This also allowed coverage of a far greater area with the same number of stations. This time 20 stations were available, 19 of which had functional wind sensors in addition to the standard temperature, relative humidity, and pressure sensors. Four strings of five stations were initially planned, with each string stretching east-west in order to best capture the south-north flow and its edges. Two strings were to be placed level with Ross Island and two level with the southern edge of White Island, however operational constraints meant this was not achievable. These strings were joined to four existing AWS units, augmenting their observations. Exact station placement is shown in Figure 2.7

Deployment report

Overview

With regard to the science objectives, this was the most successful SNOWWEB deployment to date. While the original deployment pattern was not possible, the final configuration still provided good coverage of the target area. Twenty stations were deployed between the 22nd of November 2014 and the 6th of December in 2014, with weather causing significant delays. Twelve stations were then retrieved between the 11th and 13th of February, with eight stations left out for the winter for testing after a brief visit to each to collect data and ensure the stations were still operational. This season, 2 stations did not record data due to SD card problems, while 2 more had faulty wind direction sensors (damage may have occurred during transport). This left 16 fully functional

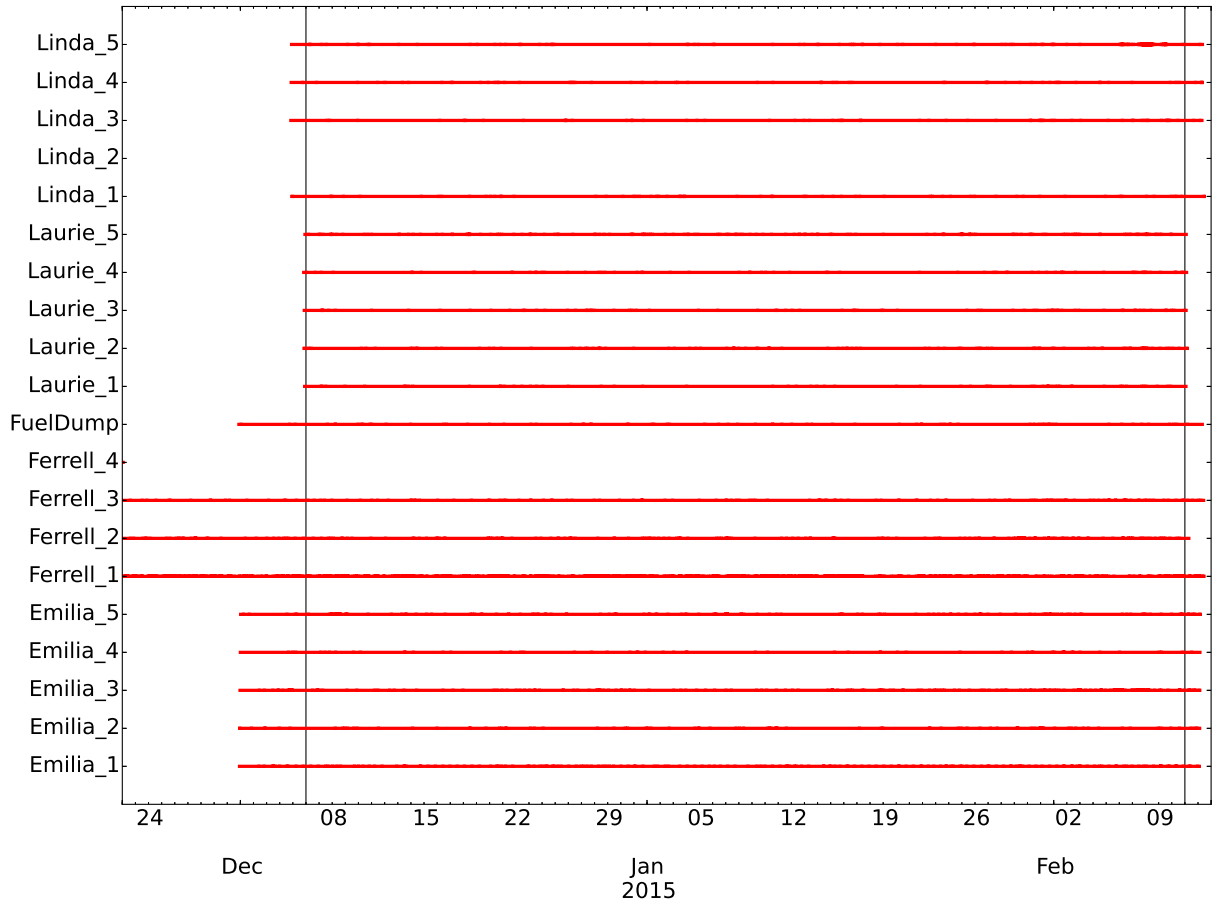

Figure 2.8: Total station uptime. Wireless transmission rate not overlaid (as in Fig 2.6) as very few transmissions were actually successful. Black lines indicate the period when all stations were fully deployed, from the 6th of December 2014 to the 11th of February 2015

stations, 15 of which were equipped with wind sensors (the final station was temperature and pressure only). These rates of failure are more than acceptable, given the nature of working in Antarctica.

Figure 2.8 shows the uptime for each station, where `Linda_2` and `Ferrell_4` were the two stations with failed SD card holders. For the almost two and a half months of operation, station records on the 18 functional stations were universally almost contiguous, with only sporadic and individual missed records, which is an excellent result - this is not visible in Figure 2.8 as the periods are too small. Values are available in Table 2.4 and show that the worst result, of the 18 functional stations, was `Ferrell_1` with a 99.2% complete record of observations.

Sensor Performance

Observations captured by SNOWWEB stations were compared with those captured by nearby UWAAWS, with mean values for correlation and bias presented in Table 2.5 along with the stand-

Table 2.5: SNOWWEB wind speed, temperature, and pressure comparison with nearby UWAAWS observations.

Property	Sensor	Mean Correlation	Mean Bias	Std. Bias
Wind Speed	NRG #40H Cup	0.9268	-0.18 ms^{-1}	0.53 ms^{-1}
Temperature	SHT75	0.9470	0.70 K	0.76 K
Pressure	BMP085	0.9990	-4.20 hPa	1.65 hPa

ard deviation of the bias to give an indication of variability. Wind speed correlations were very good ($r = 0.9268$) given the spatial distances between stations (10 to 40 km) and the expected spatial variation of the wind field. Bias was also within the uncertainty range of the instrument, however this was substantially variable in both the positive and negative direction. Temperature correlations were also good ($r = 0.9470$), however there was a high bias (0.7 K) that again varied. A likely contributor to this is the design of radiation shield employed and consequently temperature observations are treated with caution in subsequent chapters. Pressure correlations were excellent ($r = 0.9990$), however a substantial bias was observed in the order of -2 to -6 hPa. In lab experiments this was discovered to be a simple offset that could be calibrated, however a logistical mistake made it impossible to do this for most stations. The subsequent analysis of pressure data in Chapter 4 therefore uses pressure values relative to a given point (station) to enable a valid comparison to other datasets.

Taylor diagrams (Taylor, 2001) are used to give a further indication of observation validity. Extremely useful tools for investigating correlation for many points within the context of another variable in a single plot, Taylor diagrams are polar plots with correlation coefficient as the angular coordinate (log scale) and standard deviation as the radial coordinate. Figure 2.9 shows Taylor diagrams for wind speed (a), 2 m temperature (b), and pressure (c) comparisons between (blue), and within (red / green), the SNOWWEB and UWAAWS networks. The wind speed comparison shows a spread in standard deviations but largely consistent correlation values. Both variables show consistency between the SNOWWEB/UWAAWS comparison (blue) and the SNOWWEB internal comparison (green), with the internal UWAAWS comparison (red) slightly worse. This is very likely due to the distance between the stations as the wind field is expected to vary over the study area. Better results are seen for temperature, particularly in the spread of standard deviations as those plotted tend to more closely match the reference line (dashed - the mean of UWAAWS station standard deviations). The results are even better again for pressure despite the issues with bias mentioned earlier, again indicating that the bias is likely a simple offset.

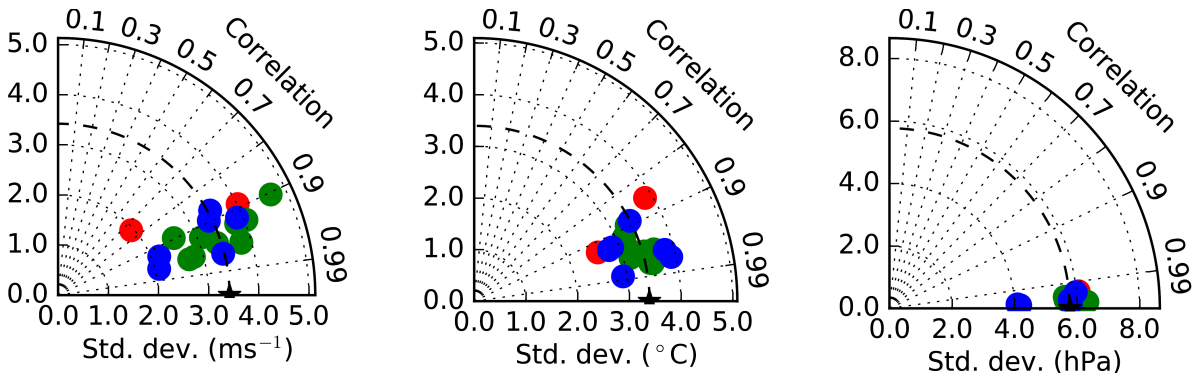

(a) Wind speed (b) 2 m Temperature (c) Pressure

Figure 2.9: Taylor diagrams plotting correlations within and between the SNOWWEB and UWAAWS networks against station standard deviations for wind speed (a), 2 m temperature (b), and pressure (c). Diagrams are polar plots, with correlation on the angular axis and standard deviation on the radial axis. Blue markers depict SNOWWEB vs UWAAWS comparisons, green SNOWWEB vs SNOWWEB comparisons, and red UWAAWS vs UWAAWS. The dashed line is a reference standard deviation (mean of standard deviations within the UWAAWS network).

Network Performance

The single major detractor from the 2014/15 deployment was the failure of the wireless communications system. Most stations did not successfully transmit or receive any data packets, and those that did were only sporadically successful with a few packets. When conducting tests on the ice shelf, prior to the final deployment, it was found that stations which worked over a 16 km separation in New Zealand would not communicate over 2 km on the ice shelf. Atmospheric conditions and line-of-sight were ideal in Antarctica, and the test area used has been the site of several successful SNOWWEB tests and deployments in previous seasons. The communications issues were partially resolved when one of the stations was located on land, which kick-started the discussion around ground planes that has been covered in Section 2.6.3.3. A detailed discussion of future SNOWWEB generations is beyond the scope of this document, however it is likely that the antenna type used will be changed to a dipole design which does not require a ground plane.

Hardware performance

As with the previous deployment, this deployment faced some challenging wind conditions with speeds exceeding 90 kmh^{-1} at times. Regardless, all stations were in perfect condition when visited again at the end of the season. There were no issues with snow melt this season because the stations were further out onto the ice shelf where temperatures were cooler. As mentioned earlier, two of the wind direction sensors failed. The exact cause is not known as cargo delivery

from the continent has been delayed, however the sensors were working during testing yet never worked once in the field so it is likely they, or their cabling, sustained damage during transport. Only 'guyed mast' designs were used in this deployment.

It was during this season that the work put into simplifying, streamlining, and standardizing all aspects of the physical station design paid off, with up to six fitting into a medium-sized helicopter along with three team-members. Because helicopter time is extremely expensive in Antarctica, the standardized fittings and ease of deployment were very important. The deployment team were able to dismount, unpack, deploy a complete station, pack up, and return to the helicopter in approximately 20 minutes, which meant five or more station could be deployed on a single round-trip of four or five hours (depending on travel time). This meant that 20 stations were deployed over just four half-day slots of helicopter time, which turned out to be very advantageous given the high demand for helicopter time during both deployment and retrieval.

CONCLUSIONS

Operating in the Antarctic environment presents a unique combination of challenges which means full-scale testing of equipment under similar conditions prior to deployment is impossible. Even finding an area with 10 km separation between two points with clear line-of-sight is a challenge in New Zealand, let alone enough space for an entire network. Regardless, it has been shown that it is possible to use off-the-shelf consumer-grade electronics to build reliable weather stations for extreme environments at a significantly reduced cost. While the instrument quality is not as good as high-end commercial weather stations, the observations produced are comparable and the cost savings per station allow the deployment of many more to a given target area. Considerable research, development, and testing of the physical station design have greatly simplified and streamlined the process for erecting them in the field. This makes it possible to transport a number of stations by helicopter and deploy them within a tight time frame. SNOWWEB is now becoming a well-established tool for providing a dense spatial observation network on a campaign basis in Antarctica, and is well-suited for this task.

3

HIGH-DENSITY METEOROLOGICAL OBSERVATIONS IN ANTARCTICA WITH SNOWWEB: A CASE STUDY OF A ROSS ICE SHELF AIRSTREAM (RAS) EVENT

INTRODUCTION

The topography of Antarctica is predominantly featureless, with large expanses of flat or gently sloping ice punctuated by occasional orographic features near the coast. This is largely true for the Ross Ice Shelf (RIS) and surrounding area (Fig.3.1), a very large and flat expanse of grounded and floating ice approximately 900 km wide at its northern edge. The exception to this is the Transantarctic Mountains (TAM), a very tall (2000 - 4000 m above mean sea level (ASL)) and long mountain range, running across Antarctica from the Ross Sea to the Weddell Sea and bordering one edge of the RIS. The large and thick West Antarctic Ice Sheet (WAIS) and East Antarctic Ice Sheet (EAIS) lie on either side of the RIS, rising to several kilometers above sea level with the WAIS sloping relatively gently down to the edge of the RIS and the EAIS terminating at the TAM. Ross Island, the site of Scott Base (NZ) and McMurdo Station (USA), is situated at the north-west corner of the RIS as shown in Figure 3.1. The topography of the area surrounding Ross Island is relatively complex, with Ross Island itself rising to 3800 m ASL at the peak of Mt Erebus and 3200 m ASL at the peak of Mt Terror. White Island and Black Island lie immediately south of Ross Island and, while much smaller, still rise from the ice shelf to 700 m and 1000 m ASL respectively. Immediately south again, Minna Bluff stands at least 800 m tall and protrudes ~50 km out into the RIS from the edge of the TAM, helping to shelter the islands to the north from the prevailing southerly winds.

Radiative cooling of air over ice is common in Antarctica, with the resulting cold, dense, negatively buoyant air descending to the surface. Over flat terrain, such as the RIS, the air will pool and form a temperature inversion with cold air at the surface and warmer air aloft (Connolley, 1996). These temperature inversions add to the highly stable stratification near the surface which enhances the blocking effects of any orographic features, where stable air resists vertical displacement and

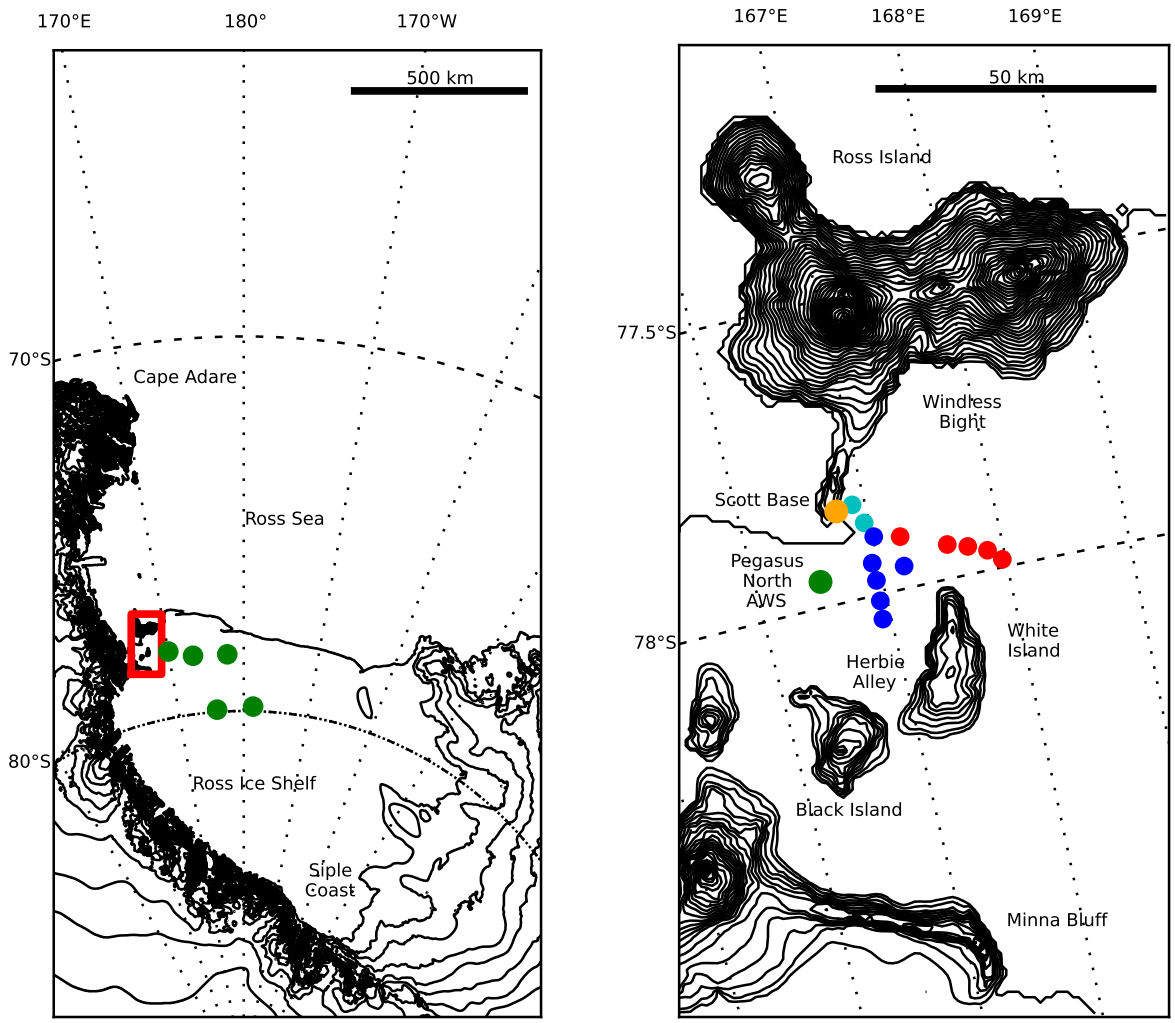

(a) Greater RIS/Ross Sea region

(b) Greater Ross Island region

Figure 3.1:

Maps of (a) the greater RIS/Ross Sea region (250 m contours) and (b) the SNOWWEB deployment area south of Ross Island (100 m contours plus one at 50 m to preserve detail of Hut Point Peninsula). The red box in (a) shows the extent of (b), with the green markers indicating the positions of selected UWAAWS (from left: 'Lorne', 'Emilia', 'Carolyn', 'Vito', 'Gill'). The markers in (b) indicate the location of 'Pegasus North' UWAAWS (named, green), Scott Base (named, orange), and SWS (other colors).

instead tends to flow around topography as shown by Sinclair (1988) and Seefeldt et al. (2003). The WAIS and EAIS, however, are extremely high and roughly dome-shaped so sinking cold air instead begins to flow down the fall line of the terrain, forming what is known as katabatic drainage (or katabatic wind) (Parish and Bromwich, 1986; Parish, 1988; Bromwich, 1989; Renfrew, 2004). As the spatial scales are large, the Coriolis force has a significant effect and deflects the flow slightly to the east of the fall line (Renfrew and Anderson, 2002), however the net effect is still drainage from the interior of the continent toward the coast line. The scale of the Antarctic terrain

is such that a significant amount of air is often displaced by this mechanism, flowing northward from the interior toward the coast and converging through valleys where the wind speed increases (Parish and Bromwich, 1987). This outflow near ground level causes convergence at high altitudes, drawing high altitude air from northern latitudes south over the continent (Parish and Bromwich, 1991, 1998).

One of the most active regions of cyclogenesis in Antarctica is located just off the coast of Adélie Land (Hoskins and Hodges, 2005; Bromwich et al., 2011), ~2000 km north-west of the RIS. The cyclones produced in this area typically propagate to the east then south-east, passing through the Ross Sea and affecting the pressure gradient over the RIS (Bromwich et al., 2011). These systems can initiate strong winds running parallel to the TAM either directly through their own horizontal pressure gradient force (PGF), or indirectly if conditions permit the formation of a 'barrier wind'. These may occur when the horizontal PGF initially directs air toward the TAM; if the boundary layer is stably stratified and the flow does not possess enough kinetic energy to overcome the barrier then mass convergence occurs, creating a PGF directed away from the TAM (Bromwich, 1988; O'Connor et al., 1994; Parish et al., 2006). Under these conditions, winds will become approximately geostrophic and flow perpendicular to the PGF (along the TAM); in the case of the RIS this will always be to the north. As the size of the TAM presents a significant barrier, rising at least 2000 m above sea-level, and the boundary layer in this area is usually stably stratified, barrier winds are extremely common (Parish et al., 2006; Seefeldt and Cassano, 2012). While cyclones in the Ross Sea are a significant contributor to barrier winds along the TAM, recent work by Nigro and Cassano (2014a) using output from the polar-modified Weather Research and Forecasting (WRF) model in the Antarctic Mesoscale Prediction System (AMPS) showed that a PGF conducive to barrier-parallel flow is sometimes produced by the temperature gradient between cold air over the Antarctic plateau and relatively warm air over the RIS instead of cyclones in the Ross Sea or over the RIS.

The combination of southerly barrier winds and katabatic drainage helps to create a wind regime known as the Ross Ice Shelf airstream (RAS), the presence of which is seen in the mean wind field over the RIS in every season (Parish et al., 2006). Characterized by strong southerly winds flowing from the base of the RIS through the western half and out into the Ross Sea, the RAS is responsible for transporting large quantities of cold air from the interior of Antarctica northward (Parish and Bromwich, 1998). The PGF present during the RAS is an important contributor to this drainage, as katabatic winds are primarily driven by a downslope buoyancy force which becomes negligible upon reaching the almost completely flat RIS (Parish and Bromwich, 1998; van den Broeke and van Lipzig, 2003; Renfrew, 2004). The resulting northward transport is highly visible on satellite-based thermal sensors as reported by Bromwich (1989) and Bromwich et al. (1992). While RAS events occur year-round, they are most prevalent (bordering on ubiquitous) during the winter months,

frequent during autumn and spring, and less common during summer (Seefeldt and Cassano, 2012; Nigro and Cassano, 2014b; Coggins et al., 2014) though the exact frequencies differ between studies as each uses a different dataset and RAS definition.

Interaction of the prevailing southerly winds (particularly the RAS) with the terrain around Ross Island is an interesting area of study. The RIS to the south and east of Ross Island is flat and featureless for many hundreds of kilometers, with the exception of the TAM that only help to guide air over this nearly frictionless surface straight toward the collection of islands and bluffs that make up the greater Ross Island area (Fig. 3.1b). Savage and Stearns (1985) provide an overview of the earliest part of what became the UWAAWS network and the first cohesive network of stations near Ross Island. They observed large spatial variation in temperature and winds, with the tendency for the cold and highly stable air on the RIS to move around rather than over the terrain near Ross Island. This effect is strongest in 'Windless Bight' (Fig. 3.1b), an area directly south of Mt Erebus and Mt Terror that experiences abnormally low mean wind speeds throughout the year due to the blocking effect of the mountains (O'Connor and Bromwich, 1988; Sinclair, 1988; Seefeldt et al., 2003). As air flow splits around Ross Island and Windless Bight, the western portion encounters further blocking by Hut Point Peninsula and is often turned again to form the prevailing north-east wind experienced by Scott Base. During strong southerly storms, the intensity of the high pressure zone in Windless Bight intensifies but the extent diminishes and the wind direction at Scott Base on Hut Point Peninsula switches to southerly (O'Connor and Bromwich, 1988; Sinclair, 1988; Seefeldt et al., 2003). In more extreme cases, the barrier winds along the TAM flow over Minna Bluff, creating mountain waves and downslope windstorms north of Black Island with the potential to severely impact the research bases on Hut Point Peninsula (Seefeldt et al., 2003; Powers, 2007; Steinhoff et al., 2008; Chenoli et al., 2015).

Long-term meteorological observation stations are difficult to deploy and maintain in the harsh Antarctic environment. The sparsity of the human population (solely resident in research bases), and the fact they are predominantly located around the edges of the continent, make the use of automatic weather stations (AWSs) a necessity for covering any useful area. Even with the advent of satellite communications, most stations still need to be visited on a regular basis for routine maintenance and to fix faults - a difficult task given the spatial scale and logistical problems presented by Antarctic research. The UWAAWS network (Lazzara et al., 2012) is the largest collection of stations managed by a single organization in Antarctica and provides good coverage of the greater RIS region for large scale analysis. Despite this, the density of stations near the complex terrain of Ross Island is insufficient for small-scale studies. The need for higher density observations led to the development of SNOWWEB, a network of small but complete AWS developed by the University of Canterbury, New Zealand, specifically for Antarctic deployments on a campaign basis (Coggins et al., 2013; Jolly et al., 2013). Designed for easy transportation and

rapid deployment to a relatively small area, SNOWWEB is an ideal tool for augmenting existing AWS networks to temporarily boost the number of observation sites on a campaign basis.

The Antarctic Mesoscale Prediction System (AMPS) (Powers et al., 2012) generates forecasts twice daily for Antarctica and the Southern Ocean. The underlying model is WRF with polar modifications (Polar WRF) developed by the Polar Meteorology Group of the Byrd Polar Research Center at Ohio State University (Bromwich et al., 2013). The primary purpose of AMPS is to provide information for forecasters helping with flight and ground operations of many countries, however its high resolution and good performance mean its output is also used by researchers to supplement available observations. Multiple studies have validated AMPS output as either a primary or secondary objective (Powers, 2007; Nigro et al., 2011, 2012a; Bromwich et al., 2012, 2013) with good results but some degradation of performance near terrain (see also Chapter 4). Bromwich et al. (2005) showed that higher resolution nested grids provide better localized forecasts in areas with more complex topography, while Nigro and Cassano (2014b) showed considerably better results when using the 15 km model grid compared to the 30 km over the RIS. While some studies have investigated the area around Ross Island, the spatial density of available observations is relatively sparse, thus detailed evaluations of the highest resolution domains in AMPS have not been completed (Chapter 4 is currently in review at Monthly Weather Review).

This study investigates surface wind flow in the area between Ross, White, and Black Islands using a dense network of SNOWWEB weather station (SWS) as shown in Figure 3.1b. The SWS were deployed for two months during the 2013/14 summer season as the final of a series of proof-of-concept deployments. Technical issues meant some stations ceased to function after ~11 days, however valuable observations were still collected while the network was at full strength. Section 3.3 shows a comparison between SWS and UWAAWS observations, while Section 3.4 presents data from a RAS event that occurred while all stations were functional. Finally, Section 3.5 compares SWS and UWAAWS observations during the RAS with output from AMPS domain 5 (the highest resolution domain).

METHODS AND DATA

Taylor diagrams

Taylor diagrams (Taylor, 2001) are extremely useful tools for investigating correlation for many points within the context of another variable in a single plot. A typical Taylor diagram plots correlation against standard deviation or normalized root-mean-square difference (NRMSD), with the standard deviation or NRMSD of some reference dataset also included. They are presented

using a polar axis, where the correlation coefficient is the angular coordinate and the other variable (such as standard deviation) is the radial coordinate. Correlation values are normally calculated against a single reference vector which is also used to calculate the reference line on the radial axis. If the radial coordinate is standard deviation then it will ideally place the point close to the reference line, however if it is NRMSD then lower is better.

SNOWWEB observations

The main data source for this analysis is observations acquired by SWS - a re-usable network of AWS purpose-built for Antarctic field work using a custom logger and mechanical design produced by the Department of Physics and Astronomy at the University of Canterbury, New Zealand. Equipped with XBee wireless modules, SWS will automatically form a wireless mesh network based on the IEEE 802.15.4 'ZigBee' standard to pass observations between each other and back to a 'controller'. Designed to be deployed on a campaign basis, each SWS is lightweight and modular with different sensor configurations that can be swapped in the field with no *in-situ* configuration required. This makes deployment and retrieval very fast, a three-person team can perform either task in under 30 minutes and will easily fit into a mid-sized helicopter with five SWS and a pilot.

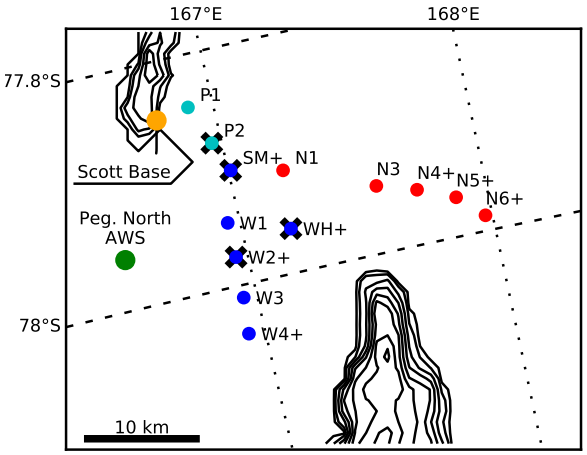

Figure 3.2: Enlargement of SNOWWEB deployment shown in Figure 3.1b with stations labeled. Stations beginning with 'W' or 'S' form the 'west' string and stations beginning with 'N' form the 'north' string (blue and red markers respectively). Cyan markers denote a small string of stations known as 'Pegasus'. Black crosses indicate the station malfunctioned after ~11 days, while the '+' symbol in station names indicates the presence of wind sensors. 'Pegasus North' UWAAWS is represented by the labeled green marker. Station N2(+) failed immediately and is not shown for clarity. Orange indicates Scott Base where the SNOWWEB network 'coordinator' was located.

The SWS deployment observations presented in this analysis cover the austral summer of 2013-14 from the 15th of November to the 7th of January. Fourteen SWS were deployed to the south and east of Scott Base at the southern tip of Hut Point Peninsula on Ross Island (see Figure 3.1). All SWS were equipped with temperature and relative humidity sensors, with eight stations also equipped with anemometers and wind vanes, seven of which are marked on

Figure 3.2 (see caption). The stations were configured to log instantaneous measurements every 10 seconds and send these back to Scott Base over a wireless mesh network consisting of fellow SWS using the IEEE 802.15.4 'ZigBee' standard. All data was also recorded to an internal microSD card as a backup. This was advantageous as the scale of the deployment stretched the network hardware to its limits and resulting data coverage was spotty.

All stations bar one (N2 not marked on maps for clarity) worked extremely well for the first eleven days of the deployment, however at this point a further four stopped responding and were found in an 'endless reset' cycle when recovered. The remaining nine stations, including four with wind sensors, survived until around the 7th of January at which point most of them began to suffer the effects of a very large summer ice melt and the data could not be trusted. The root cause of the initial failures was not found despite post-deployment testing, however both the hardware and firmware of all SWS units were subsequently upgraded and the fault did not reoccur.

During initial analysis of the deployment data, an unrelated electrical fault was found in some of the stations that manifested as unusual wind gusts. Through extensive further analysis and wind tunnel testing it was found that a number of SWS would sometimes incorrectly measure the length of time it would take for a single rotation of the connected anemometer. This happened frequently and randomly, however the erroneous times were always an exact ratio of the correct time (determined by the duty cycle of the anemometer pulse) and always resulted in wind speeds that were substantially too fast. Due to the very high sample rate (six per minute) of the SWS it was possible to not only easily detect the incorrect measurements but also correct the majority of them with very good confidence resulting in little data loss.

The final result of the deployment was eleven days of instantaneous observations every ten seconds from fourteen stations, seven of which were equipped with wind sensors, followed by a further forty-two days of ten-second observations from nine remaining stations, four of which were equipped with wind sensors. This dataset was quality controlled by removing observations more than three standard deviations from the mean for all sensors. Additional quality control was required for the temperature (and associated relative humidity) observations as multiple anomalous observations remained after the initial standard deviation method. Solar radiation bias of temperature observations is a recognized problem in areas with a high ground albedo (snow and ice covered ground) as the radiation may be reflected up through ventilation slats/holes in most common radiation shields (Genthon et al., 2011). The most effective mitigation is to use mechanically-ventilated shields (effectively a box with two pipes and a fan on one pipe), however these are not always viable due to power requirements and reliability issues. An alternative strategy is to simply discard observations that occur when wind speeds are too low to effectively ventilate the shield naturally. Genthon et al. (2011) tested the response of several radiation shields in the Antarctic environment and found a minimum wind speed of 4 to 6 ms^{-1} was likely to be

sufficient to remove most of the solar radiation bias. A 4 ms^{-1} (10 minute rolling window mean) threshold is used as a balance between certainty and coverage, as a 6 ms^{-1} threshold would discard too much data.

UWAAWS observations

UWAAWS, managed by the University of Wisconsin Antarctic Meteorological Research Center (AMRC) (Lazzara et al., 2012) record similar observations to SWS but are designed to be permanently deployed with higher-grade, more expensive, instrumentation and control systems. Most stations use satellite communications, or local wireless networks where possible, to upload data. Unfortunately, some of the data collected over the local wireless network (freewave) is not yet integrated into the semi-automatic quality-control process carried out by the AMRC, so freewave data was processed by the authors using the same quality-control techniques as for SWS data. The final UWAAWS dataset used is a combination of the 'q10' 10 minute quality controlled data product available from the AMRC and freewave data quality-controlled by the authors.

ERA-Interim reanalysis

Output from the ERA-Interim global atmospheric reanalysis (Dee et al., 2011), produced by the European Centre for Medium-Range Weather Forecasts (ECMWF), is used to help establish atmospheric conditions at the synoptic scale while referring to the local scale of the SWS deployment. The ERA-Interim product provides a 0.75° x 0.75° grid of both surface (3-hourly) and upper-atmosphere (6-hourly) products. Global-scale forecast models ingest *in-situ* and remotely-sensed observations and use that data to inform and constrain extrapolation to a regular grid covering the whole globe. ERA-Interim data is known to be reliable at larger scales over the Ross Sea and RIS (Bracegirdle, 2013; Coggins et al., 2014).

Coggins regimes

As a starting point for defining synoptic situations, this study uses the synoptic climatology and regimes developed for the greater RIS/Ross Sea region by Coggins et al. (2014), who used k-means clustering on 10 m winds from the ERA-Interim reanalysis over a 33 year period (1979-2011). Twenty classes were produced and grouped into five regimes based on spatial variability in the mean sea level pressure (MSLP) composite for each class: weak northern cyclonic (WNC), strong

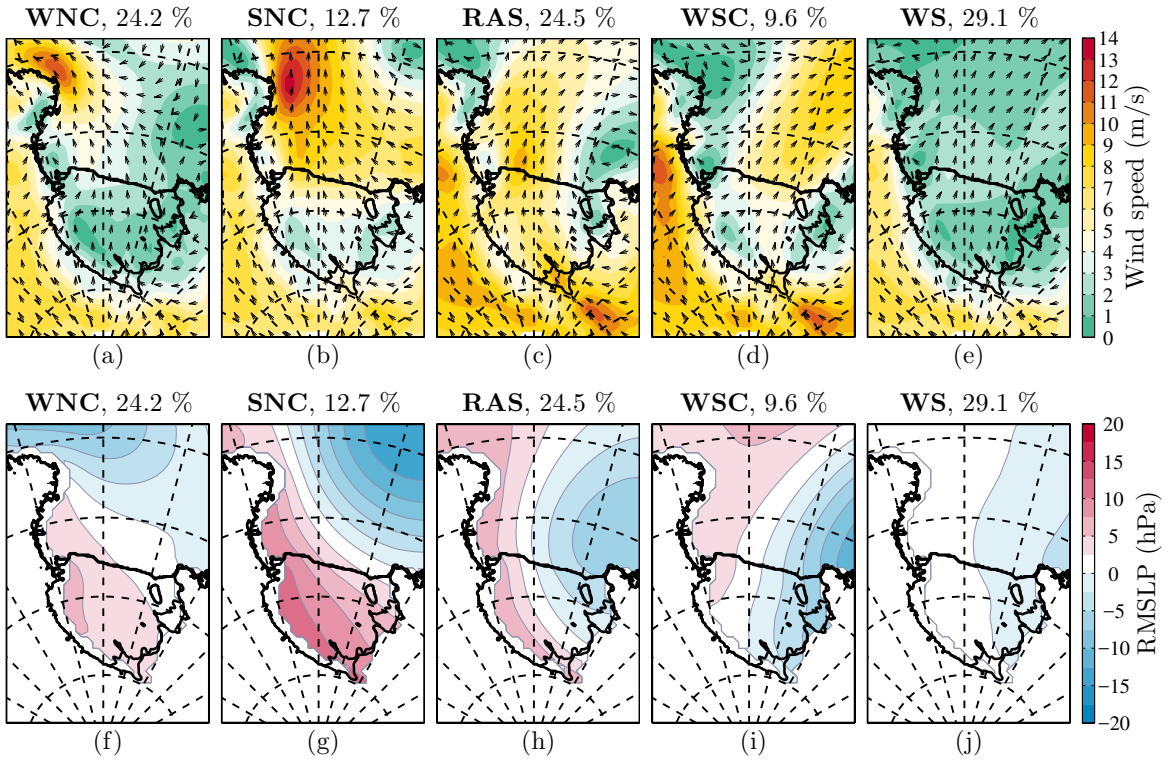

Figure 3.3: Reproduction (with permission) of Figure 2 from Coggins and McDonald (2015), original caption (CMJ2014 = Coggins et al. (2014)): *(a-e) Surface (10 m) winds of CMJ2014 synoptic regimes. Arrows indicate direction in which wind is flowing and are plotted relative to grid north. Background color represents the mean wind speed. Percentages above each diagram display the total frequency of the particular regime, computed annually. (f-j) As in Figure 2a-2e but for relative MSLP. Regime names are the following: WNC = Weak Northern Cyclonic, SNC = Strong Northern Cyclonic, RAS = Ross Ice Shelf airstream, WSC = Weak Southern Cyclonic, and WS = Weak Synoptic.*

northern cyclonic (SNC), RAS, weak southern cyclonic (WSC), and weak synoptic (WS). Coggins and McDonald (2015) created composites of each regime which are reproduced here in Figure 3.3. This study uses the same definition of a RAS as Coggins et al. (2014), which is based on the definition used by Seefeldt and Cassano (2012) - a *pronounced corridor of atmospheric mass transport northward across the RIS and Ross Sea from the continental interior* - but with the extra requirement of *wind speeds being consistently above average within the corridor*.

AMPS domain 5

AMPS features several 'domains' (forecast grids) of varying grid spacings and spatial extent. Domain 1 is the largest and covers the Southern Ocean including the entirety of New Zealand with a 30 km grid spacing, while domain 2 covers the Antarctic continent at 10 km grid spacing. Domain 3 covers a wide area around, and centered on, the RIS with a 3 km grid spacing, while domain 5

covers a 613 km x 718 km (440000 km^2) area centered on the southern edge of Black Island, near Ross Island, at 1 km grid spacing. The Polar WRF model within AMPS exchanges information between these domains so domain 5 benefits from simulations of the wider area at lower resolution and *vice-versa*. This study uses output from domain 5 as it has the finest grid spacing and covers the study area well. These forecasts extend for 40 hours with hourly temporal resolution with a new forecast generated every 12 hours.

To compare AMPS output with SWS observations, 'virtual stations' were constructed by choosing the model grid point closest to each physical station location. Interpolation was not required due to the fine grid spacing of domain 5. The 10 m u and v wind components from AMPS were rotated from the model grid to true north and interpolated to 2 m above ground level (AGL) using a log wind profile with a surface roughness (z_0) parameter of 0.0001 m (Nigro and Cassano, 2014b). As the change in height was small (10 m to 2 m), the atmosphere was assumed to be neutrally stable and therefore there would be no discernible effect on wind direction.

SNOWWEB VALIDATION

As a preliminary step, a brief comparison between observations from the western portion of the SWS network and 'Pegasus North' UWAAWS (see Figure 3.2) is provided. Figure 3.4 shows time-series of observations of wind speed (Fig. 3.4a), temperature at 2 m AGL (Fig. 3.4b), and surface pressure (Fig. 3.5c) for the western portion of the network. The SWS observations are plotted alongside those from Pegasus North which is treated as a reference point. In all, the data compare very well with SWS wind speeds and temperatures largely matching those observed by Pegasus North.

As mentioned in Section 3.2.2, availability of observations from some stations was limited after the first ~11 days of the deployment which is visible in the subplots within Figure 3.4 via the density of lines plotted. Despite this, a southerly storm (RAS) moved through the network during the initial period when all stations were operational so data from this period is still useful. Figure 3.5 displays Taylor diagrams (Taylor, 2001) for wind speed (Fig. 3.5a), temperature (Fig. 3.4b), and pressure (Fig. 3.5c). Due to data availability, only the initial period is used for the wind speed in Figure 3.5a (except red marker for 'W4' SWS), however sufficient data from the entire period was available for the temperature and pressure figures.

The wind speed correlations in Figure 3.5a between SWS and Pegasus North AWS (blue markers) are good, while the standard deviation for each SWS compares very well with Pegasus North for most stations. There is also good agreement between the SWS-Pegasus North points (blue/red) and the SWS-SWS points (green), suggesting that a correlation co-efficient of 0.8 for wind speed

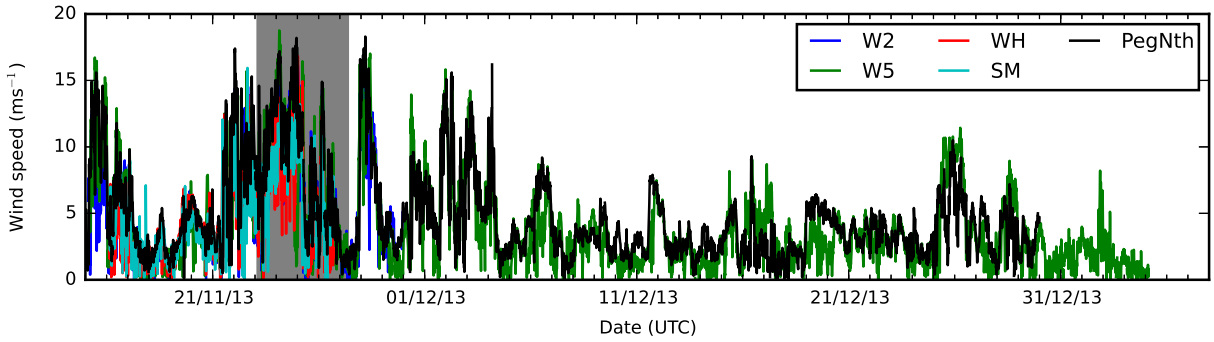

(a) Wind speed

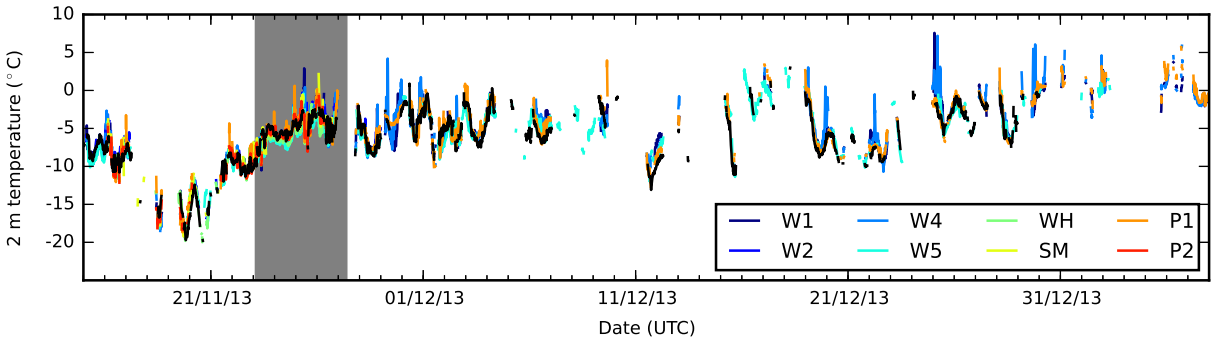

(b) Temperature

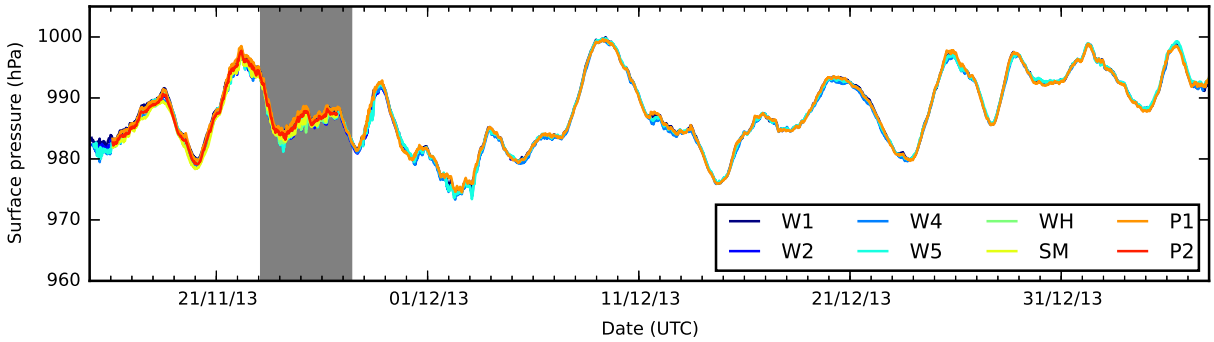

(c) Surface pressure

Figure 3.4: Time-series plots of wind speed (a), temperature (b), and pressure (c) observations from SWS and 'Pegasus North' UWAAWS, where Pegasus North is always depicted using a black line.

is a good expectation over the distances used given the spatial variation in the area. Even better results are obtained for 2 m temperature and surface pressure in Figure 3.5b and Figure 3.5c, with mean correlation coefficients greater than 0.95 and 0.99, respectively, and a similar level of agreement between standard deviations. Thus far, results show that SWS data is reliable and can be trusted for further analysis.

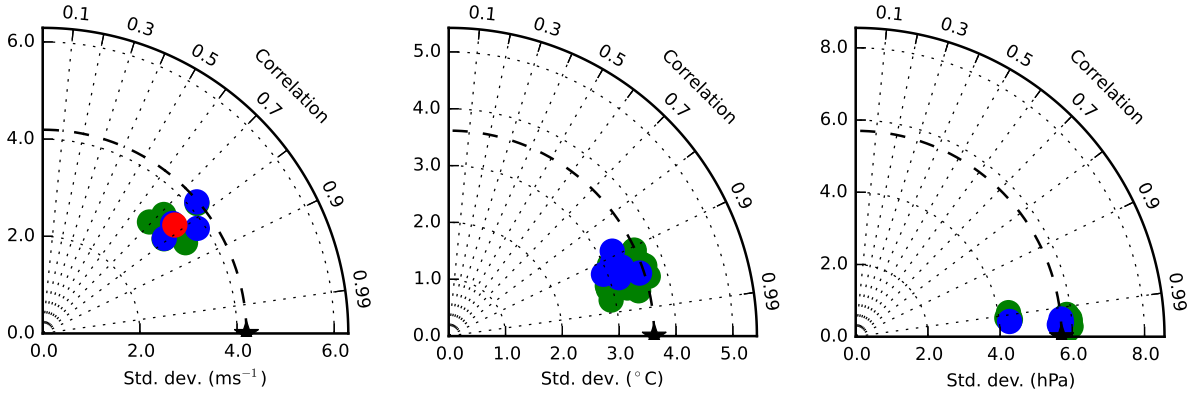

(a) Wind speed (b) Temperature (c) Surface pressure

Figure 3.5: Taylor diagrams of wind speed (a), temperature (b), and pressure (c). Blue markers depict the relationship between Pegasus North UWAAWS and each SWS within ~15 km, while green markers show the relationship between each SWS pair within that group. The standard deviation of observations from Pegasus North is used as the reference (dashed) line in each diagram. The wind speed (a) diagram uses data from the first ~11 days only except for the red marker ('W4' SWS) which used data from the entire period. Temperature (b) and pressure (c) diagrams use data from the entire period.

A CASE STUDY OF A RAS EVENT

Synoptic conditions

During the first 11 days of the deployment, when all SWS were recording observations, a southerly storm occurred over the deployment area. Coggins regime classifications of ERA-Interim re-analysis data over the greater RIS/Ross Sea area were obtained from the authors of Coggins et al. (2014), who extended the original classification period to cover this deployment. The regimes present during an eight day time window centered on the storm period are displayed in Figure 3.6. The storm period can be seen to fall under the RAS regime defined by Coggins and McDonald (2015) (see Figure 3.3(e & h)), specifically Coggins classes '(2,5)' and '(1,4)' (see Figure 3.7). The duration of this almost contiguous set of RAS classifications was four days and six hours, from 0300 hours on November 23rd to 0600 hours on November 27th (UTC), as indicated by the dark gray shading in Figure 3.6. Only a single three hour period breaks the contiguous RAS classifications toward the end, receiving an SNC regime classification instead (class '(3,3)' - see Figure 3.7a). The following analysis covers an eight day period extending two days either side of the RAS classification block, from 0300 hours on November 21st to 0900 hours on November 29th (UTC).

Investigating Figure 3.6 in greater detail, the RAS is seen to originate from a WNC regime present two days prior which further develops into an SNC. The mean relative MSLP depicted in Figure

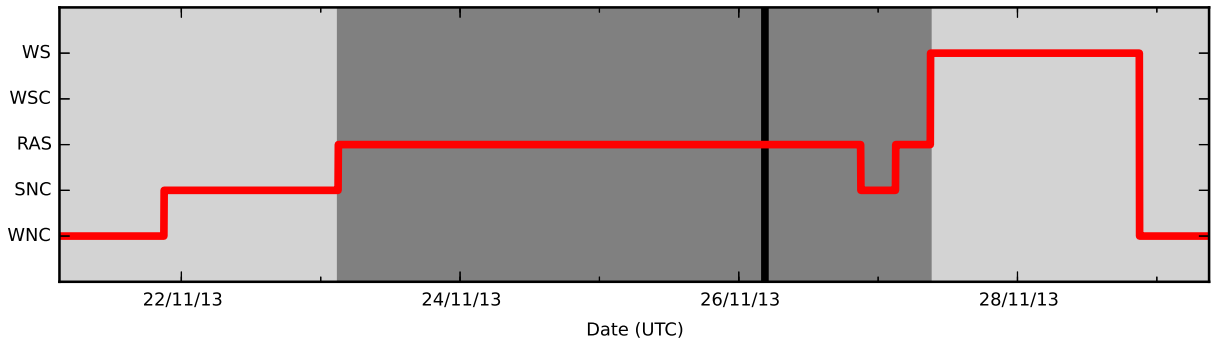

Figure 3.6: Time-series plots of Coggins regimes during greater RAS study period.

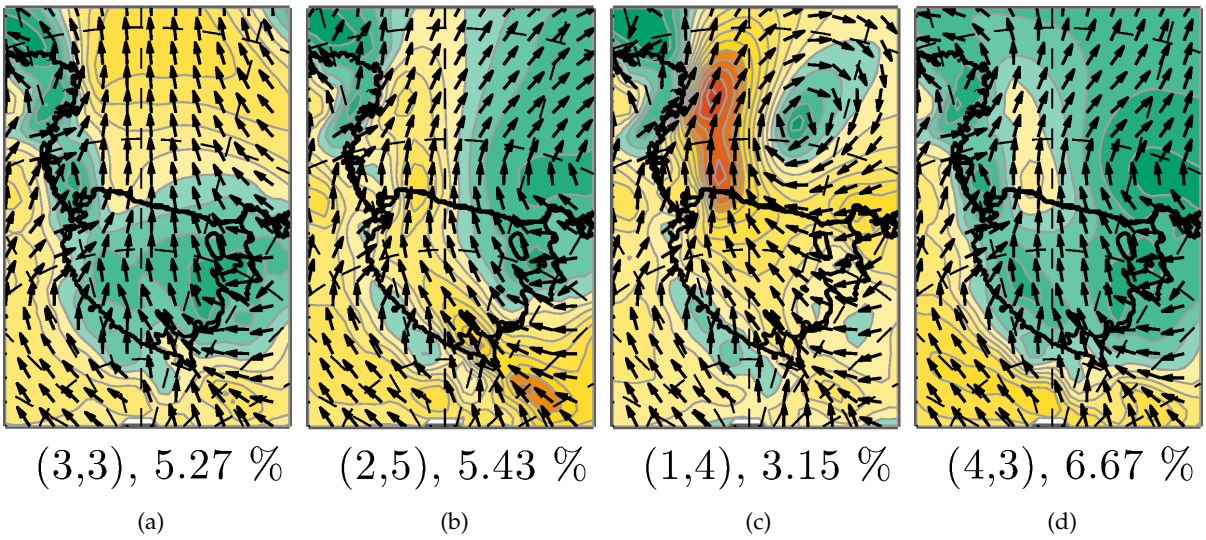

Figure 3.7: Mean wind fields for Coggins classes present prior (a), during (b) & (c), and after (d) the RAS event (2013-11-23 to 2013-11-27). Reproduced with permission from Figure 3 of the study by Coggins et al. (2014).

3.3(f-h) shows that this typically presents a situation with a low pressure system to the north of Cape Adare (Fig. 3.1a) which deepens and moves south and east. As the RAS finishes, the logical progression is through regimes WSC and WS as the system moves further east along the coast, however in this case Figure 3.6 shows a jump straight from the RAS regime to the WS regime.

The actual progression of the synoptic pressure gradient according to the ERA-Interim reanalysis is shown in Figure 3.8, with the sub-figures arranged in chronological order. Figure 3.8a shows the synoptic MSLP situation at the beginning of the extended study period identified above. There is a relatively deep low pressure system sitting well north of the RIS with a small pressure gradient over the ice shelf, hence the WNC Coggins regime classification in Figure 3.6. As this system moves eastward to the south and east the regime classification changes to SNC then RAS, with Figure 3.8b showing the situation at the start of the RAS classification block. As the RAS intensifies the synoptic pressure gradient increases to the maximum point shown in Figure 3.8c before

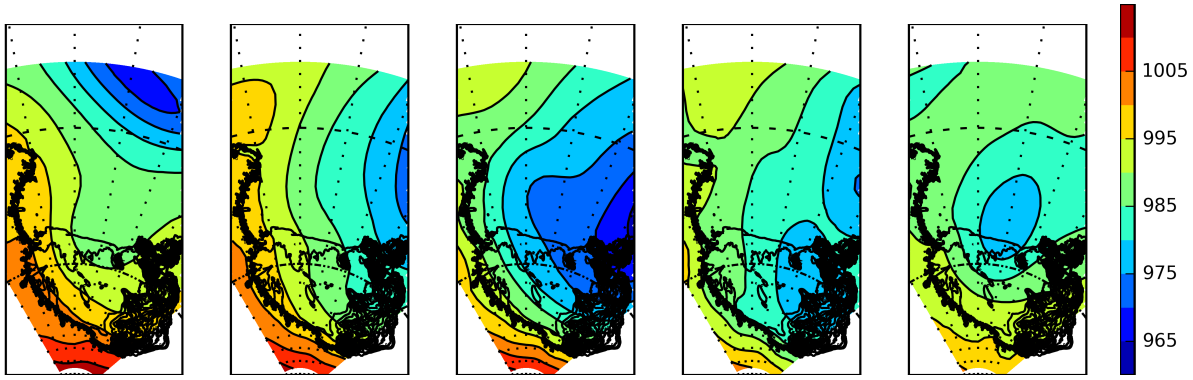

(a) 21-11 0300 WNC (b) 23-11 0300 RAS (c) 24-11 0300 RAS (d) 27-11 0300 RAS (e) 28-11 0000 WS

Figure 3.8: MSLP (hPa) from ERA-Interim reanalysis for five key moments: (a) beginning of study period, (b) start of RAS, (c) highest RAS wind, (d) lowest RAS wind, (e) peak wind after RAS.

diminishing to the minimum in Figure 3.8d. Figure 3.8e is a snapshot of the MSLP field during the WS regime that followed the RAS, where a minor low pressure system that can initially be seen over the far eastern portion of the RIS in Figure 3.8d has developed and moved north-west and over the Ross Sea.

Local wind conditions

As the RAS develops in Figure 3.6, Figure 3.9a shows an increasing wind speed throughout the network. This is mirrored at a larger scale by Figure 3.10, which shows wind speeds from five UWAAWS spread over the western half of the RIS (green markers in Figure 3.1a). During the RAS itself, the SWS network observed elevated wind speeds for about half of the classified RAS period, with two lulls toward the end broken by a very short burst of high winds (addressed below in Section 3.4.3). Interestingly, there was a substantial increase in wind speed for a period of almost a day after the RAS ceased while the WS regime - typically associated with minimal synoptic forcing and low wind speeds - was in effect. The likely cause of this is the cyclone seen in the ERA-Interim MSLP field in Figure 3.8e which will have created higher wind speeds over a more localized region of RIS, thus escaping the classification of a faster Coggins regime which takes a far wider area into account.

The most likely explanation for the lulls seen in Figure 3.9a during the RAS is that the main stream of high winds simply moved away from Ross Island toward the center of the RIS. The low level jet usually present during a RAS is known to move around the RIS (Seefeldt and Cassano, 2012; Coggins et al., 2014) and even relatively small directional shifts at the scale used by the Coggins regimes could have large impacts on the very small scale of the SWS deployment. This

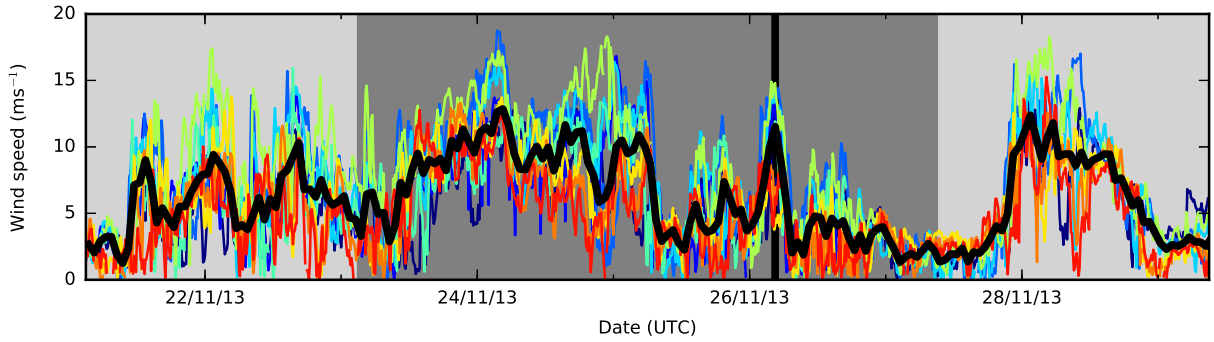

(a) Wind speed

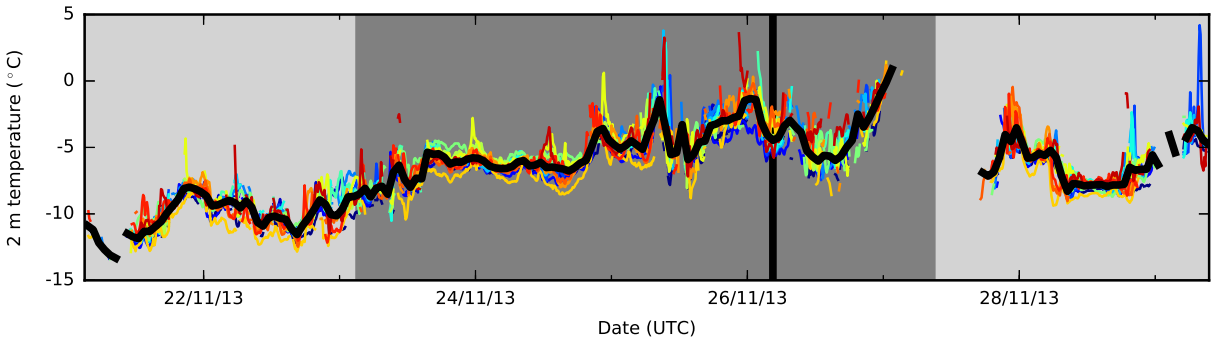

(b) Temperature

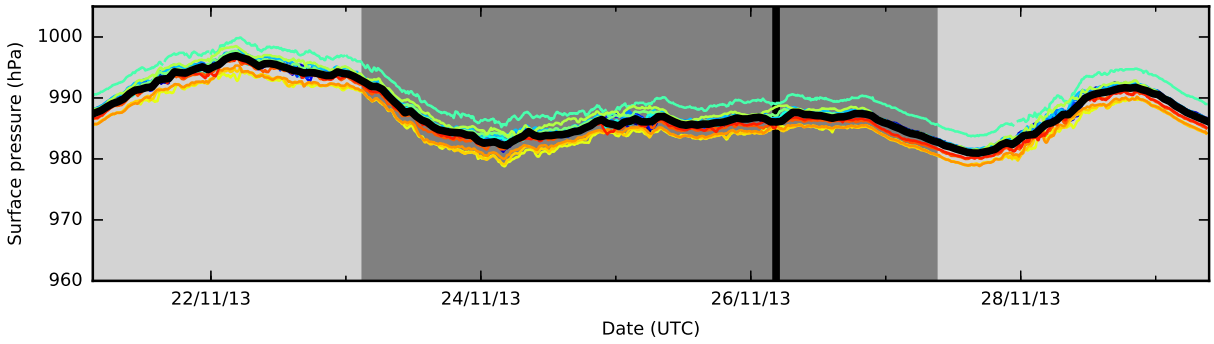

(c) Surface pressure

Figure 3.9: Wind speed (a), temperature (b), and pressure (c) observations from the SWS network. Cool colors denote 'west' string SWS and warm for 'north' consistent with Figure 3.2. Hourly medians are depicted by a thick black line. Dark gray shading indicates 'RAS' period in Figure 3.6. The black vertical line indicates an interesting wind speed peak.

is supported by the UWAAWS deeper inside the RIS (green markers in Figure 3.10) which show a gradual decrease in wind speed over the period instead of the sharp drop (and brief renewal) seen by the SWS.

Southerly winds and in particular RAS events are known to be associated, perhaps counter-intuitively, with warmer temperatures. This is consistent with the SWS observations in Figure 3.9b which show relatively cold temperatures before the RAS begins, followed by steadily increasing temperatures throughout the course of the RAS. The rising temperatures during a RAS

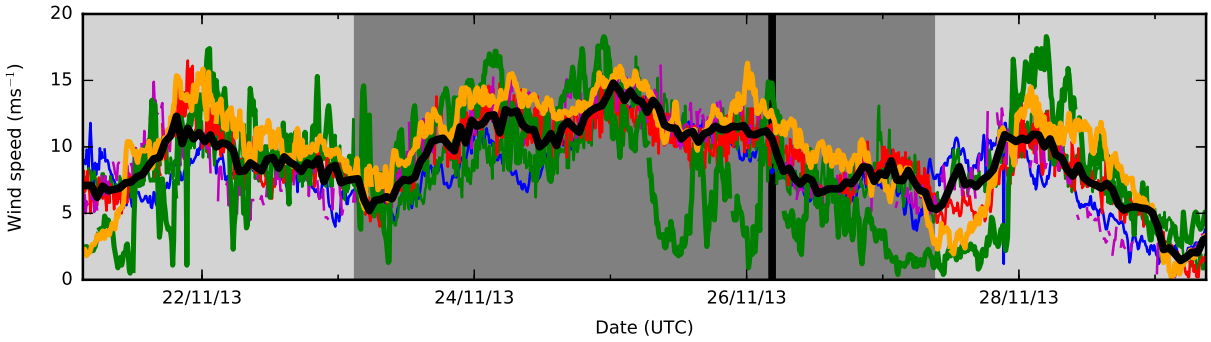

Figure 3.10: Wind speed observations from selected UWAAWS (see Figure 3.1b). 'Pegasus North' and 'Lorne' are shown in green and orange, respectively, with other stations illustrating spread only. Hourly medians are depicted by a thick black line. Dark gray shading indicates 'RAS' period in Figure 3.6. The black vertical line indicates an interesting wind speed peak.

are normally linked to substantial turbulent vertical mixing due to the high wind speeds which destroys the inversion layer typically found at the surface (Riordan, 1977; Bromwich et al., 1993; Lüpkes et al., 2008). The presence of cloud during a RAS also contributes down-welling long-wave radiation and effectively block the radiative cooling associated with formation of temperature inversions. There is a large 'hole' in the temperature observations at the end of the RAS which is caused by the quality-control systems of both the Pegasus North UWAAWS data and the SWS data. Wind speed is universally low during this period which greatly increases the risk of a positive temperature bias due to reflected solar radiation infiltrating the radiation shields at each station, where sufficient ventilation will mitigate this to a reasonable level (see Section 3.2.2 and the work of Genthon et al. (2011)).

Acceleration between White and Black Islands

The sudden increase in wind speeds seen during the latter part of the RAS period in Figure 3.9a highlights an interesting feature of the complex local terrain present within the study area (Fig. 3.1b). Severe and localized southerly wind storms in this region are colloquially known as 'Herbies', with the area that most frequently experiences the worst of these bearing the name 'Herbie Alley' (indicated on Figure 3.1b). This area is positioned in the narrow gap between White Island and Black Island, which act to force southerly and south-easterly winds through the narrow constriction, sometimes resulting in high wind speeds. The presence of Minna Bluff to the south may help to reduce the frequency of these events somewhat as it provides blocking for south to south-westerly winds when wind speeds are too low to overcome the barrier.

The interesting increase in wind speed occurs over a four hour period centered on 0430 hours on November 26th (UTC) and is indicated in previous figures by a vertical black line. Figure 3.11

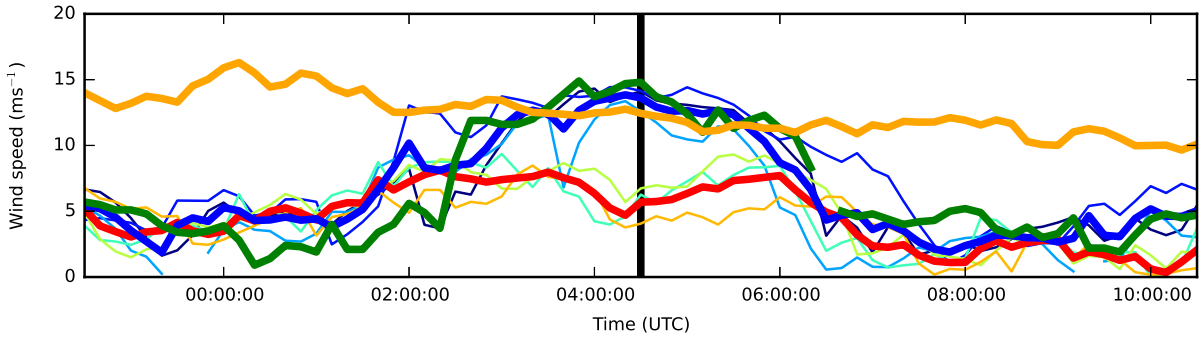

(a) Wind speed

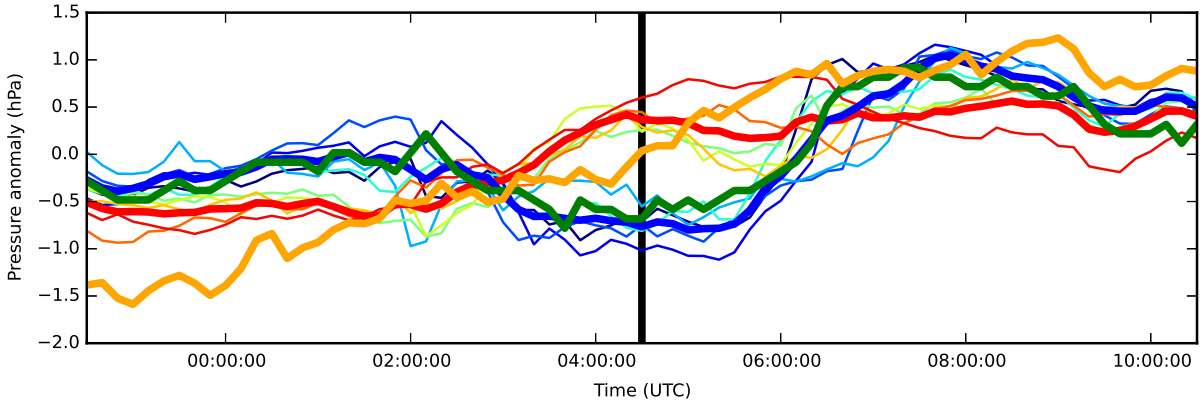

(b) Surface pressure anomalies

Figure 3.11: Time-series of SWS and Pegasus North UWAAWS wind speed (a) and pressure anomaly (b) observations during peak wind speed on the 26th of November, 2013. Data from Pegasus North and Lorne are shown by thick green and orange lines (respectively) in both plots. Two groups of SWS are shown by the use of cool/blue (western string close to Pegasus North) and warm/red (northern string above White Island) colors consistent with Figures 3.9 and 3.2. Thicker blue/red lines are group means.

shows the observed wind speed and pressure anomaly from two groups of SWS stations - 'north' and 'west' - and Pegasus North UWAAWS. The 'north' group of stations passes above White Island in Figure 3.2 and are represented with 'warm' (red) colors in Figure 3.11. The 'west' group passes to the west of White Island toward Herbie Alley and are marked with 'cool' (blue) colors.

Figure 3.11a shows the elevated wind speed first seen in Figure 3.9a does not extend to the entire network and is predominantly experienced by the west (blue) group of stations along with Pegasus North UWAAWS (green) - this is expected given the close proximity of Pegasus North. The north (red) group do show a slight elevation in wind speed but the result is less than half of the speed seen to the west - in fact there is a lull in the north string at the point where the west string experiences the maximum wind speed. Winds at Scott Base and McMurdo Station (not shown) do increase during this period but the magnitude is so small that this is barely visible above the baseline (only 1 - 2 ms^{-1}). Lorne UWAAWS, located just to the east of the area in Figure 3.1b (see

Figure 3.1a) shows a very slight decrease in wind speed during this time but is largely unchanging. Wind speeds observed by Minna Bluff UWAAWS (not shown) are decreasing and similar to those at Lorne but 3 - 5 ms^{-1} faster. This further indicates that the wind speeds seen over the SWS network are local in nature and likely induced by the terrain.

Anomalies in surface pressure (from the station mean) are calculated for each station and are included in Figure 3.11b. There is a decrease in pressure for the west string and Pegasus North during the higher wind speed period, while the north string experiences an increase which is later matched by the west string and Pegasus North after the high wind speeds dissipate. A consistent overall increase in pressure is observed by Lorne UWAAWS over the period. The decrease in pressure in the direction of the flow of the wind through a constriction (between the Islands) is consistent with a gap wind, where a damming effect on the upwind side increases pressure and air flows ageostrophically through the constriction in the direction of the pressure gradient. In this case the spatial scale is much smaller than typical examples (Overland and Walter, 1981; Jackson and Steyn, 1994; Gaberšek and Durran, 2004).

PERFORMANCE OF AMPS DOMAIN 5 FORECASTS DURING A RAS EVENT

The presence of the RAS event shown above provides a good opportunity to investigate AMPS domain 5 which features the finest grid spacing (1 km) of all the AMPS domains. Figure 3.12 gives an overview of observed and modeled wind speeds for three station locations during the RAS event. Overall the AMPS forecasts follow the general pattern of the observations well, however there are some deviations, with frequent over-estimations of wind speed and variability at N6 (Fig.3.12a) and under-estimations of speed at W4 (Fig.3.12b) and Pegasus North (Fig.3.12c). Network correlation coefficients (Fig.3.13a) and mean root-mean-square difference (RMSD) (Fig.3.13b) by forecast hour for wind speed are relatively consistent throughout. The worst performing block is hours 12-23 which is actually the preferred block to use when building a time-series from multiple forecasts (Guo et al., 2003; Bromwich et al., 2005; Seefeldt and Cassano, 2012; Nigro and Cassano, 2014b), however it must be noted that the short duration of the period limits extrapolation to longer periods or wider study areas.

While various wind speed peaks were predicted by AMPS during the RAS, none aligned with the sudden resurgence discussed above in Section 3.4.3. Interestingly, there appears to be a strong link between peaks seen at both W4 and N6, located 25 km apart with White Island in between them, but these same peaks are not seen at Pegasus North which is only 13 km from W4. Additionally, the observational records from these two stations are more closely linked than W4 is with N6. The net result is that AMPS does not appear to forecast any gap winds between White Island and

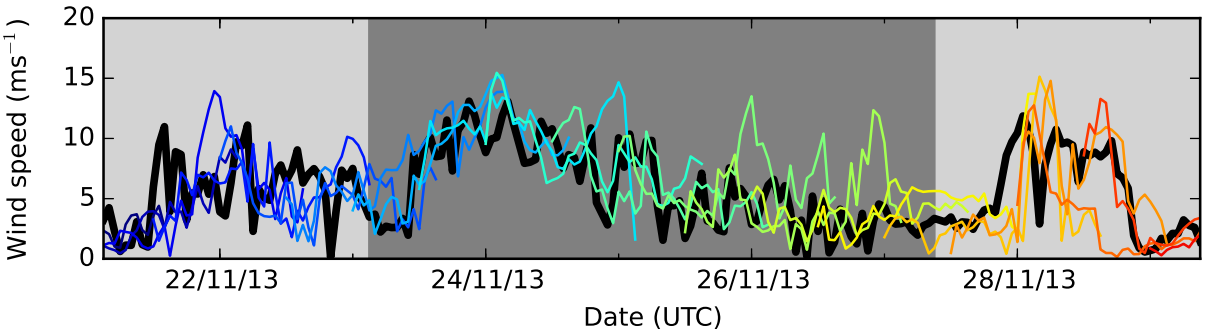

(a) N6 wind speed

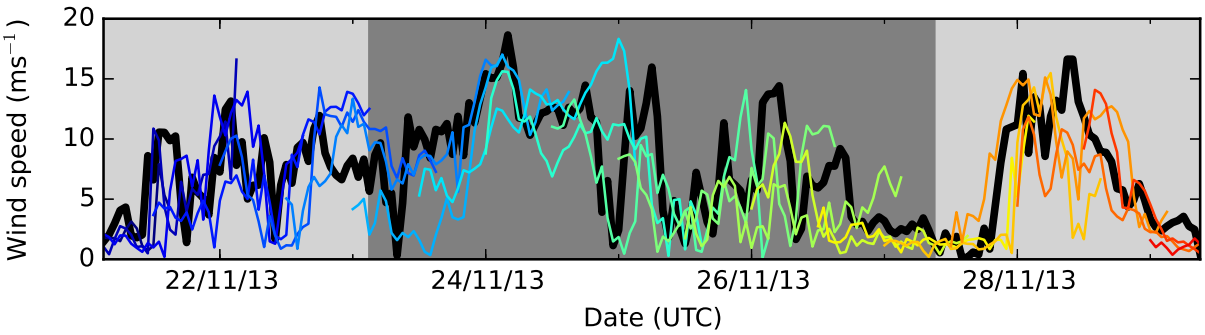

(b) W4 wind speed

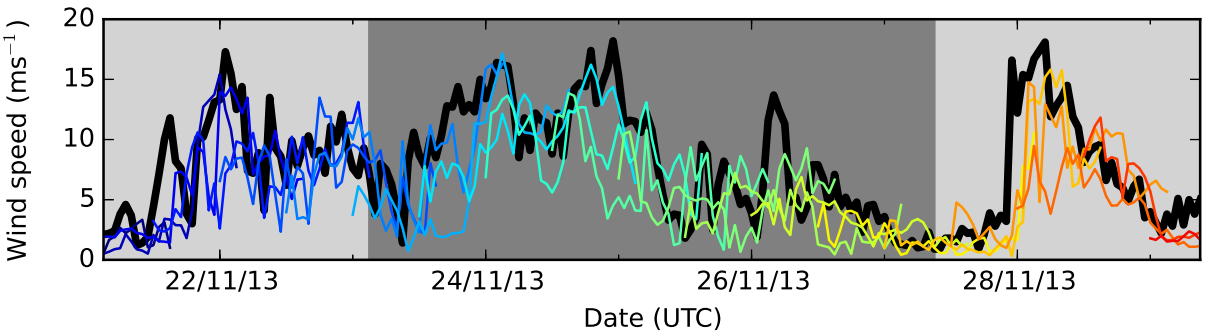

(c) Pegasus North wind speed

Figure 3.12: Time-series plots of observed (thick black line) and AMPS forecast (multicolored) wind speed for N6 (a), W4 (b), and Pegasus North (c) weather stations. The dark gray background shading indicates the RAS event period.

Black Island, though it should be noted that the very short duration and localized nature of the event greatly increase the challenge presented to the model.

An interesting point of difference between AMPS and AWS observations at a wider scale occurs in the temperature data (Fig. 3.14), where AMPS shows a strong diurnal cycle throughout the RAS that is not seen in the observations. By November, sunlight is present 24-hours a day at the latitude of the study location, however there is sufficient variability in angle and intensity to produce a noticeable diurnal cycle. The ubiquitous Antarctic temperature inversion plays a role in this cycle, where lower level air radiatively cools while the sun angle is lower and is then warmed as the

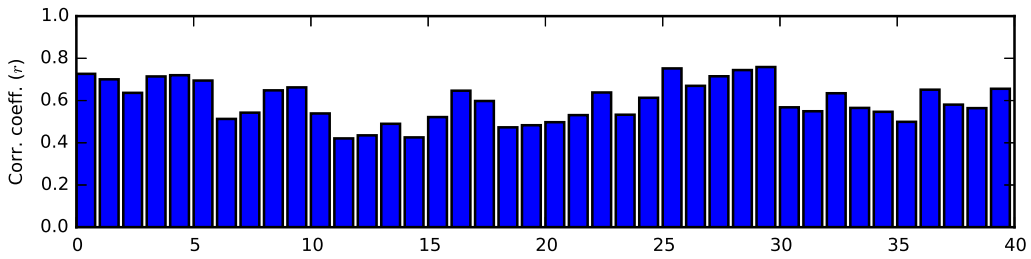

(a) Correlation coefficient

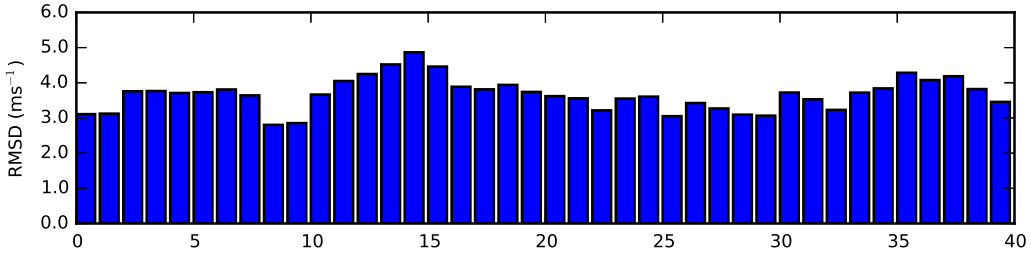

(b) RMSD

Figure 3.13: Wind speed correlation (a) and RMSD (b) between AMPS and station observations by forecast hour

sun elevation angle increases. During high wind events, however, the magnitude of this cycle is diminished as high wind speeds, turbulence and often associated cloud suppress the cooling effect and prevent the formation of the inversion. During this particular RAS event the diurnal cycle is practically non-existent for the first two days, a fact observed by both SWS and UWAAWS in the study area but not reflected by AMPS. This effect is localized, though, as UWAAWS further out on the RIS still show a visible diurnal cycle (figure not included). The large differences (~10°C) that can be observed toward the end of the RAS are very likely caused by the initial conditions given to AMPS, given they occur at the beginning of the forecast and are quickly warmed to similar levels seen in the observations.

SUMMARY AND CONCLUSIONS

This study has presented results from a largely successful SNOWWEB deployment - while six of the fifteen stations failed prematurely they still recorded valuable observations during a RAS event. While the failures that occurred during the season presented here could not be fully diagnosed, the subsequent generation of hardware and firmware that built on the experience of this season did not experience such problems (resulting data presented in Chapter 4). All SNOWWEB stations performed very well when functional, recording and transmitting data that compared well with other available observations in the area, with the time-series plots in Figure 3.4 showing good

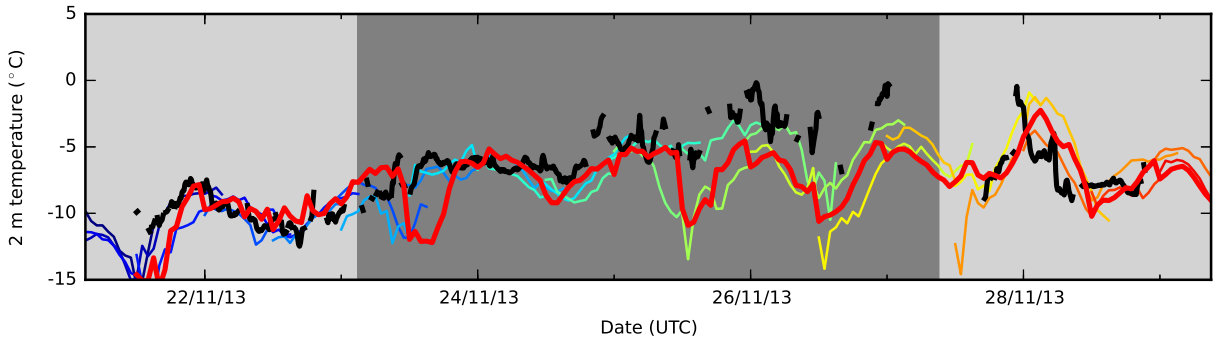

(a) N4 2 m temperature

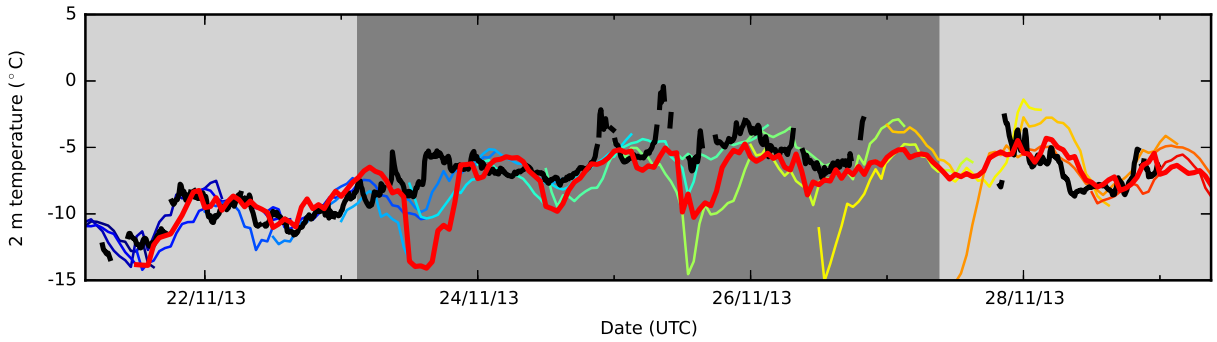

(b) W4 2 m temperature

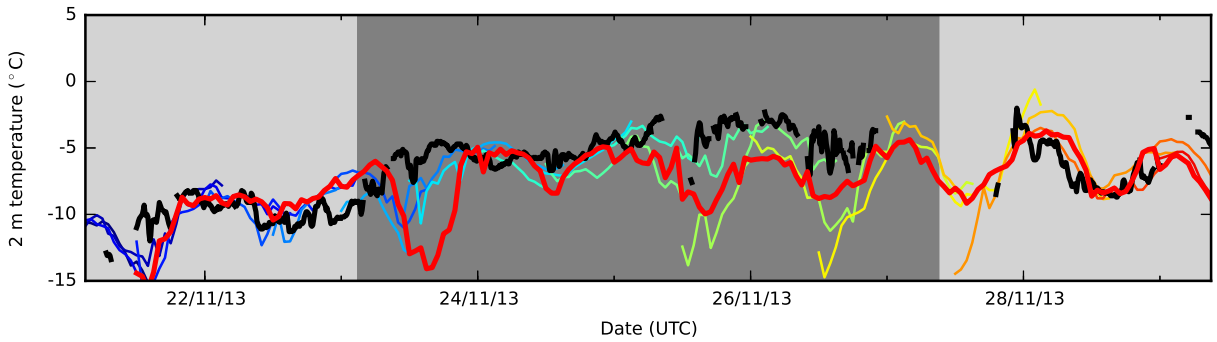

(c) Pegasus North 2 m temperature

Figure 3.14: Time-series plots of observed (thick black line) and AMPS forecast (multicolored) 2m temperature for N6 (a), W4 (b), and Pegasus North (c) weather stations. The dark gray background shading indicates the RAS event period.

agreement at a glance. Figure 3.5 confirms this in more detail by showing SWS correlate as well with Pegasus North UWAAWS as they do with each other, implying most of the differences between observations are due to spatial variance.

The regimes identified by Coggins et al. (2014) and Coggins and McDonald (2015) provide good synoptic context for a network of weather stations focused on local-scale weather. The identification of the RAS event largely matched what was seen by SNOWWEB but local variability even during a relatively stable and strong synoptic scale event was obvious. This was illustrated by differences between the stations south of Ross Island in Figure 3.9a and the UWAAWS to the east

in Figure 3.10 during the latter half of the RAS. The two lulls seen by SNOWWEB and Pegasus North during this time were not fully reflected by the other UWAAWS on the RIS, indicating that the corridor of high winds of the RAS shifted away from Ross Island. The sudden spike in wind speeds seen by both SNOWWEB and Pegasus North suggest that the corridor briefly moved back toward Ross Island as the wider UWAAWS network does not show a similar increase, in fact the spike coincides with the beginning of a decrease in wind speed over the wider area.

Further investigation of the sudden increase in wind speed shows that it was not observed over the entire SNOWWEB network, with the 'north' string of stations (Fig.3.2) showing a relatively minor increase in wind speed compared to the 'west' string (plus Pegasus North) as shown by Figure 3.11a. The surface pressure observations at each station also show an interesting separation between the north and west strings which experienced a minor increase (~0.5 hPa) and a shallow drop (~0.5 hPa) respectively during the peak wind speed, returning to relative agreement shortly afterward. For both wind speed and pressure, the closest UWAAWS from Figure 3.10 (Lorne) shows relatively constant decreases and increases respectively. The differences in wind and pressure between the two strings of SNOWWEB stations (plus Pegasus North) suggests the presence of a gap wind (Overland and Walter, 1981; Gaberšek and Durran, 2004) between White Island and Black Island at this time, where the decrease in surface pressure occurs with the rise in wind speed, albeit at a relatively small scale.

Unlike the strong wind events in this region covered by other studies (Steinhoff et al., 2008; Chenoli et al., 2012, 2015), the sudden increase in wind speed is not associated with flow over Minna Bluff or downslope wind storms, nor does it even reach McMurdo station. Regardless, it is still important as it propagates as far as Pegasus North UWAAWS on the edge of Pegasus Runway - the main airfield in the area for most of the year - with wind speeds greater than the 7 - 13 ms^{-1} threshold for blowing snow (Holmes et al., 2000) which can constitute a major visibility hazard for aircraft attempting to use the airfield. While the wind speed increase is relatively short-lived at ~3 hours, this is sufficient time to cause a hazard to aircraft operations if the runway is obscured while aircraft are en-route (see report by McClelland (2014) covering an incident caused by fog earlier in the same season).

AMPS output from larger domains is known to degrade near complex terrain (Nigro et al., 2011; Bromwich et al., 2013), with a common explanation being an inability to resolve this terrain for a given model grid size. While AMPS showed good general agreement with observed wind speeds during the RAS there were some obvious differences between the forecasts and observed conditions. The gap wind recorded by the 'west' string of stations was not reflected in any of the AMPS output, and earlier forecast increases in wind speed that did not eventuate were inconsistent with the observed spatial relationships between stations with increase at both the west and north string but not at Pegasus North UWAAWS. It is recognized that these events are hard to

correctly forecast as they are transient and localized, however their potential impact is significant, where previous effort has been made to forecast these events using UWAAWS data (Holmes et al., 2000). AMPS also did not predict the decreased magnitude (flattening) of the diurnal signal in temperature observations over the SWS network (and nearby UWAAWS), though again it appears this effect was localized to the vicinity of Ross Island as UWAAWS further out on the RIS were unaffected (and featured better correlations). The local nature of both the gap wind and smoothing of the diurnal cycle suggest that Polar WRF within AMPS is not correctly simulating the boundary layer processes in this area of complex terrain. It is very likely that poor initial conditions play a part, with temperature values during early forecast hours showing a very large disconnect from observations (Fig. 3.14).

4

A VALIDATION OF THE ANTARCTIC MESOSCALE PREDICTION SYSTEM USING SELF-ORGANIZING MAPS AND HIGH DENSITY OBSERVATIONS FROM SNOWWEB

INTRODUCTION

The Ross Ice Shelf (RIS) is a largely flat expanse of permanent ice covering approximately 487,000 km^2. Straddling the date line, it is fed by both the West and East Antarctic Ice Sheets (WAIS and EAIS respectively). The western edge of the roughly triangular-shaped shelf is bounded by the barrier of the Transantarctic Mountains (TAM), with the EAIS behind. Katabatic winds from the EAIS converge through multiple glacial valleys in the TAM (Bromwich, 1989), while corresponding drainage from the WAIS flows onto the eastern and southern edges of the RIS at the Siple Coast (Bromwich and Liu, 1996; Bromwich et al., 1992). This katabatic drainage is known to move significant quantities of air onto the RIS from the interior of Antarctica (Parish and Bromwich, 1987, 1997, 1998). In combination with meso- or synoptic- scale cyclones and the barrier presented by the TAM, the katabatic drainage helps to feed a southerly wind regime that dominates the climatology of the RIS. Known as the Ross Ice Shelf airstream (RAS) (Parish et al., 2006), the presence of this low-level stream of air can be seen in mean surface wind field plots from monthly to annual time scales.

The signature of the RAS is a corridor of high winds flowing north, parallel to the TAM and out into the Ross Sea. There is no single consistent source of atmospheric forcing for a RAS (Parish et al., 2006; Seefeldt and Cassano, 2012; Nigro and Cassano, 2014a), however these events are often initiated by a low pressure system at meso- or synoptic scale, either north of the RIS in the Ross Sea or over the ice shelf itself. These systems create barrier-parallel flows relative to the TAM during a RAS either directly through their own horizontal pressure gradient force (PGF), or indirectly if conditions permit the formation of a 'barrier wind'. These winds form when the horizontal PGF initially directs air toward the TAM; if the boundary layer is stably stratified and the flow does not possess enough kinetic energy to overcome the barrier then mass convergence

occurs, creating a PGF directed away from the TAM. Under these conditions, winds will become approximately geostrophic and flow parallel to the Mountains; in the case of the RIS this will always be to the north as the PGF is directed toward the east, away from the Mountains. The size of the TAM presents a significant barrier, rising to 2000 m above sea-level, and the boundary layer in this area is usually stably stratified, therefore barrier winds are extremely common (Parish et al., 2006; Seefeldt and Cassano, 2012). Recent work by Nigro and Cassano (2014a) using output from the polar-modified Weather Research and Forecasting (WRF) model in the Antarctic Mesoscale Prediction System (AMPS) showed that a PGF conducive to barrier-parallel flow is sometimes produced by the temperature gradient between cold air over the Antarctic plateau and relatively warm air over the RIS instead of cyclones in the Ross Sea or over the RIS.

Another feature that is commonly present during a RAS event is katabatic drainage from the surrounding ice sheets (Seefeldt and Cassano, 2012; Coggins et al., 2014; Nigro and Cassano, 2014a). These winds are formed when air over the ice sheets is cooled, typically radiatively or via sensible heat flux into the ice surface, and becomes negatively buoyant at the surface, generating a force directed along the fall line of the terrain. Accounting for the frictional and Coriolis forces, the air flows approximately down and to the left of the fall line of the terrain, with the exact direction influenced by the background pressure gradient force (Parish and Cassano, 2003). The WAIS and EAIS are both extremely large and approximately dome-shaped with high interior elevations dropping to sea-level at the edges. Radiative cooling at the surface of the ice sheets resulting in katabatic drainage is extremely common, with the ensuing winds sometimes reaching very high speeds at the edges of the sheets - particularly when forced into confluence zones such as glacial valleys (Parish and Bromwich, 1987, 1997, 1998). These winds are widespread, persistent, directionally constant, and capable of transporting extremely large volumes of air from the interior of Antarctica northward to the coast. Once a katabatic flow reaches a large expanse of level terrain, the katabatic (downslope buoyancy) force reduces and, in the absence of another source of forcing, the air will pool and begin to impede further drainage (van den Broeke and van Lipzig, 2003; Renfrew, 2004). A typical RAS event provides the ideal pressure gradient force to transport this air further north, over the RIS and the Ross Sea. Because the RIS (and RAS) is positioned between the EAIS and WAIS, a significant mass of air from the interior of both sheets is transported to the RIS and therefore available for further transport into the Ross Sea. A case study by Parish and Bromwich (1998), investigating a significant drop in surface pressure over the Antarctic continent, identified the RIS as the destination for katabatic drainage from approximately one-third of the entire Antarctic continent (by surface area) during the event.

The Antarctic Mesoscale Prediction System (AMPS) (Powers et al., 2012) generates forecasts twice daily for Antarctica and the Southern Ocean. Currently, it utilizes the WRF model with polar modifications (Polar WRF) developed by the Polar Meteorology Group of the Byrd Polar Research

Center at Ohio State University. While AMPS provides valuable forecast data for the flight and ground operations of many countries, its output is also used by researchers over longer time scales to supplement available observations from both staffed and automated weather stations. Multiple studies have validated, as either a primary or secondary objective, AMPS output for both the older MM5 model (Bromwich et al., 2005; Guo et al., 2003) and the newer Polar WRF model (Powers, 2007; Nigro et al., 2011, 2012a; Bromwich et al., 2012, 2013). AMPS forecasts compare very well with observations from the interior regions of Antarctica, where the terrain is rather uniform. Along the coast, AMPS forecasts still compare favorably with observations, however it is clear that adequately resolving terrain is extremely important. This has a significant effect on winds in areas with complex topography, where higher resolution nested grids provide better localized forecasts (Bromwich et al., 2005). Most recently, Nigro and Cassano (2014b) calculated correlations between AMPS and 12 weather stations over the wider RIS area and showed considerably better results when using the 15 km model grid compared to the 30 km. While some of these studies have investigated the area around Ross Island, the spatial density of available observations is relatively sparse, thus detailed evaluations of the highest resolution domains in AMPS have not been completed. This study refers to, and validates, forecasts produced by the AMPS system as a whole rather than the underlying Polar WRF model specifically. The free availability and range of high resolution nested grids make AMPS a viable data source for researchers and forecasters alike, so performing a holistic validation of the system will be of value to others in the community.

The air, sea, and land operations around Ross Island require accurate weather forecasts, which is why the highest resolution AMPS nested grids are situated over this area. Fine grid spacings also assist in resolving some of the complex terrain in the region, where the effect of this terrain on wind patterns in the area is interesting in and of itself (e.g. O'Connor et al., 1994; Seefeldt et al., 2003; Monaghan et al., 2005; Powers, 2007). The RAS commonly passes close to Ross Island (Parish et al., 2006; Coggins et al., 2014; Nigro and Cassano, 2014a), where its impact on the nearby Ross Sea Polynya is the subject of ongoing research associated with this study. These factors, combined with easy physical access via the nearby research bases makes studying this area an attractive prospect. The SNOWWEB network of weather stations (Coggins et al., 2013; Jolly et al., 2013) has been designed and built by the Department of Physics and Astronomy at the University of Canterbury, New Zealand. The high density observations from a SNOWWEB deployment in the vicinity of Ross and White Islands (see Figure 4.1) provide a unique opportunity to assess Polar WRF output from AMPS at very high resolution.

self-organizing maps (SOMs) are artificial neural networks commonly used to reduce the dimensionality of a dataset (Kohonen, 1990). Training of the neural network is unsupervised, where the network adapts itself to the input dataset with no external indication of 'correct' or 'incorrect' results. While the user may specify the size and shape of the SOM as well as certain training

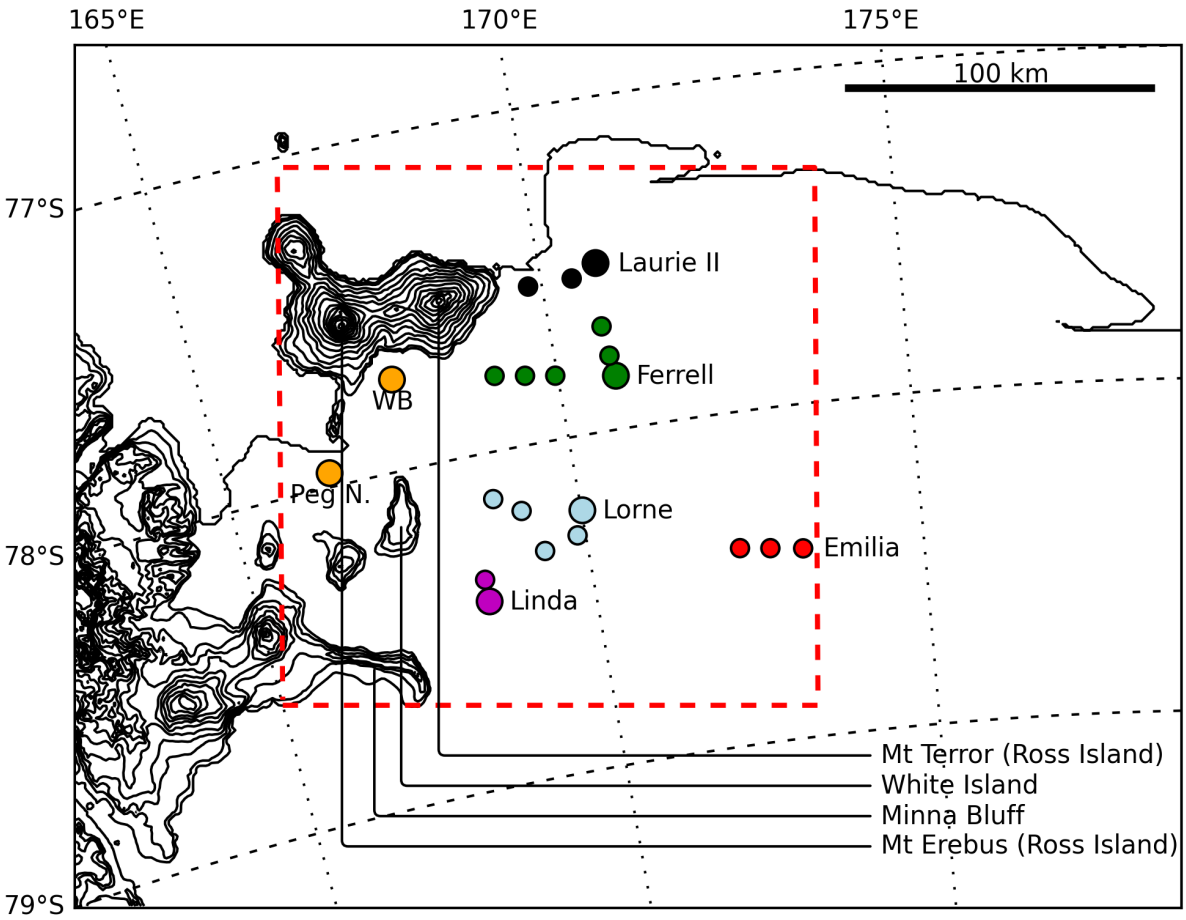

Figure 4.1: Map of deployment area with topographic contours every 250 m. Ross Island (marked by proxy through Mt. Erebus and Mt. Terror) is situated in the top-left segment, with Scott Base and McMurdo Station located at the tip of the peninsula on the south side (near Pegasus North). Small markers denote SWS locations while large, labeled, markers denote existing UWAAWS locations. SWS are color-coded to the nearest UWAAWS for ease of reference, there are no SWS in the vicinity of the orange-colored UWAAWS. The red box shows the area extent covered by subsequent figures.

parameters, the end result is an objective set of distinct patterns that is representative of the entire dataset. This makes SOMs very useful tools for cluster analysis of large, complex datasets, given the simplicity and computational efficiency of the algorithm. While SOMs have been used for a wide array of studies covering many disciplines, they are particularly effective at developing climatologies (Hewitson and Crane, 2002; Reusch et al., 2005; Sheridan and Lee, 2011) and investigating weather patterns and extremes (Seefeldt and Cassano, 2012; Nigro and Cassano, 2014a; Cassano et al., 2015). Clustering methods in general, and SOMs specifically, also have great potential for validating model output. Good examples are demonstrated by Nigro et al. (2011), who used SOM classifications to validate Polar WRF output from AMPS by weather pattern, and Coggins et al. (2014), who used *k*-means clustering to classify ERA-Interim data over a similar area which was

then validated against observations from weather stations. Both highlighted the possibility that large model biases may be overlooked by more traditional methods such as monthly, seasonal, or annual statistics.

The work presented here builds upon the work of Nigro et al. (2011) by applying the SOM algorithm to both model output and SNOWWEB observations then comparing not only the classified data but also statistics from the classifications themselves. In order to compare the SNOWWEB observations with corresponding Polar WRF output from AMPS, 'virtual stations' are generated from the model output by taking the nearest grid points. Surface wind data from both sources are then combined to create a single dataset which is used to train a SOM. This combined SOM is used to classify wind data from SNOWWEB and AMPS separately and compare overall differences in wind and surface pressure by SOM class, as well as differences in SOM class frequency, transience, and temporal alignment to determine how well the highest resolution AMPS output performs at this scale. In addition, the influence of synoptic scale forcing is investigated by using climate regimes presented by Coggins and McDonald (2015) derived from 33 years of ERA-Interim surface wind reanalysis data on a 0.75° x 0.75° grid. Throughout this study, observations from the University of Wisconsin-Madison Antarctic automatic weather station (UWAAWS) network are incorporated to augment and extend the spatial coverage of SNOWWEB, however these observations were not used during the SOM training process.

DATA AND METHODS

Observations

This analysis uses two sources of observational data: SNOWWEB weather station (SWS) (Coggins et al., 2013; Jolly et al., 2013) from the University of Canterbury, and UWAAWS run by the UW Antarctic Meteorological Research Center (AMRC) (Lazzara et al., 2012). SWS are smaller, temporary, weather stations used on a campaign basis to boost the number of observations in an area during the summer months, whereas UWAAWS are larger, permanent, stations that are more widely spread over a far larger area. Twenty SWS stations were deployed at the end of November 2014 and retrieved in the middle of February 2015. The deployment area, approximately 120 km by 130 km, was to the east of Ross and White Islands as indicated in Figure 4.1. The exact time span of this study follows the period when all SWS were deployed and runs from 1st December 2014, to 11th February 2015. The observations used in this analysis come from 15 of the 20 stations mentioned above, the remaining 5 experienced difficulties recording valid wind data throughout the period specified or were not equipped with wind sensors.

SWS commonly observe wind speed and direction, temperature, relative humidity, and pressure, however exact sensor combinations vary with objectives from site to site. Measurements are recorded every minute to an on-board SD card for later quality control and post-processing to produce a 10 minute dataset of mean values. These data are quality controlled by eliminating measurements greater than three standard deviations from the mean using a three hour rolling window. This study focuses on wind and atmospheric pressure observations. While temperature 2 m above ground level was also recorded, there was a substantial positive bias caused by incoming solar radiation during low wind speeds. Filtering data to remove this bias, as per methods suggested by Genthon et al. (2011), removes a large proportion of the total temperature and relative humidity observations and thus reduces the usefulness of these measurements for this study.

UWAAWS record similar observations to SWS but are designed to be permanently deployed with higher-grade, more expensive, instrumentation and control systems. Most stations use satellite communications, or local wireless networks where possible, to upload data. Unfortunately the data collected over the local wireless network (freewave) is not yet integrated into the semi-automatic quality-control process carried out by the AMRC, so freewave data was processed by the authors using the same quality-control techniques as for SWS data. The final UWAAWS dataset used is a combination of the 'q10' 10 minute, manually quality controlled (Lazzara et al., 2012), data product available from the AMRC and freewave data quality-controlled by the authors.

Both (SWS and UWAAWS) 10 minute datasets were further down sampled to match the hourly resolution available from the domain 5 (1.1 km grid) output of AMPS, where the closest possible measurement to the top of each hour was taken.

The Antarctic Mesoscale Prediction System (AMPS)

Using output from the Polar WRF model within AMPS (Powers et al., 2012) as a proxy for observations over a medium to long time period usually requires the researcher to combine output from multiple forecasts into a single, cohesive dataset. Depending on the AMPS domain used, forecasts extend for 40 to 120 hours, where higher resolution (spatial and temporal) domains have shorter forecast lengths (Powers et al., 2012). As forecasts are run twice-daily, the currently accepted method is to define a 12 hour block of forecast hours then concatenate data from all forecasts for those hours only into a single dataset (e.g. Nicolas and Bromwich, 2011; Nigro et al., 2011; Seefeldt and Cassano, 2012; Nigro and Cassano, 2014b). Most studies use forecast hours from the 12 to 23 hour block, with exact hours varying with available model output intervals, to allow time for model spin-up (Guo et al., 2003; Bromwich et al., 2005). A preliminary study re-investigated this method and found that, for domain 5, earlier forecast hours could be used with a small increase in model skill. However the benefit was not substantial and would reduce the relevance of

this study for others in the research community, therefore this study uses the accepted range of hours 12 to 23.

The AMPS physics options for Polar WRF include: the RRTMG longwave radiation scheme, Goddard shortwave radiation scheme, Mellor-Yamada-Janjic (Eta) TKE boundary layer scheme, Monin-Obukhov (Janjic Eta) surface layer scheme, and the WSM 5-class cloud micro-physics scheme. Model top is set at 10 mb with vertical velocity damping applied in the top 7.5 km. Initial model conditions use the National Centers for Environmental Prediction (NCEP) Global Forecast System (GFS) with a horizontal resolution of 0.25° latitude/longitude and a temporal resolution of 6 hours.

Several nested grids ('domains') exist within AMPS. This study uses output from domain 5, a nested 613 km by 718 km grid centered near Minna Bluff south of Ross Island with a 1.1 km horizontal grid length and hourly temporal resolution. Zonal (u) and meridional (v) wind components are available at 10 m, temperature at 2 m, and pressure at the surface. To compare a gridded model output to a network of physical stations, 'virtual' AMPS stations were generated by choosing model grid points that were close to physical station locations. As domain 5 uses a 1.1 km grid length, and the immediate area around each station is flat, interpolation was not required. However, vertical interpolation between 10 m above ground level (AGL) and 2 m AGL was required before the AMPS wind components could be compared to observations. A log wind profile was used with a surface roughness (z_0) parameter of 0.0001 m (Nigro and Cassano, 2014b) and, as the distance was small (10 m to 2 m), the atmosphere was assumed to be neutrally stable and there would be no discernible effect on wind direction. Wind components were also rotated from the model grid to true north using the parameters in the model output files. The time period chosen for the virtual stations matches that for the observations - 1st December 2014 to 11th February 2015.

Self-Organizing Maps (SOMs)

The purpose of SOMs in this study is to cluster time periods with similar wind conditions together into classes (where each class is a node within the SOM) which will be used to classify AMPS output and SWS observations. This allows for the creation of composites for each class as well as the comparison of class statistics between the input datasets. The size and shape of a SOM are important factors to consider before training: too many possible classes will result in low frequencies of occurrence for each class, while too few will result in classes that are 'averages' of what may have been two similar but distinct classes in a larger SOM (Cassano et al., 2015). After some experimentation, a 4 x 3 rectangular SOM was selected as this shape showed sufficient inter-cluster variability while maintaining relatively high frequencies for each cluster which allows

robust analysis. Multiple randomly-initialized SOMs were each trained in two stages: a brief run with aggressive training parameters to roughly shape the SOM, followed by a longer run with more conservative parameters. All returned similar patterns with similar quantization errors so the SOM with the lowest mean error was chosen. A Sammon map (Sammon, 1969) was produced which showed approximately even separation between the SOM nodes with some minor distortion - a good indication that the SOM was well constructed and trained for the purpose of this study (Cassano et al., 2015).

The SOM was trained using a combined dataset of SWS 2 m zonal and meridional wind observations and output for corresponding AMPS virtual stations, with UWAAWS observations reserved for independent validation. The integration of both model and observational data into a single training dataset for a SOM requires caution as the resulting classes will reflect the combined dataset, not the individual components. This is a problem when developing representative climatologies, but that is not the aim of this study as the duration of available observations is insufficient. The primary reason for training with the combined dataset is to produce a set of SOM nodes that can be used to classify either input dataset, with the goal being two classification time series (SWS and AMPS) that may be directly compared. Model bias will be reflected in differences in class frequencies between the time series, where observations will be less likely to receive a classification unduly influenced by model bias. The analysis approach presented is not possible if two separate SOMs (one for each dataset) are used as the classes will be slightly different and thus not exactly comparable. Additionally, a single SOM trained on one dataset would not produce valid classifications of another as the behavior of the SOM classifier on data outside the range (due to model bias/differences) of the training data is undefined.

Approximately two months of data were used for this analysis with just over 1700 hourly timestamps, so the number of periods from the combined SWS and AMPS datasets approaches 3400 timestamps, each with 30 data points (zonal and meridional components from 15 stations). Training the SOM with both SWS and AMPS data produced a common set of classes that could be used to compare the two, allowing the comparison of not only standard meteorological variables and associated correlations but also SOM class frequency, duration, progression, and temporal alignment. The SOMPAK (v 3.1) software implementation of the SOM algorithm was used in this study (obtained from `http://www.cis.hut.fi/research/som_pak/` on 5th March 2015).

RESULTS

SWS and UWAAWS surface winds

After training the SOM using the combined SWS and AMPS dataset of hourly wind vectors, each dataset was classified individually and composites were created from the resulting SOM classes by taking the mean of all data points for each class by station. The objective of this study is to investigate the performance of AMPS (and therefore Polar WRF) and not to develop a new set of surface wind patterns, so the SOM classes themselves will be introduced and discussed briefly to establish confidence they are physically realistic before moving on to the question of validating AMPS forecasts. A subset of statistics for both the SWS and AMPS classifications is presented in Table 4.1, where the network mean wind speed for each class is most relevant to this section. Whenever observations (or model output from corresponding locations) are shown, observations from six UWAAWS are included with those from the SWS network to form a combined set referred to as 'SWS/UWAAWS'. The six UWAAWS - Laurie II, Lorne, Linda, Ferrell, Pegasus North, and Windless Bight - are included on all figures but are not specifically marked after Figure 4.1 in order to increase readability of the already complex diagrams (refer to Figure 4.1 for locations). Correlations with scalar wind speed and both zonal and meridional winds between UWAAWS and SWS neighbors are consistent with equivalent stations within the SWS network alone.

Figure 4.2 shows the mean wind vectors for SWS/UWAAWS observations for each class, with a '(col,row)' identifier (class name) and the class occurrence frequency displayed in each title. There is an obvious gradient in wind speed between class (0,0) at the top-left and class (3,2) at the bottom-right of Figure 4.2, with mean wind speeds increasing toward (3,2). These two classes also have the highest frequencies, together accounting for 38.6% of all time periods. Class (0,0) is the only class to show mean northerly winds, however the fact that it accounts for one-quarter of all periods suggests it simply represents a broad classification of light, northerly, winds. Classes (0,1) and (0,2) represent cases with significant westerly components, however mean vector magnitudes are relatively low. Class (1,0) shows the most significant easterly components but with light overall winds again. All other classes show significant to solely southerly components with a wide range of mean wind speeds. Class (3,2) features the largest mean vector magnitudes and shows structure typical of a RAS event. Wind direction is predominantly southerly and there is a corridor of the highest wind speeds that closely follows the edge of White and Ross Islands, originating from the edge of Minna Bluff and stretching into the Ross Sea. The 'Emilia' group of stations to the east (see Figure 4.1) observe lower winds outside of this corridor. 'Windless Bight' UWAAWS shows extremely low winds from the north (on average) which is typical of the high pressure stagnation zone that typically forms during strong wind events in this area (O'Connor and Bromwich, 1988;

Table 4.1: SOM class occurrence frequencies, mean quantization error, class persistence, and network mean wind speeds for SWS and AMPS datasets. Persistence is the median duration of each class, and mean wind speed is the mean of individual station (or virtual station) means for a given class. Frequency and wind speed differences are negative where AMPS values are smaller SWS. Bold frequency differences are significantly different (95% CI), all other frequency differences are significantly equivalent within +/- 2.5 pp (95% CI). Mean wind speed differences were not tested for significance.

SOM Class	Frequency			Persistence (hrs)		Mean Wind Speed (ms^{-1})		
	SWS	AMPS	Diff.	SWS	AMPS	SWS	AMPS	Diff.
(0,0)	24.77%	20.60%	−4.17	8.0	8.5	2.1	2.2	0.1
(0,1)	5.15%	5.50%	0.35	2.0	2.5	2.1	2.6	0.6
(0,2)	7.87%	7.35%	−0.52	2.0	4.0	3.5	4.0	0.5
(1,0)	11.98%	8.04%	−3.94	3.5	3.0	2.4	3.1	0.7
(1,1)	4.22%	3.65%	−0.58	2.0	2.0	2.9	3.5	0.6
(1,2)	9.26%	5.67%	−3.59	2.0	3.0	4.1	4.2	0.1
(2,0)	5.44%	11.69%	6.25	2.0	3.0	3.8	4.3	0.4
(2,1)	3.47%	3.41%	−0.06	2.0	2.0	4.9	5.0	0.1
(2,2)	7.18%	3.88%	−3.30	3.0	3.0	6.0	6.2	0.1
(3,0)	2.72%	9.32%	6.60	2.0	3.0	5.5	5.5	−0.1
(3,1)	4.11%	7.23%	3.12	3.0	4.0	6.8	6.2	−0.6
(3,2)	13.83%	13.60%	−0.23	8.0	8.0	10.7	10.6	−0.1

Seefeldt et al., 2003). Additionally, the strong alignment of class (3,2) with the 'RAS' regime from the work of Coggins et al. (2014) and Coggins and McDonald (2015) will be shown later, therefore class (3,2) will be referred to as a 'RAS' class throughout the rest of this study. Figure 4.3 is the AMPS equivalent of Figure 4.2 and is discussed in greater detail in Section 4.3.2 (some figures are positioned out of order to aid in comparison).

Figure 4.4 shows directional constancy by SOM class, with Figure 4.5 displaying the difference between AMPS and SWS (discussed in Section 4.3.2). A value of 1.0 indicates a perfectly constant wind direction, while lower values indicate higher variability. Constancy is often related to scalar wind speed, with low constancies indicative of low wind speeds. This effect is seen in the SOM classes, with lower speed classes such as (0,0) displaying lower constancies that increase with wind speed toward class (3,2). 'Windless Bight' (WB) UWAAWS station (named after its location - see

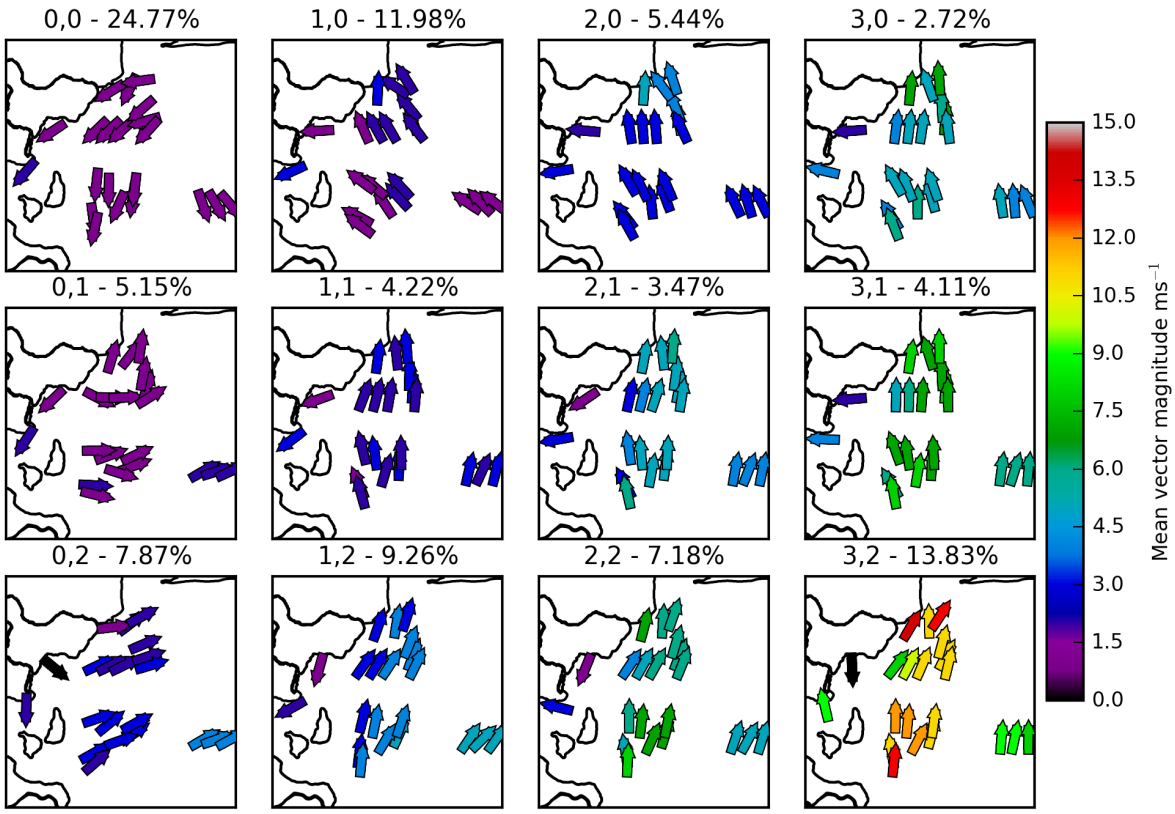

Figure 4.2: Mean 2 m wind vectors for SWS and UWAAWS observations, composited by SOM classification of SWS observations only. The two leftmost stations are Windless Bight and Pegasus North UWAAWS, the remaining four UWAAWS are not marked but may be deduced using Figure 4.1.

Figure 4.1) consistently stands out as an anomaly for most classes, displaying lower wind speeds and lower directional constancy.

Station elevations varied from 18 m to 52 m above mean sea level. To aid in comparison, surface pressure observations were reduced to mean sea-level by calculating a mean scale height every 12 hours using temperature observations from four of the UWAAWS stations: Linda, Lorne, Ferrell, and Pegasus North. These four were selected as they were widely spaced and had good data availability for the entire period. The sea level pressure (SLP) calculated for the easternmost station was then subtracted from the SLP of the other stations to create a relative sea level pressure (RSLP) value for each which is plotted in Figure 4.6. There is a persistent positive westward pressure gradient in this region regardless of class, however class (0,0) - the lowest wind speed class - displays the most homogeneity which implies that, in the absence of a dominant pressure gradient, local forcing for winds is likely dominant and complex. In most other classes, there is a clear gradient from Windless Bight UWAAWS along the Ferrell SWS group. This is particularly pronounced in class (3,2), where Windless Bight shows an extremely high localized RSLP and the gradient is the strongest of all the classes. This is a good example of a high pressure stagnation zone caused by significant orographic blocking (O'Connor and Bromwich, 1988; Seefeldt et al.,

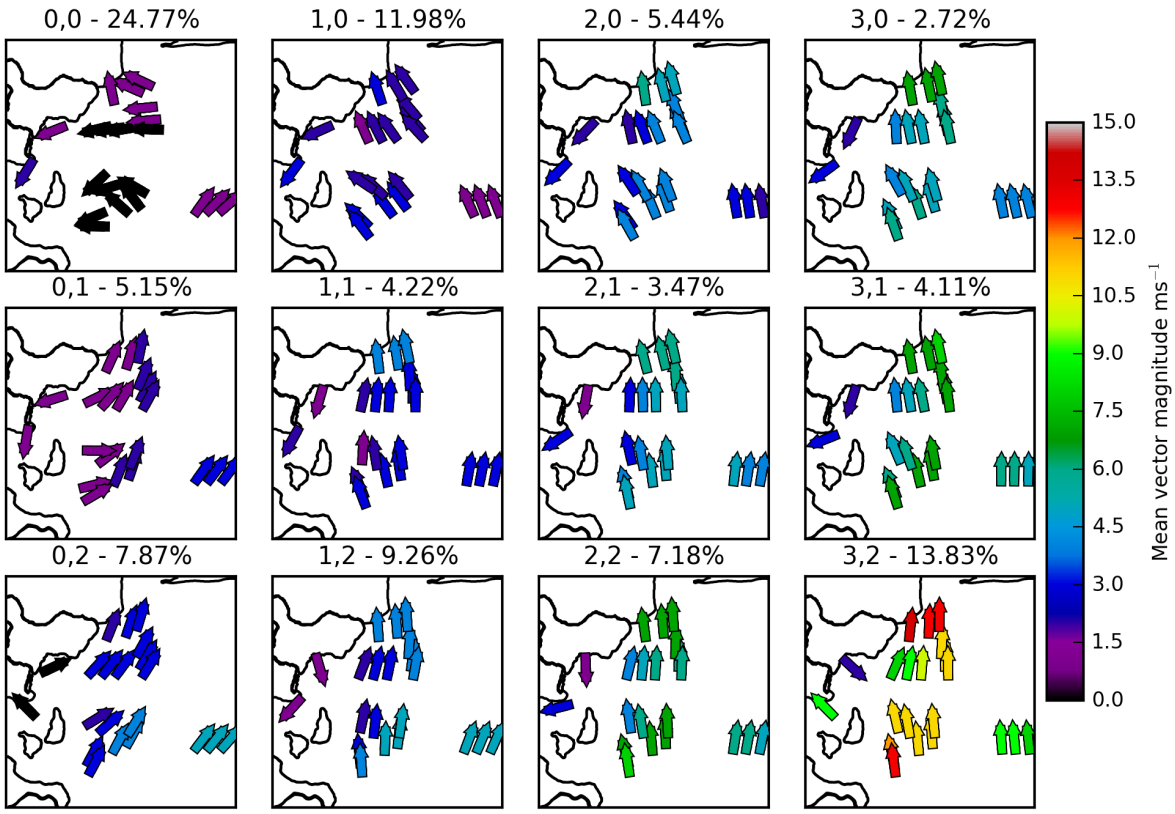

Figure 4.3: As Figure 4.2, but using AMPS output for each station's location in place of actual observations where the nearest model grid point to the physical station location was used. Output is composited using periods identified by SWS SOM classifications.

2003) and supports the low wind speed and directional constancy near Windless Bight in figures 4.2 and 4.4. Differences between AMPS and SWS are shown in Figure 4.7 and discussed in Section 4.3.2.

Comparison with AMPS

Comparing the AMPS vectors in Figure 4.3 to the SWS/UWAAWS in Figure 4.2, where both composites use the SWS SOM classifications, there is general agreement between the two figures. The most notable network-wide differences occur in the left-hand column classes of (0,0), (0,1), and (0,2). Class (0,0) shows what are likely highly variable winds with vector magnitudes approaching 0, while (0,1) and (0,2) show larger southerly components (1.0 ms^{-1} and 1.5 ms^{-1} respectively) and higher mean vector magnitudes (0.7 ms^{-1} and 0.5 ms^{-1} respectively) than seen in the SWS/UWAAWS vectors. There is also a large gradient in the mean vector magnitudes for these classes in AMPS than in SWS/UWAAWS, an effect that is also seen in classes (1,1) and (1,2). For higher wind speed classes in the right-hand half of the SOM, the direction of the AMPS wind

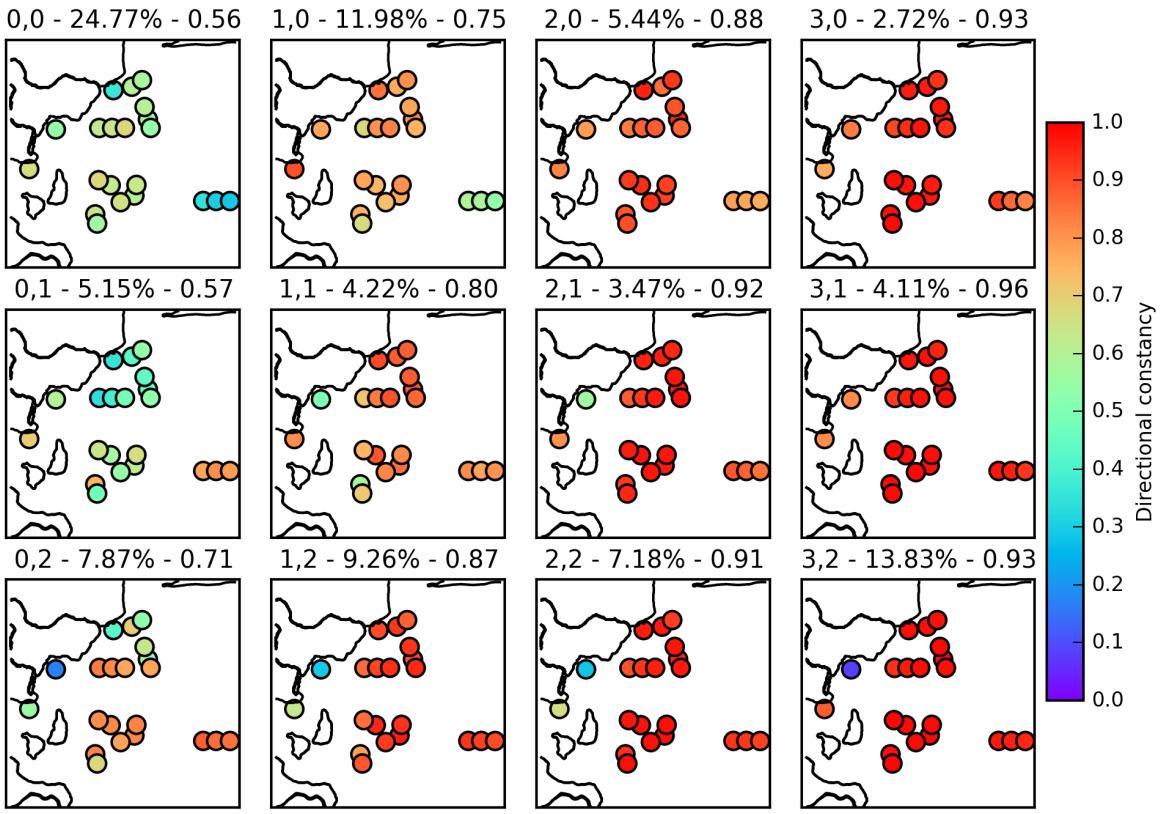

Figure 4.4: Directional constancy of 2 m winds for SWS and UWAAWS observations with composites chosen as per Figure 4.2.

vectors appear more uniform than SWS and are not as visibly affected by surrounding topography. This is particularly pronounced in the final column (classes (3,0/1/2)), where the north-western section of the SWS network shows the influence of Mt. Terror (Ross Island) on the wind field extends further east than is reflected in the AMPS virtual stations.

Differences in directional constancy between AMPS and SWS/UWAAWS observations (Figure 4.5) are inversely proportional to the SWS constancies, where constancy is calculated as the ratio of the mean vector magnitude to the mean scalar speed. There are relatively large differences (both positive and negative) for the classes with lower constancy (see Figure 4.4), decreasing as constancy increases alongside wind speed toward class (3,2). Class (0,0) shows a very large discrepancy, with the AMPS constancy less than half of the bulk of the SWS/UWAAWS network. This suggests Polar WRF within AMPS does not resolve small-scale local forcing well, affecting winds to the east of White and Ross Islands and resulting in highly variable wind directions. The higher constancy of Windless Bight and Pegasus North (see Figure 4.1) are unexpected but likely reflect the fact that WRF is correctly simulating the blocking effect of Hut Point Peninsula and the north-easterly winds that are so common to the area (Coggins et al., 2013) - a hypothesis supported by figures 4.2 and 4.3. The overestimation of constancy for the northern half of the network in class (0,1) can

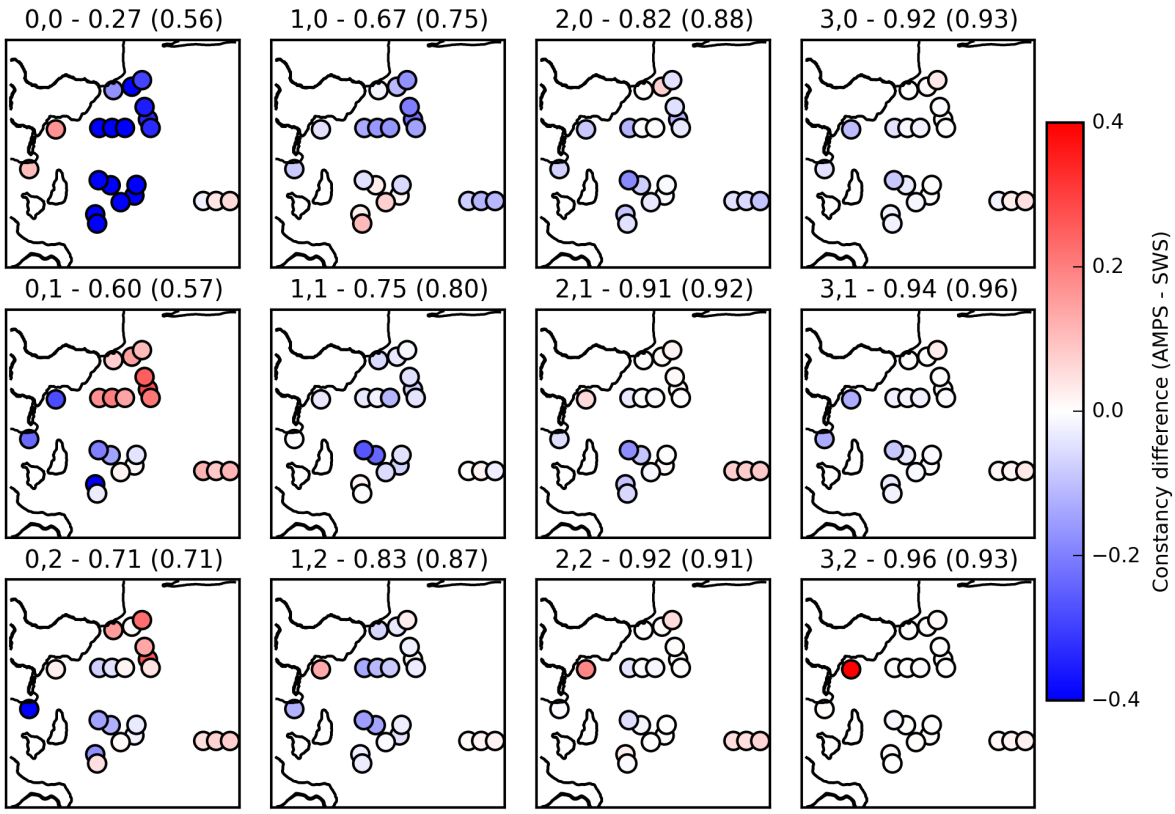

Figure 4.5: Difference in wind directional constancy (of 2 m wind data) between AMPS output and SWS/UWAAWS observations. Positive values indicate overestimation of constancy (therefore underestimate of variability in wind direction) by AMPS. Subplot titles indicate class ID, then the network mean directional constancy for that class for AMPS then SWS/UWAAWS in brackets. NOTE: values for Windless Bight are clipped for classes on bottom row but reach up to 0.5 for class (3,2), as are values for Pegasus North in classes (0,2) and (1,2) which reach as low as −0.44 for (1,2). SWS/UWAAWS observations and AMPS output are both grouped using SWS SOM classifications.

be linked to the higher wind speeds and a larger southerly component, with a similar though less pronounced effect seen in class (0,2).

Differences between the RSLP values in the SWS/UWAAWS observations (Figure 4.6) and those in AMPS are shown in Figure 4.7. For consistency, AMPS SLP was calculated from the surface pressure output using the same methods as SWS/UWAAWS instead of simply using the SLP output that was also available. As this figure shows the difference in RSLP instead of SLP, it is not biased by any offset that may be present between AMPS output and observations. It shows general agreement between AMPS and SWS/UWAAWS RSLP with a tendency for AMPS to very slightly underestimate the RSLP closer to topography for some classes. There are two outliers immediately apparent in the northern-most group of stations - one positive and one negative - yet closer investigation of the SWS/UWAAWS RSLPs in Figure 4.6 does not reveal any obviously

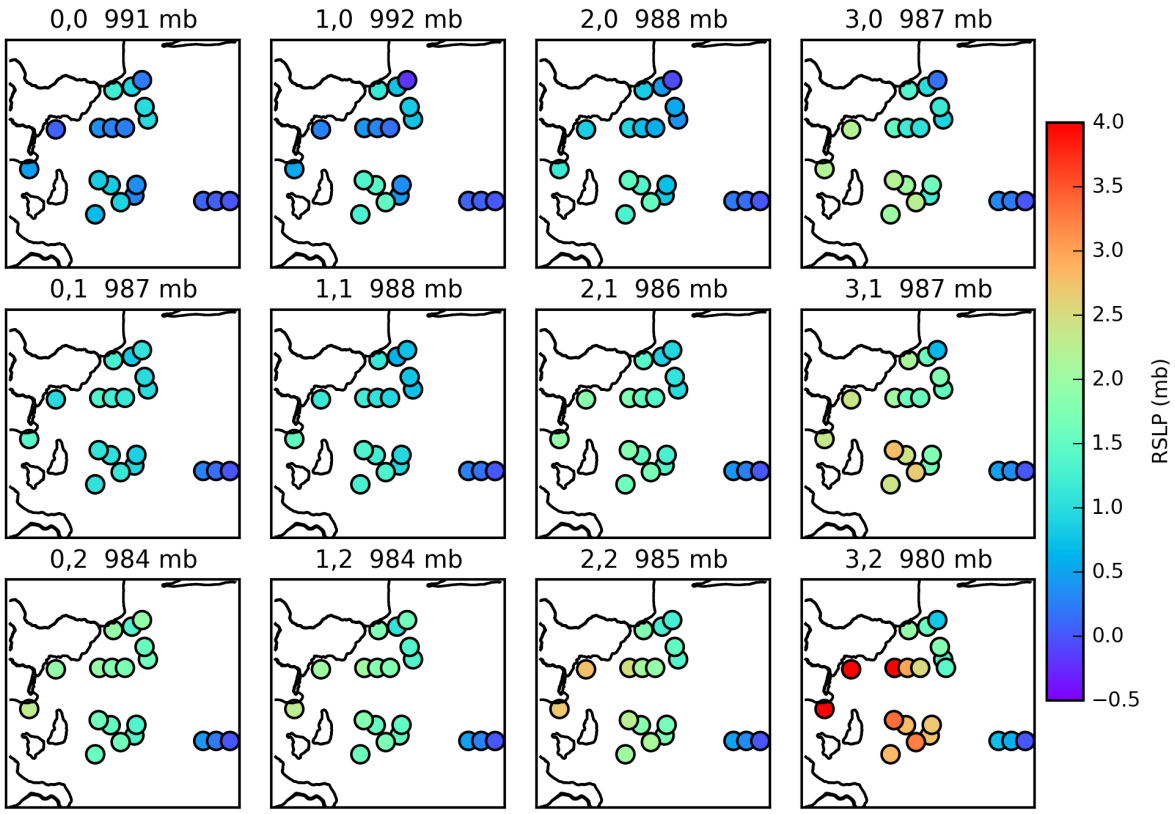

Figure 4.6: Station pressure adjusted to sea-level and relative to the easternmost (rightmost) station for SWS and UWAAWS observations. The sea-level pressure of this station is included in the title of each class subplot for reference.

abnormal RSLP values. Inspection of the AMPS equivalent of Figure 4.6 (not shown for brevity) reveals both locations to be consistent outliers in the AMPS RSLP values, one being lower while the other is higher (matching with the RSLP difference). As both station locations are very close to the edge of the ice shelf, we speculate that there may be a discrepancy between the actual edge and its representation within AMPS at these locations. While the ice shelf edge has recently been updated within AMPS, the stations are so the close that the discrepancy need not be large. The largest differences are in two of the lowest wind speed classes, (0,0) and (1,0), with many stations showing a reduction in RSLP that indicates a weaker or non-existent gradient. The AMPS equivalent of Figure 4.6 (not shown) confirms the gradient in these classes is much smaller or non-existent. This reduction carries through for the Linda/Lorne group into the higher wind speed classes (2,0), (3,0), and (3,1).

Least-squares linear regression was used to determine if any significant linear relationship existed between SWS/UWAAWS wind observations and corresponding AMPS output. Significance was determined using a *t*-test for a 95% confidence interval (CI), where non-significant stations are omitted from all plots. To begin with, correlation coefficients (r-values) for the best fitting linear relationship between SWS/UWAAWS observations and AMPS output were calculated over the

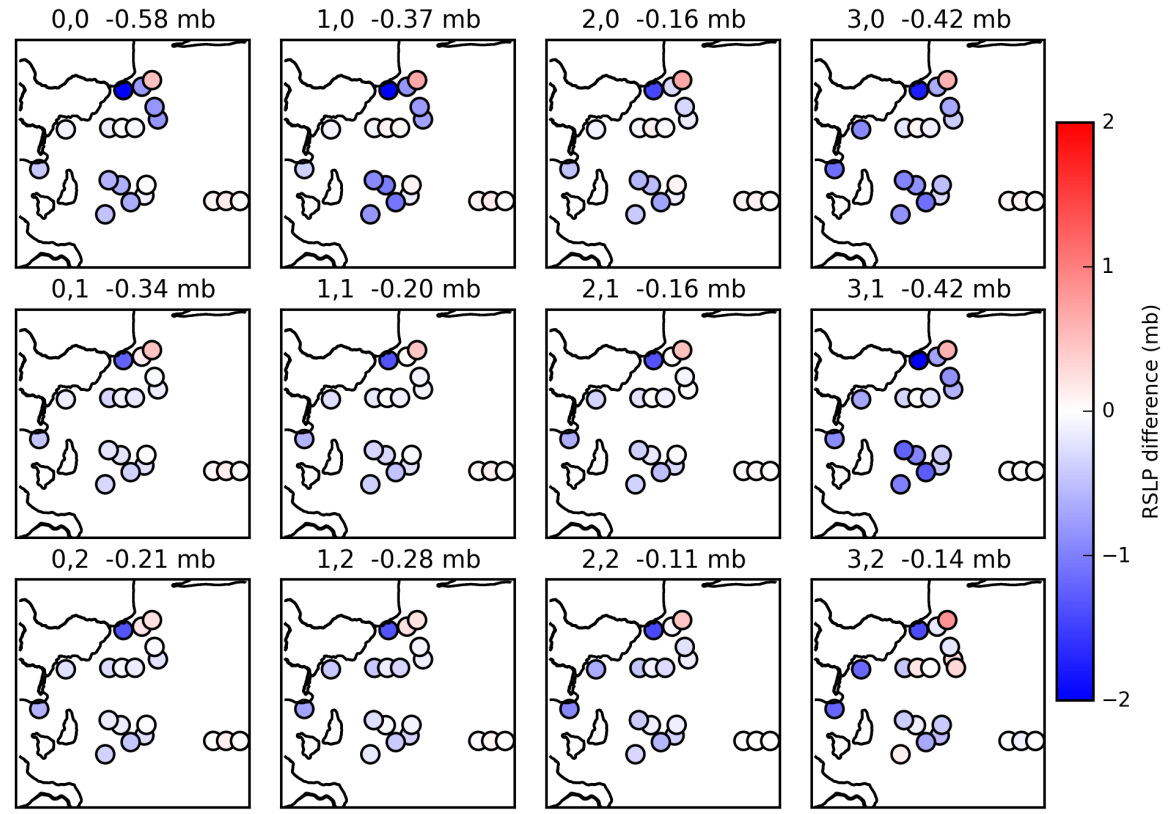

Figure 4.7: Difference in RSLP between SWS/UWAAWS observations and AMPS, where RSLP is the difference in sea-level-adjusted station pressure between each station and the easternmost (rightmost) SWS. The network mean difference in RSLP is included in the title of each class subplot for reference. SWS/UWAAWS observations and AMPS output are both grouped using SWS SOM classifications.

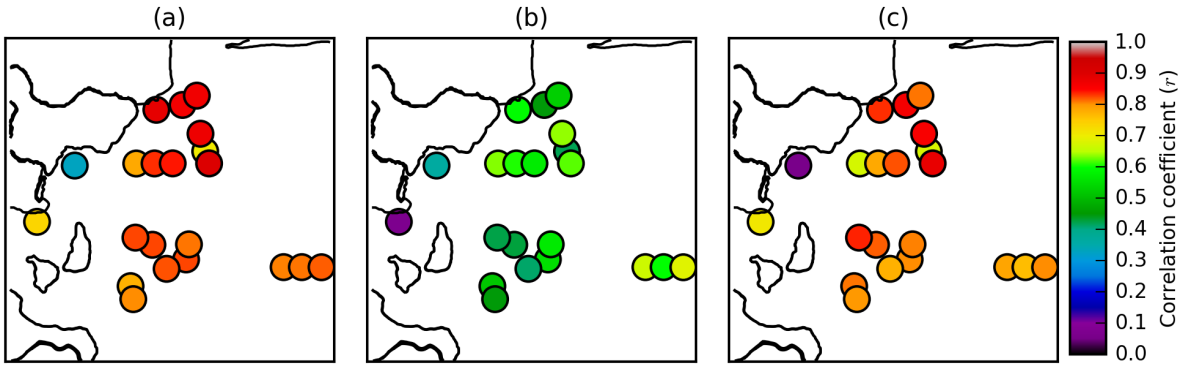

Figure 4.8: Correlation between AMPS output and UWAAWS/SWS observations for 2 m scalar wind speed (a), zonal wind component (b), and meridional wind component (c). All values displayed are statistically significant (95% CI), non-significant values are not plotted.

entire deployment for 2 m scalar (Figure 4.8(a)), zonal (Figure 4.8(b)) and meridional (Figure 4.8(c)) wind components. Speed is highly correlated for this period, while the zonal component is moderately correlated with coefficients between 0.5 and 0.7 for most stations with a distinctive

negative east-west gradient as correlations decrease in proximity to topography. The meridional wind component is more highly correlated than the zonal wind, but also features higher variation between stations. Correlation coefficients decrease along the 'Ferrell' string of stations toward Windless Bight UWAAWS for both scalar wind speed and the meridional component but the effect is not visibly obvious for the zonal wind, perhaps due to the fact that zonal correlations in this area are relatively poor. Windless Bight UWAAWS is the poorest-performing location for all components, an important point which is addressed further in Section 4.4.

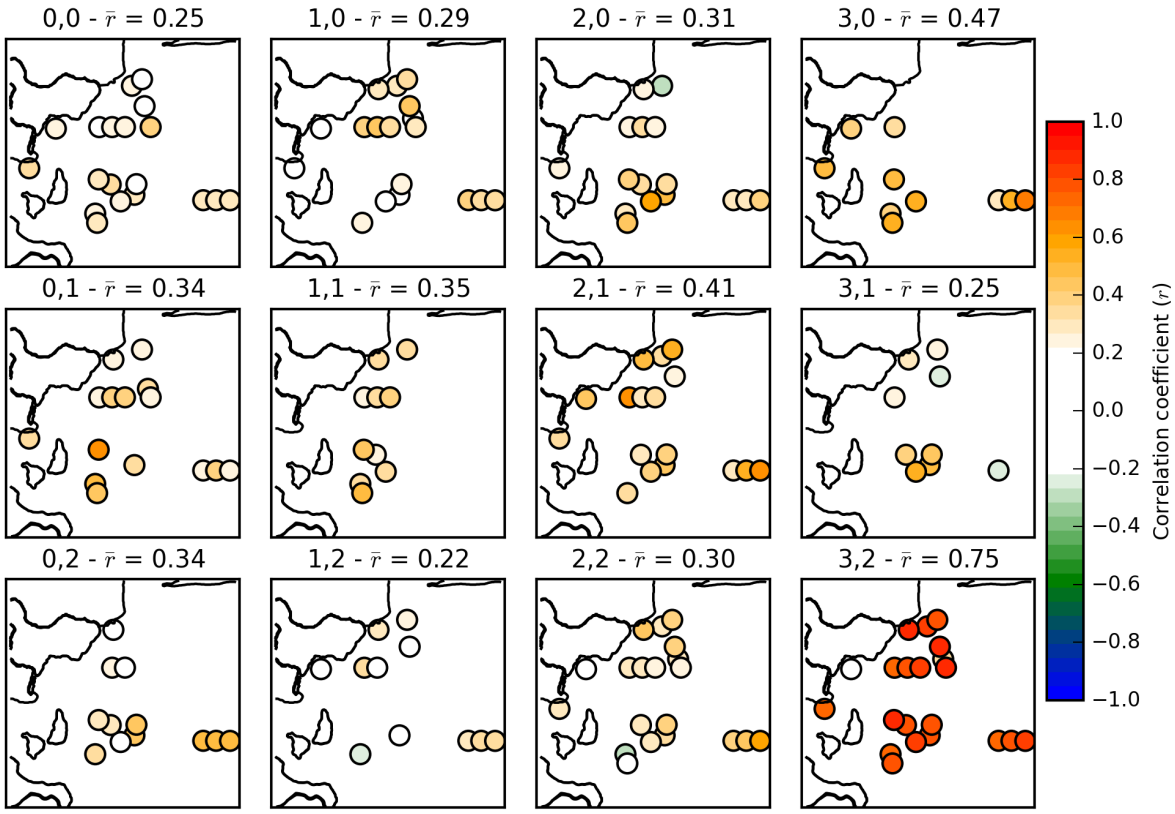

Figure 4.9: Correlation between AMPS output and UWAAWS/SWS observations for 2 m scalar wind speed, organized by class. All values displayed are significant (95% CI), non-significant values are not plotted. Mean correlation coefficient ($\bar{r}$) is displayed in the title for each subplot. Again, SWS classifications were used when selecting data for each class.

Figure 4.9 shows the correlation coefficients for 2 m wind speed between AMPS and SWS/UWAAWS for each SOM class. The un-filled markers denote stations with poor correlation coefficients ($-0.2 < r < 0.2$) that are still statistically significant (95% CI) - non-significant stations are not plotted. There is an obvious gradient present between the low wind speeds and correlations of class (0,0) and the higher wind speeds and correlations of class (3,2). The most consistently well performing locations are the 'Emilia' stations to the east, which also happen to be the furthest from any topographical features.

Scalar wind speed bias is displayed in the final column of Table 4.1 and shows that Polar WRF within AMPS tends to over-estimate wind speeds during lower wind speed classes (as classified by SWS observations). This overestimation is generally low and in the order of 0.1 ms^{-1} averaged over the network, however it can reach as high as 0.7 ms^{-1} (class (1,0)). During the higher wind speed classes of the final column of the SOM, AMPS underestimated wind speeds by a similar amount. In general, the model estimates the network mean wind speed well.

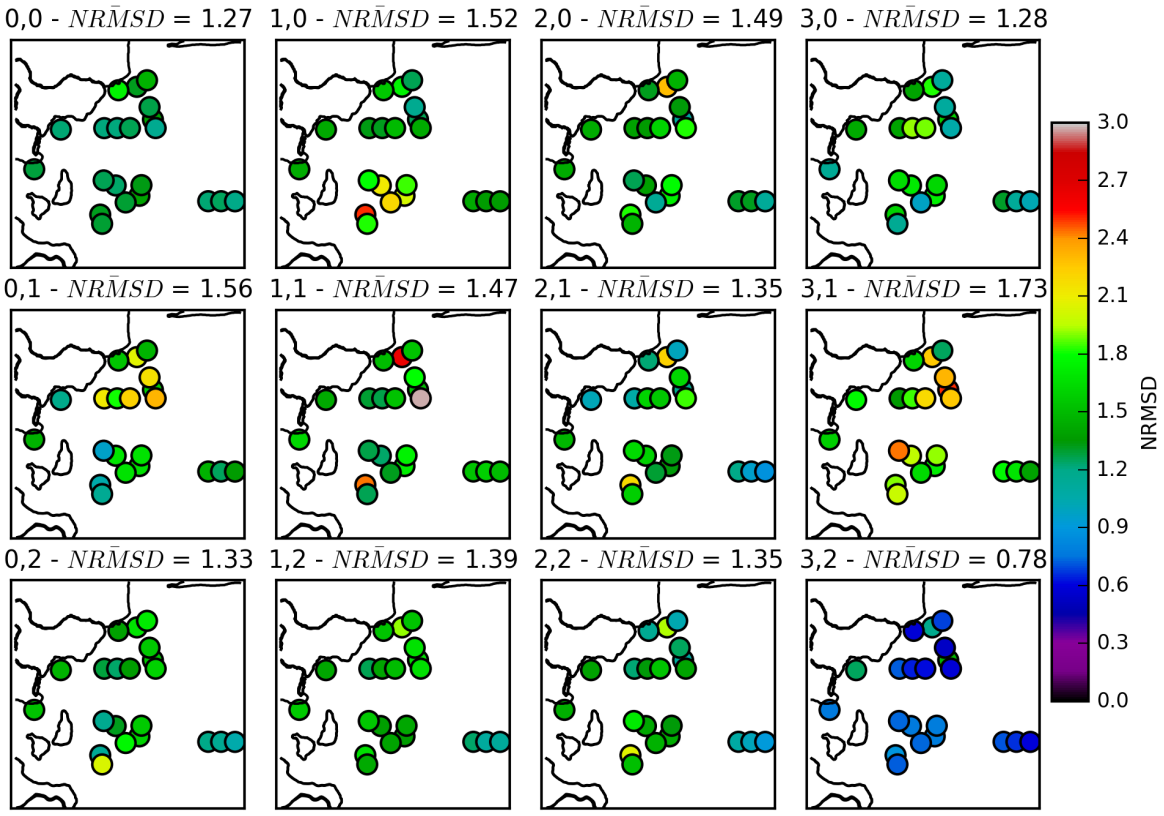

Figure 4.10: NRMSD between SWS/UWAAWS 2 m wind speed observations and AMPS output, where both datasets are composited using SWS classifications. The RMSD is calculated by class and station, then normalized by the standard deviation of the corresponding SWS or UWAAWS observations. Values greater than 1 (green/orange/red/gray on the color scale) indicate that differences between the model and observations were greater than the variability within the observations (lower values are better). Network mean NRMSD for each class is displayed in the subplot titles.

The bias information is important context for Figure 4.10, which displays the NRMSD between SWS/UWAAWS observations and AMPS output. The NRMSD is simply the RMS difference between SWS/UWAAWS observations and corresponding AMPS output, normalized by the standard deviation of the observations for each station (Bromwich et al., 2005). Low values (NRMSD < 1) indicate the difference between the AMPS output and the observations is less than the variability within the observations alone. Figure 4.10 shows a similar gradient across the SOM to that of Figure 4.9, except for class (0,0) which features the second lowest mean NRMSD - lower than

all surrounding classes. Class (0,0) also has a very homogeneous spatial distribution of NRMSD values relative to the other SOM classes.

SOM statistics

The primary advantage of training a single SOM on the combined dataset is to allow the direct class-by-class comparison of SOM statistics between SWS and AMPS. Table 4.1 shows the frequencies (proportion of time during the entire study that a given class occurred) and persistence (median duration of class in hours) for each class for both SWS and AMPS classification sets. Differences in class frequency are also shown, where a negative difference indicates the AMPS frequency was lower than the SWS. Differences that are not in boldface are significantly equivalent within +/- 2.5 percentage points, while those that are in boldface are significantly different. Both significance tests used variants of the z-test with a 95% CI. Most of the differences are observed in the top row of the SOM, with AMPS output featuring a lower rate of occurrence of the lower wind speed classes (0,0) and (1,0) than SWS, and a higher rate of occurrence of the higher wind speed cases of (2,0) and (3,0). Other classes with substantial differences are (1,2) and (2,2) (under) and (3,1) (over), where it appears as though (3,1) is over-predicted at the expense of (2,2) - this is addressed later when discussing class alignment.

Persistence (or class duration) is calculated from contiguous blocks of timestamps with identical classifications, for example 5 consecutive (3,2) classifications are interpreted as a single 5 hour event. The distributions of persistence are non-normal with uneven tails for most classes with occasional large outliers, therefore class median values were calculated. Both SWS and AMPS show a median persistence of approximately 8 hours for the most prevalent classes (0,0) and (3,2) with good agreement between the model and observations in this respect. While persistence values are largely similar for the majority of the other classes, with only one featuring a difference of more than one hour, the AMPS classes do tend to persist for longer than the SWS classes.

Investigating how well SWS and AMPS classifications align in time provides much more information on the performance of AMPS than class frequencies alone. Figure 4.11 shows the probability ($0 < P < 1$) of AMPS receiving the same classification as SWS by SOM class (values highlighted by green boxes). The other boxes show the probability, by class, that AMPS output will receive a different classification. For example, if a given snapshot of SWS observations receives a classification of (0,0), the probability of AMPS output for the same time slice also receiving the same classification is 0.6 (or 60%). Additionally, for the remaining 40% of occurrences, there is a roughly equal chance (approximately 10%) of receiving a classification of (0,1), (0,2), (1,0), or (1,2). Figure 4.11 shows very poor alignment (less than 10% of the time) between AMPS and SWS for classes (1,1) and (2,1), yet the frequencies for these classes are equivalent (significant at 95% CI) between

the datasets. This indicates that, while Polar WRF and AMPS may do a good job overall, there are substantial issues around timing.

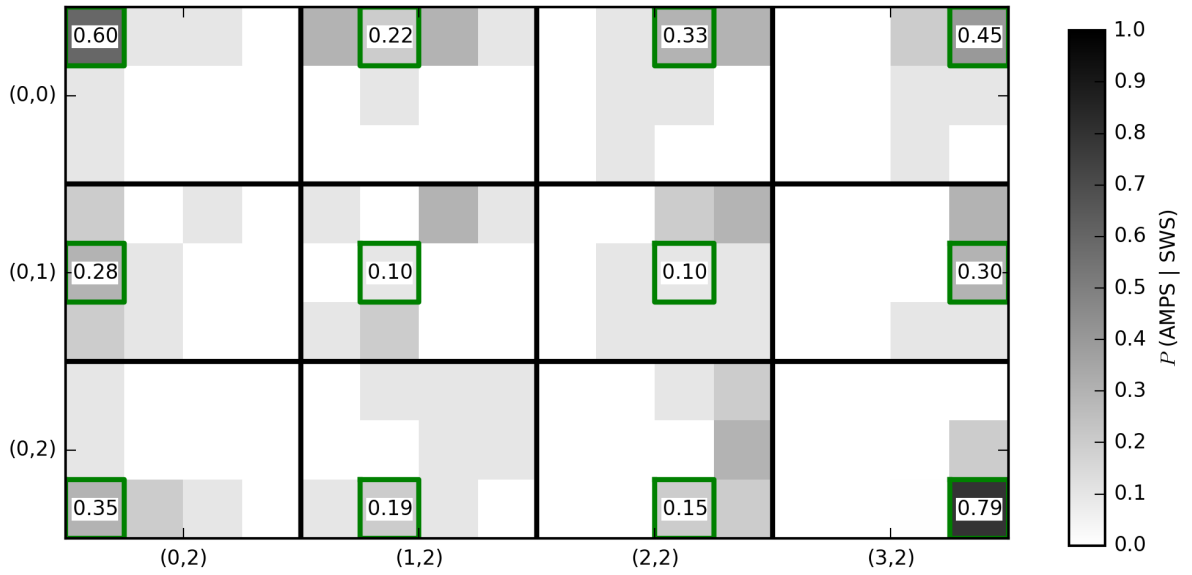

Figure 4.11: Probability ($0 < P < 1$) of AMPS receiving a classification for each SWS classification, shown as a 4 x 3 grid (bold outlines) of nested 4 x 3 grids (shaded squares). Grid cells containing values (surrounded by green boxes) show the P of AMPS receiving the same classification as SWS, while the other cells of the 4 x 3 sub-grid show the P of AMPS receiving each other classification, where shading is indicative of the value. For example, in class (0,0), AMPS will receive the same classification as SWS with a P of 0.60 (60%), with the remaining 0.4 (40%) evenly split between classes (0,1), (0,2), (1,1), and (1,2). To ease interpretation, cell values were rounded to one decimal place before shading.

Equally important is the very good alignment shown for class (3,2) within AMPS, with a probability of alignment with SWS classifications of 0.79. Additionally, the only other classification that AMPS received during SWS class (3,2) during this study was class (3,1), which is a lower wind speed variant of (3,2) with some minor associated differences in direction. Class (0,0) is also well-represented in AMPS despite the fact it occurs at a lower rate than with SWS observations. While the alternative classifications for this class in AMPS (shown in Figure 4.11) all feature very different mean vector patterns (Figure 4.3), it is worth remembering that the directional constancies of these patterns are among the lowest of the SOM classes, which means conditions for some of these instances may overlap to a greater extent than displayed. Most other classes are poorly represented with respect to rate of occurrence (significant differences in Table 4.1) or alignment (low P values in Figure 4.11) or both.

Figure 4.11 also provides insight into the differences in frequencies displayed in Table 4.1 for classes (2,2) and (3,1), where the differences in frequencies are -3.30 and +3.12 percentage points respectively. The preferred AMPS classification for SWS instances of (2,2) is (3,1), as shown by

the dark cell shading, yet this is not reciprocated. Combined with the fact that class (3,1) is over-predicted by a similar amount that (2,2) is under-predicted, thus the majority of this difference is caused by AMPS output forecasting class (3,1) conditions at the expense of class (2,2). The main difference between these classes is the wind flow pattern (see Figure 4.2), where class (3,1) displays a tendency for the predominantly southerly winds to curve to the west around the tip of White Island, resulting in easterly winds at Windless Bight and Pegasus North. Class (2,2) shows the southerly being deflected in the opposite direction, toward the east, with very light winds at Windless Bight and a stronger southerly component at Pegasus North. Both these UWAAWS locations show higher variability in direction in class (2,2) (Figure 4.4) along with increased RSLP (Figure 4.6) in the observations.

In the same way that results shown in Table 4.1 need to be considered in the context of Figure 4.11, the opposite is also true. While class (3,0) has a relatively acceptable alignment between AMPS and SWS at 45%, AMPS receives that classification at 3.4x of the rate of SWS. This effectively means that AMPS is forecasting those conditions so often that the good alignment is not necessarily a reflection of model skill; classes (2,0) and (3,1) also show similar tendencies. While the reverse may be said of (0,0), (1,0), (1,2), and (2,2), the alignment probabilities of all bar (0,0) are low enough that the effect would likely be minimal.

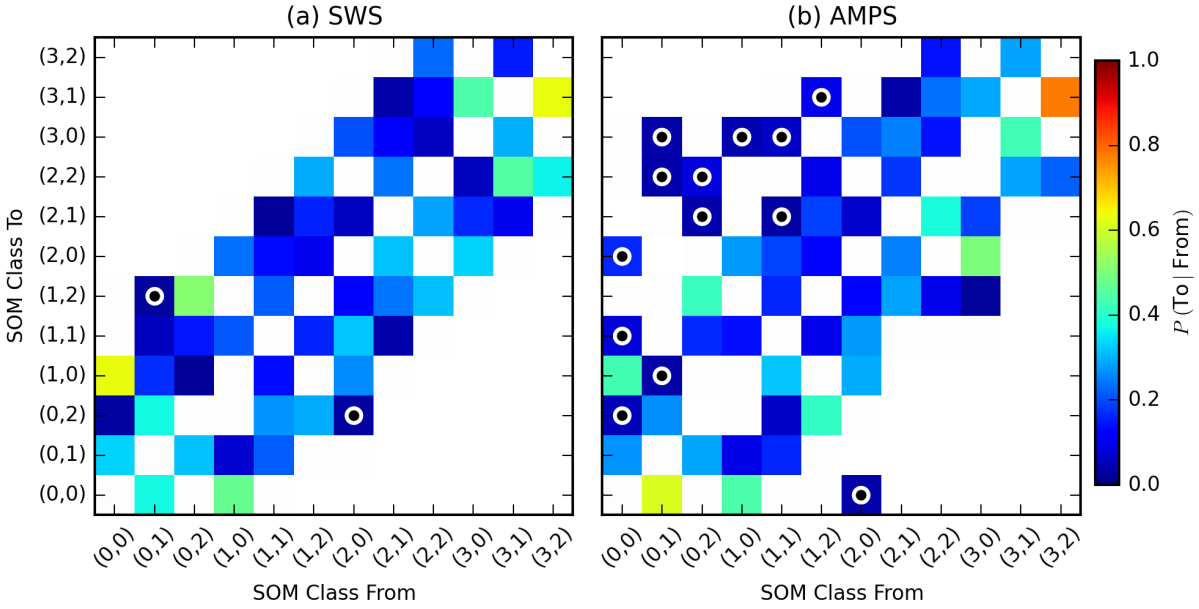

Figure 4.12: SOM class progression for SWS (a) and AMPS (b) classifications, where the origin class is on the x-axis. Black and white markers indicate transitions that predominantly (> 75%) occurred at the hours of 0000 or 1200 UTC, where different 12 hour AMPS forecast blocks join.

SOM class progression for both SWS (a) and AMPS (b) is shown in Figure 4.12, where the probability that an instance of a given SOM classification (x-axis) will progress to another classification (y-axis) that is not itself (class is not persisting) is indicated by the color. For example, Figure

4.12(a) shows that class (0,0) tends to progress toward class (1,0) most frequently (approximately 60%), followed by (0,1) (approximately 30%), then (0,2). The overall pattern (roughly symmetrical about the diagonal) in this figure shows that, for SWS observations, classes tend to progress towards adjacent neighbors. This behavior is expected as the SOM algorithm groups similar classes together in SOM-space, so a large number of transitions that were not to an adjacent neighbor would indicate a very unstable or non-linear underlying system, or a poorly-designed SOM.

Figure 4.12(b) shows class progression through AMPS output. Immediately visible is the tendency for AMPS classes to occasionally jump adjacent neighbors and progress to very different classes. Upon further investigation, it was found that most of these jumps coincide with boundaries between the different blocks of forecast hours used to construct the AMPS dataset, where blocks change at 0000 and 1200 hours UTC every day. Class progressions that occur predominantly (at least 75%) during these hours are indicated by black-and-white markers in Figure 4.12, where all obviously abnormal transitions in (b) fall into this category. The markers in Figure 4.12(a) (SWS) are provided for context only and show that transitions during this time occur randomly and are not common. There is evidently a deviation from the observations as the forecast progresses, which results in a step-change as the output from the subsequent forecast - 12 hours younger with a new set of initialization inputs - is introduced into the dataset. It can be seen that AMPS has a higher tendency to deviate from the observations under lower wind conditions as none of the highest wind speed classes are affected.

Synoptic scale context

While this study focuses on the mesoscale, it is important to also understand larger scale processes that are forcing the conditions seen in the target area and their potential contribution to differences between SWS and AMPS. The synoptic climatology developed by Coggins et al. (2014), using *k*-means clustering to classify 33 years of 10 m wind output from the ERA-Interim reanalysis, is a useful tool for providing wider-scale context for the SOM presented here. Of particular interest are the broader 'regimes' as outlined by Coggins and McDonald (2015) and shown in Figure 2 of their study which are referred to hereafter as 'Coggins regimes'. Five regimes were identified in total: weak northern cyclonic (WNC), strong northern cyclonic (SNC), RAS, weak southern cyclonic (WSC), weak synoptic (WS). The WNC and SNC regimes feature a cyclone in the Ross Sea to the north of the RIS with varied degrees of intensity, alongside light to moderate winds over the RIS. The WSC regime features a cyclone over the RIS itself with light winds, while WS has a very small pressure gradient over the RIS with widespread calm conditions. The RAS regime features a strong pressure gradient over the RIS with strong southerly winds transporting air from the Siple Coast and interior of Antarctica out into the Ross Sea, often past the edge of Ross

Island. Updated classifications of 6-hourly ERA-Interim reanalysis output for the relevant time period were created to directly compare with the SOM from this study. SOM classifications were down-sampled to match the 6-hourly resolution of the ERA-Interim output.

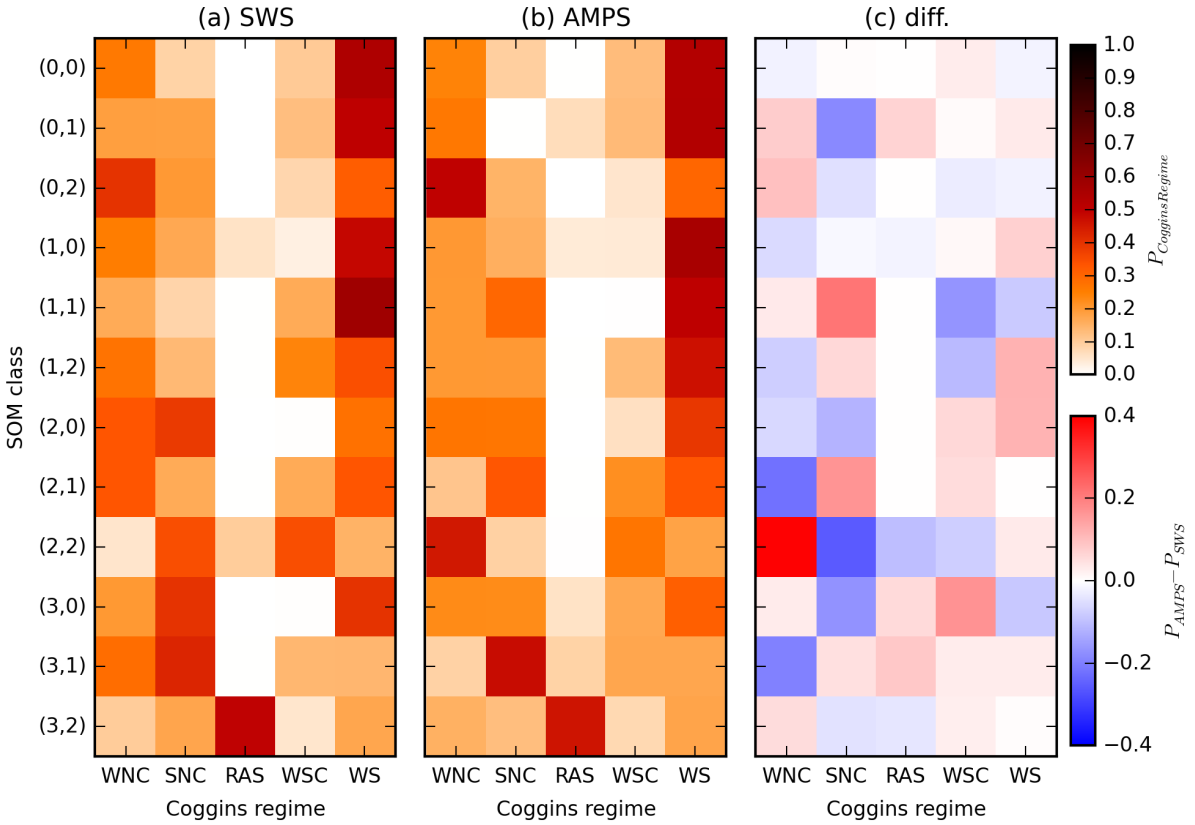

Figure 4.13: Alignment of Coggins regimes for each SOM type as classified by SWS observations (a) and AMPS output (b), with the difference (c).

Figure 4.13(a) shows $P(\text{Coggins}|\text{SOM}_{SWS})$, the probability of finding each Coggins regime for each SOM classification of SWS observational data. Because two different classification schemes on very different spatial and temporal scales are being compared, and the ERA-Interim dataset is not perfect, SOM classes will not always align with their ideal Coggins regime counterparts. However there is good agreement between the two, with synoptic regimes likely to have a weaker forcing effect on the SOM target area (WNC, WS, WSC) being more prevalent in the upper half of the SOM, corresponding to the first two columns of the SOM space in other figures, where weaker and more variable winds are observed. Conversely, SNC has a higher prevalence in the lower half where winds are higher and more directionally constant. The RAS regime is dominant for SOM class (3,2) which has already been identified. In rare cases, the RAS regime is also present in (1,0) or (2,2), which is likely caused by the exact location of the airstream shifting away from Ross Island toward the middle of the RIS with the SWS/UWAAWS network observing reduced wind speeds. If alignment is investigated in reverse by calculating SOM class occurrence for each

Coggins regime (not shown for brevity), SWS class (3,2) is present for 83% of all Coggins 'RAS' regime occurrences.

Figure 4.13(b) shows the alignment of Coggins regimes with the AMPS SOM classifications, with Figure 4.13(c) displaying the differences between the AMPS and SWS classifications. A recurring theme is the switching of prevalence of the WNC and SNC regimes between SWS and AMPS SOM classifications, the most notable classes being (2,1) and (2,2). These two AMPS classes also have poor alignment with SWS (as shown in Figure 4.11), so the fact they relate to different synoptic situations suggests the large-scale forcing is important for the differences in these classes. While AMPS has slightly more spread during the RAS regime than SWS, it is promising that it still aligns well with class (3,2). Additionally, there is very little difference between the regimes present for SWS and AMPS during classes (0,0), (0,2), and (1,0) which, when combined with (3,2), account for almost 60% of the study period (by SWS classifications). As with SWS classes in Figure 4.13(a), if the reverse of Figure 4.13 (b) is calculated then SWS class (3,2) is predominantly present (in this case 75% of the total) during Coggins 'RAS' regime occurrences.

DISCUSSION

The use of SOMs for analyzing Antarctic atmospheric data over the RIS, in particular output from the AMPS forecast system, is not a new idea (e.g. Seefeldt and Cassano, 2008; Nigro et al., 2011, 2012a,b; Seefeldt and Cassano, 2012; Nigro and Cassano, 2014a,b). However, previous studies have operated at far larger spatial and temporal scales, predominantly seeking to develop climatologies or insights into physical processes at the synoptic scale. Only a single summer season of observations from the SWS network are available for the target location of this study, so attempting to define a climatology is unrealistic. However, this does not preclude the use of a SOM for model validation and the classes produced (Figure 4.2) appear to represent a wide variety of wind patterns that may be expected over the summer months in the target area. Large periods of calm or light winds are often encountered during this time, with occasional southerly storms of varying intensity and duration (Savage and Stearns, 1985; O'Connor and Bromwich, 1988; Seefeldt et al., 2003). This is reflected in the frequency and persistence information presented in Table 4.1, with calm or light wind conditions accounting for around 50% of the study period, gentle to moderate winds for 32%, and strong winds for almost 14% (class (3,2)). Additionally, classes (0,0) and (3,2) were both very persistent with median durations of 8 hours each. The intra-class spatial patterns observed in Figures 4.2, 4.4, and 4.6 are coherent between variables, with lighter and more variable winds closer to orographic features and the high pressure stagnation zone observable in Windless Bight.

Class (0,0) of the SOM in this study is the most prevalent, with a class frequency of almost 25% in the observations, and represents light winds with a mean northerly, yet highly variable, direction. This is likely the result of a bias in granularity in the SOM algorithm toward higher wind speeds which have a greater effect on the Euclidean distance metric (root mean squared difference between training data and SOM class weights) used. The SOM was repeated as a separate study using normalized wind components, effectively removing any bias due to vector magnitude. The patterns produced were similar to those presented in this study, though greater granularity was observed at lower wind speeds. While this behavior is desirable, wind speed information is still vital for fair comparisons with AMPS so the study was not pursued further. An improvement to the current study would be to create a second SOM using data from class (0,0), and possibly the surrounding low wind speed classes, to gain further clarity about what happens under lower wind speed conditions. Whether or not this would improve the correlations, bias, NRMSD, and alignment between AMPS and the observations is unknown as it is likely that some detrimental attributes are being masked by the high variability and large number of occurrences.

Class (3,2) is the next most prevalent and is representative of those periods with the largest mean wind vectors (Figure 4.2), highest constancy (Figure 4.4) and largest pressure gradient (Figure 4.6). Coggins regimes (Coggins et al., 2014; Coggins and McDonald, 2015) add context with wider synoptic conditions and show that (3,2) is associated with the RAS regime 50% of the time, with RAS or the strong synoptic forcing of SNC present for almost 70% for all instances of (3,2). AMPS represents conditions during class (3,2) very well, with the highest correlations (Figure 4.9), smallest NRMSD (Figure 4.10), smallest differences (Figure 4.5 and Figure 4.7), best class alignment (Figure 4.11), and good agreement for class frequency and persistence (Table 4.1), and transitions (Figure 4.12). The exception is the magnitude of the pressure gradient from Windless Bight toward the RIS and the corresponding low correlations, large difference in constancy, and obvious difference in mean vectors for Windless Bight UWAAWS. Thus, while Polar WRF within AMPS does well at representing RAS conditions in general, it appears to underestimate the magnitude of the orographic blocking provided by Mt. Erebus and Mt. Terror on Ross Island. This blocking manifests as the Windless Bight high pressure stagnation zone which has a large impact on wind flow in the area (O'Connor and Bromwich, 1988; Seefeldt et al., 2003). The effect of this underestimation is visible in the wind vectors of Figure 4.3 relative to the SWS/UWAAWS observations in Figure 4.2, where the AMPS vectors are more uniform with reduced components for all high wind speed classes. The cause of the underestimation is likely influenced by terrain smoothing due to the relative (to the terrain features) coarseness of the model grid; Mt Erebus and Mt Terror are approximately 250 m too short and the high points of Hut Point Peninsula are 100 m too short with more gentle slopes in the model than reality.

In this study, the Polar WRF model in AMPS clearly performed poorly under the low wind conditions of class (0,0). While the frequency and alignment of this class (Table 4.1 and Figure 4.11), along with the Coggins regimes present (Figure 4.13), compared relatively well with observations, the actual conditions forecast did not correlate well (Figure 4.9) and contained some large differences (Figures 4.3 and 4.5). The observed pressure gradient for class (0,0) is smaller than all other classes (Figure 4.6) and there is a high prevalence of Weak Synoptic or Weak Northern Cyclonic regimes (Figure 4.13) developed by Coggins and McDonald (2015). This shows the synoptic scale sources of forcing are weak for this class, which is expected in conjunction with the lower wind speeds. Other classes surrounding (0,0) also feature small pressure gradients, high probability of the Weak Synoptic Coggins regime, low wind speeds, and poor correlation, high NRMSD, and larger biases in directional constancy. While Polar WRF within AMPS may predict the occurrence of low wind conditions well (class alignment in Figure 4.11), the actual wind conditions forecast do not often match the observations (intra-class correlation in Figure 4.9 and comparison of vectors in Figure 4.2 and Figure 4.3). In a practical sense, this may not have a large impact on the logistical (predominantly flight) operational planning that utilizes AMPS forecasts, however wind flow patterns at low wind speeds will impact the formation and trajectory of fog in the region which often interferes with human activity and impacts on the radiation balance.

During periods of reduced synoptic scale pressure gradients, such as those highlighted above, mesoscale atmospheric dynamics play a larger role in dictating the surface wind field. Two important factors that need to be well resolved are incoming and outgoing radiation and their interaction with the local terrain (Pielke Sr, 2013), which influence mesoscale pressure gradients and thereby wind fields. The correct simulation of cloud, particularly cloud micro-physics, is extremely important in this context - a difficult task especially at such a small scale (Bromwich et al., 2013). Mixed-phase and supercooled clouds are common (Lawson and Gettelman, 2014; Scott and Lubin, 2014) and the ratio of liquid water to ice within clouds will affect the incoming and outgoing radiation balance (Wilson et al., 2012). To assist, appropriately fine model grids are required which in turn require high resolution datasets (including sea and land ice cover) for initial parameterization. Data sources used for initialization are also likely insufficient given the complex, small scale, topography near Ross Island. The GFS output assimilated by AMPS provides 0.25° horizontal resolution which equates to 27.9 km x 5.8 km (latitude/longitude respectively) over Ross Island. This is insufficient for GFS to resolve the complex topography of the region and therefore its interaction with the atmosphere, which will result in differences between the GFS output and reality. It is worth noting that a previous study by Bromwich et al. (2013) identified that Polar WRF is very sensitive to initial conditions.

Using the Coggins regimes as a method to gain synoptic scale perspective for a mesoscale SOM works very well and helps to highlight classes where AMPS does not characterize available obser-

vations. Some classes with high disagreement between AMPS and SWS also tend to show very different regimes, with AMPS tending to be more spread between the five possible options. Class (3,0) is a good example, where the synoptic forcing appears to be either a low pressure system to the north (SNC/WNC), or weak overall pressure gradients (WS) in the observations, yet an almost even spread for AMPS. Class (2,2) shows poor correlation, alignment, and frequency difference features a swap in the dominant regime from SNC (SWS) to WNC (AMPS), and a reduction in the probability of seeing RAS and WSC regimes for AMPS. This switching between SNC and WNC between AMPS and SWS is also very visible in class (2,1), and less obvious but still present in many other classes, which suggests that AMPS may not be reflecting the magnitude or position of low pressure systems seen over the Ross Sea in ERA-Interim output. This is consistent with previous work by Nigro et al. (2012a), who found problems with the representation of cyclones within AMPS over the Ross Sea.

The discontinuities within the dataset of concatenated AMPS forecast blocks highlighted in Figure 4.12(b) could prove to be an interesting measure in the future for the analyses of larger datasets. Unfortunately, the period of available observations for this study was not large enough to allow further study of the discontinuities with a high level of confidence, however future studies employing SOMs to analyze concatenated output from multiple model runs over longer periods of time could use the SOM class progression as a proxy to identiAlignment of Coggins regimes for each SOM typefy radical discontinuities in their dataset.

CONCLUSIONS

This study used wind observations during the 2014-15 austral summer from 15 SWS (weather stations). Combined with output from corresponding nearby AMPS grid points ('virtual stations'), the resulting dataset was used to train a single SOM which in turn classified the original data sets individually. This allowed a comparison of both the datasets and their corresponding SOM statistics in order to gain further insight into the quality of simulations over part of AMPS domain 5, a nested grid with a spacing of 1.1 km not previously studied in detail. Both wind and pressure SWS and UWAAWS observations were compared with output from nearby AMPS grid points for each SOM class. Within AMPS, Polar WRF did not accurately model surface-level winds during light wind conditions when synoptic-scale forcing was weak, however it was able to forecast the low wind periods themselves well and there was good alignment with synoptic-scale regimes identified. This suggests that Polar WRF within AMPS may struggle to resolve localized (meso-scale) forcing during periods of low winds and weak synoptic forcing. Insufficient resolution of available model initialization data, along with model grid length are possible contributors, given the complex nature of the topography in this region.

Surface wind correlation generally increased with wind speed, however problems arose around the timing of certain SOM classes (wind patterns) for classes with lower persistence and/or frequencies. Polar WRF performed extremely well during the high wind speed RAS events in the study, with good temporal class alignment, good correlation of surface winds, and a low (good) NRMSD. Synoptic-scale context for the SOM region was provided by Coggins regimes and demonstrated that combining classification sets from different studies that cover overlapping areas, but different scales, is useful in differentiating between large and small scale drivers. In particular, analyzing the SOM classes within the context of these regimes suggested that Polar WRF within AMPS did not accurately resolve the strength and location of cyclones in the Ross Sea. The use of SOMs to increase the temporal granularity of this validation study, particularly the ability to directly compare time-series of classifications of model output and observations, proved to be effective and is widely applicable.

5

CLOUDS OVER THE ROSS ICE SHELF AND SOUTHERN ROSS SEA AS SEEN BY CLOUDSAT AND CALIPSO

INTRODUCTION

Antarctic tropospheric clouds have been the subject of many studies (including relevant reviews by Lachlan-Cope, 2010; Bromwich et al., 2012), though detailed ground or *in-situ* air-based observation campaigns (e.g. Morley et al., 1989; Scott and Lubin, 2014) are difficult, expensive to conduct and therefore rare (Lachlan-Cope, 2010). However, freely available satellite measurements from both active and passive space-borne sensors make some types of detailed studies possible (Comiso and Stock, 2001; Steinhoff et al., 2009; Verlinden et al., 2011; Bromwich et al., 2012; Adhikari et al., 2012). Passive nadir viewing satellite sensors typically have an advantage in their larger spatial scale (2D images of large areas), however they lack altitude data which magnifies the challenges in identifying cloud against snow and ice covered ground that is largely white, highly reflective, and can exhibit similar temperatures (Frey et al., 2008). Active satellite sensors cover a smaller area - typically points along a track - however are more proficient at distinguishing cloud from snow and ice as they collect detailed vertical information by measuring the reflection of controlled light or radio waves emitted by the satellite. In addition to observations, remote or *in-situ*, detailed atmospheric models potentially allow further studies over far greater volumetric and temporal scales (Monaghan et al., 2005; Fogt and Bromwich, 2008; Steinhoff et al., 2009). However cloud is notoriously difficult to model and accurately forecast, particularly over Antarctica and the Southern Ocean (Guo et al., 2003; Fogt and Bromwich, 2008; Bromwich et al., 2012, 2013; Naud et al., 2014), with paucity of observations a contributing factor.

Clouds over the Southern Ocean and Antarctica can consist of predominantly liquid water, ice crystals, or both (mixed-phase) (Haynes et al., 2011; Chubb et al., 2013; Scott and Lubin, 2014; Lawson and Gettelman, 2014). Cloud formation occurs when the level of water vapor in the air reaches saturation and begins to condense (liquid) or freeze (ice). This may be expressed using air temperature and dew point, where the dew point can be defined as the temperature at which a

given air parcel will reach saturation. The dew point is governed by the amount of water vapor (specific humidity) as well as atmospheric pressure, where an increase in either will increase the dew point in turn. For cloud to form a given parcel of clear air must either undergo a temperature decrease to the dew point (e.g. as a parcel is lifted and cools adiabatically, or via radiative cooling or sensible heat flux), or the dew point must be raised via increases in specific humidity (e.g. through evaporation) or pressure (e.g. via a decrease in altitude). Despite the ubiquitous freezing temperatures of the high southern latitudes, liquid water droplets are still frequently observed even over the interior of the continent (Scott and Lubin, 2014; Lawson and Gettelman, 2014). This occurs because, in the absence of ice nuclei, the high surface tension of the tiny water droplets prevents their expansion during the normal freezing process and they become supercooled. This effect is overcome at the homogeneous freezing point, where water will freeze regardless of nucleation or surface tension, which is approximately $-37°C$ in clouds (Meyers et al., 1992; Korolev et al., 2003). However the window between 0 and $-37°C$ where water may exist in either state is large, so liquid and mixed-phase clouds are commonly observed. Cloud composition is important to determine because ice crystals and water droplets have different radiative properties and therefore reflect and absorb different levels of incoming radiation (Haynes et al., 2011; Scott and Lubin, 2014). Cloud composition over Antarctica and the Southern Ocean is currently not well understood or modeled (Haynes et al., 2011; Bromwich et al., 2012; Chubb et al., 2013; Lawson and Gettelman, 2014), however Lawson and Gettelman (2014) have shown that this area is highly sensitive to changes in cloud composition and that model modifications to match observations over the South Pole yielded a net increase in incoming solar radiation of 7.4 Wm^{-2}.

There is little opportunity for evaporation over the Antarctic continent even during the summer months, which means any moisture - and therefore cloud - over the continent must be transported from the open water of the ocean north of the continent perimeter (Tietäväinen and Vihma, 2008). During winter and spring the presence of sea ice greatly increases the distance this moisture must travel from the open ocean to the permanent ice or land of the continent, where work by Comiso and Stock (2001) has shown a link between this seasonal sea ice and cloud. Additionally, the cold temperatures present during this time of year reduce the water carrying capacity of the air which further reduces the amount of moisture that makes the journey inland. However, in certain locations some gaps in the ice do form, exposing areas of open water named 'polynya'. These ice-free areas surrounded by sea ice and land or ice shelf are formed through a combination of oceanographic and atmospheric processes. They contribute a significant quantity of moisture and heat energy to the atmosphere via evaporation and refreezing, with fluxes of up to 400 W m^{-2} for the sensible heat component and 130 W m^{-2} for latent heat (Andreas et al., 1979). If a polynya is large enough, the heat and moisture contribution is also significant enough for substantial convection to occur (Andreas and Cash, 1999). This process creates a thermal internal boundary layer, where warm moist air from the polynya rises, cools, and condenses into fog layers over and

down-wind from the polynya (Morales Maqueda et al., 2004). These fog layers can extend upward for tens to hundreds of meters (Smith et al., 1983; Walter, 1989; Schnell et al., 1989), or even as far as the upper troposphere for exceptional events observed in the northern hemisphere (Dethleff, 1994). The Ross Ice Shelf Polynya is the largest in Antarctica with an average area of $27,000$ km^2 and a maximum area almost twice that (Zwally et al., 1985). As the name indicates, the Ross Ice Shelf Polynya is located next to the Ross Ice Shelf (RIS), along the northern edge, potentially providing a rich source of heat and moisture for the RIS given the appropriate wind conditions.

The RIS is a largely flat expanse of permanent ice covering approximately $487,000$ km^2 fed by both the West Antarctic Ice Sheet (WAIS) and East Antarctic Ice Sheet (EAIS). The western edge of the roughly triangular-shaped shelf is bounded by the 2 km high barrier of the Transantarctic Mountains (TAM), with the EAIS behind. Katabatic winds from the EAIS converge through multiple glacial valleys in the TAM (Bromwich, 1989), while corresponding drainage from the WAIS flows onto the eastern and southern edges of the RIS at the Siple Coast (Bromwich and Liu, 1996; Bromwich et al., 1992). This katabatic drainage is known to move significant quantities of dry air onto the RIS from the interior of Antarctica (Parish and Bromwich, 1987, 1997, 1998). The Ross Sea is located along the northern boundary of the RIS and frequently experiences large low pressure systems originating off the coast of Adélie Land located well to the north-west that advect moist marine air from the ocean/sea ice onto the RIS, often via the WAIS and Siple Coast (Nicolas and Bromwich, 2011). This combination of cyclones, the barrier presented by the TAM, and katabatic drainage helps to feed a southerly wind regime that dominates the climatology of the RIS. Known as the Ross Ice Shelf airstream (RAS) (Parish et al., 2006), its signature is a corridor of high winds flowing north, parallel to the TAM and out into the Ross Sea which can be seen on timescales ranging from monthly to seasonal to yearly.

The NASA A-Train of satellites contains three platforms that are particularly useful for cloud observations: Cloud-Aerosol Lidar and Infrared Pathfinder Satellite Observations (CALIPSO), CloudSat, and Terra. CloudSat and CALIPSO use active sensors (radar and lidar respectively) to gather detailed vertical information in a line along a track, while Terra houses the MISR and MODIS multi-spectral 2D imaging sensors (among others). A recent study by Scott and Lubin (2014) investigated clouds over Ross Island - located at the north-west corner of the RIS - using a spectroradiometer installed near McMurdo station as well as observations from the NASA A-Train. Two main moisture sources were identified: marine air intrusions originating over the WAIS and crossing the RIS before finally reaching Ross Island, and moist air advection from the Ross Sea. Observed clouds over Ross Island contained water in both solid and liquid phases, where moisture from marine air intrusions over the WAIS tended to be predominantly ice-based while moisture from the closer Ross Sea area was more likely to be (but not exclusively) liquid-based. Large cyclones in the Ross Sea were not observed to contribute significant levels of moisture to Ross Island.

In a follow-up study, Scott and Lubin (2016) extend this work further to show a link between high ice content and increased vertical motion of the air parcel prior to observation.

Verlinden et al. (2011) also made extensive use of observations from A-Train satellites, using the combined CloudSat/CALIPSO 2B-GEOPROF-LIDAR (Mace and Zhang, 2014) cloud product on a much larger scale over Antarctica and the Southern Ocean. By producing vertical profiles for latitudinal 'bands' on a seasonal time scale they found that cloud increased during winter over the continent and surrounding ocean. They suggest that the comparatively sensitive nature of the saturation vapor pressure for ice relative to that for liquid water is at least partially responsible for this. The profiles produced also revealed two distinct local maxima over the 'ocean' latitude band, with one at surface level and the other near the top of the troposphere which has implications for the current study as discussed below. The increase of cloud during winter is contrary to the findings of Adhikari et al. (2012), who calculated seasonal variations spatially and found that summer and autumn featured higher cloud incidence than winter and spring over most of Antarctica and Southern Ocean, but particularly over the RIS. Sea ice was suggested as a contributing factor, blocking evaporation that occurs over open water, as were the extremely low temperatures. Low-level cloud featured the highest inter-seasonal variability, with low incidence during winter and reduced incidence during spring relative to summer and autumn.

This study aims to quantify cloud incidence over the RIS and southern Ross Sea using the CloudSat/CALIPSO 2B-GEOPROF-LIDAR (Mace and Zhang, 2014) product, both spatially and vertically. For comparison, seasonal differences will be presented before a more detailed analysis using synoptic regimes identified by Coggins et al. (2014). A broad spatial overview is presented before a method of combining multiple A-Train passes is used to collate vertical information from several similar passes for each regime.

DATA AND METHODS

Synoptic climatology

There have been multiple studies of the synoptic-scale atmospheric processes in the greater Ross Sea/RIS region, with the development of several climatologies using clustering techniques (Seefeldt et al., 2007; Coggins et al., 2014; Nigro and Cassano, 2014b; Coggins and McDonald, 2015, for example). To provide context on atmospheric circulation for the duration of this study, classifications and regimes developed by the work of Coggins et al. (2014) and Coggins and McDonald (2015) are used. Five broad synoptic-scale regimes, hereafter referred to as 'Coggins regimes', encompass 20 classes created by applying the k-means clustering technique to 33 years of ERA-Interim reanalysis

(Dee et al., 2011) 10 m winds in the Ross Sea/RIS region. The ERA-Interim dataset has been found to be particularly effective over the RIS (Bracegirdle, 2013; Coggins et al., 2014) which makes it well-suited for the area of this study. The 20 classes grouped into five regimes were found to be representative of conditions in the area (Coggins et al., 2014) and spanned the entire time period of available cloud observations so were an obvious choice for this analysis.

The five Coggins regimes are presented in Figure 5.1 (a reproduction of Figure 2 from Coggins et al. (2014)) which depicts the mean wind field and mean sea level pressure (MSLP) anomaly for each regime. The weak northern cyclonic (WNC) and strong northern cyclonic (SNC) regimes feature cyclones to the north of the RIS, with the relative 'weak' and 'strong' ratings referring to their effect on the RIS; WNC generally provides weak forcing and low wind speeds while SNC features a strong synoptic pressure gradient force (PGF) and high wind speeds over the RIS. The RAS regime covers the strongest winds over the RIS and typically features a strong cyclone to the north and east that provides a large PGF over the ice shelf. The weak southern cyclonic (WSC) regime is associated with relatively weak cyclones and mesocyclones positioned over the RIS, with medium wind speeds and PGF. Finally, the weak synoptic (WS) regime covers periods where a very weak PGF and very low winds are present over the RIS. Regime (annual) frequencies are displayed as percentages in Figure 5.1, with WS being the most prevalent (~30%) followed by RAS (~25%) and WNC (~25%) then SNC (~13%) and WSC (~10%). There is no strong seasonality to the SNC regime, however the RAS, WSC, andWNC regimes tend occur more frequently during winter while WS strongly favors the summer months.

CloudSat and CALIPSO

CloudSat (Marchand et al., 2008) and CALIPSO (Liu et al., 2009) are two satellites that exist within the NASA 'A-train' - a group of satellites with identical orbits that pass over the same parts of the earth within a narrow time window (effectively co-located for the purposes of this study). CloudSat carries a millimeter-wavelength (94 GHz) radar with a vertical resolution of ~240 m and a sea-level footprint of 1.4 km x 1.7 km. Designed to detect tiny water droplets within clouds while also penetrating through optically dense upper layers to detect further layers at lower altitudes, it struggles to resolve cloud below ~1 km above ground level (AGL) due to its large vertical bin size and interference from ground returns (Marchand et al., 2008; Chan and Comiso, 2011). The Cloud-Aerosol LIdar with Orthogonal Polarization (CALIOP) instrument carried by the CALIPSO satellite provides vertical resolution of the order of 30 - 60 m with a circular sea-level footprint 100 m in diameter as well as the ability to accurately detect cloud down to ground level, however suffers from reduced sensitivity during daylight operations and cannot penetrate thick cloud

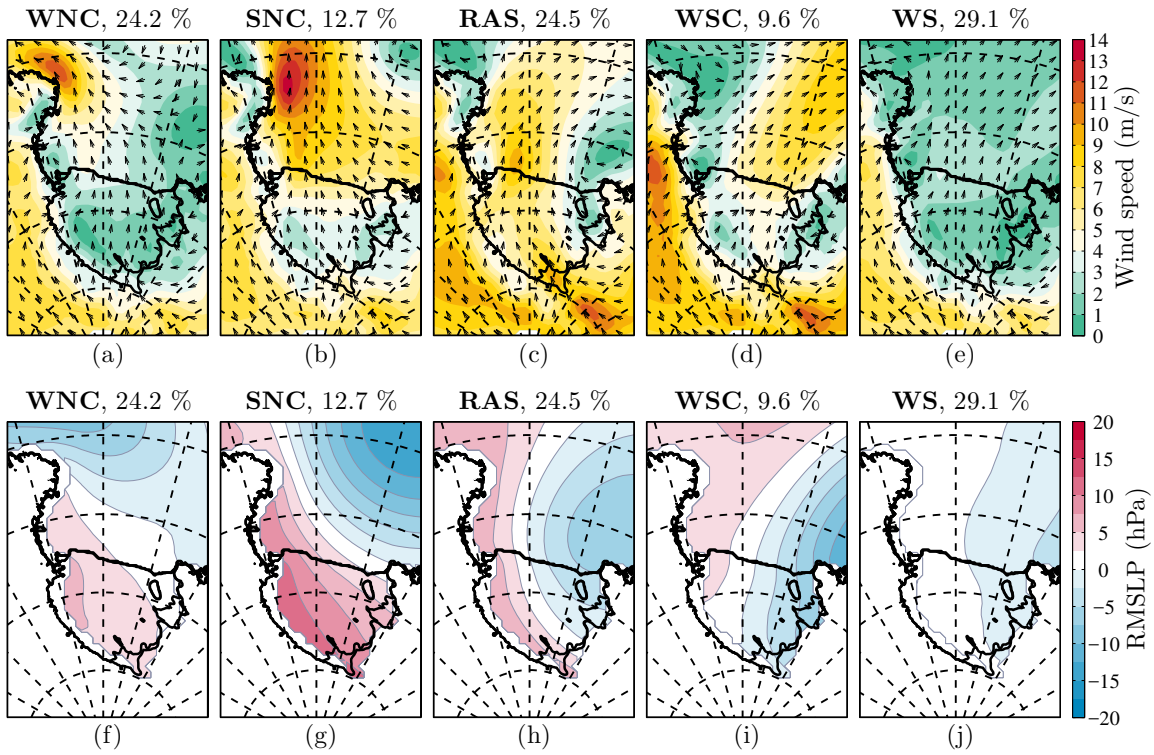

Figure 5.1: Reproduction of Figure 2 from Coggins and McDonald (2015) showing Coggins regimes. Original caption (CMJ2014 = Coggins et al. (2014)): *(a-e) Surface (10 m) winds of CMJ2014 synoptic regimes. Arrows indicate direction in which wind is flowing and are plotted relative to grid north. Background color represents the mean wind speed. Percentages above each diagram display the total frequency of the particular regime, computed annually. (f-j) As in Figures 2a-2e but for relative MSLP. Regime names are the following: WNC = Weak Northern Cyclonic, SNC = Strong Northern Cyclonic, RAS = Ross Ice Shelf airstream, WSC = Weak Southern Cyclonic, and WS = Weak Synoptic.*

(approximately five optical depths) so may miss lower level cloud if it is obscured (Mace and Zhang, 2014).

The primary source of vertical cloud information from CloudSat is the GEOPROF (geometric profile) product (Marchand et al., 2008), which provides a cloud mask for each vertical level along with radar return intensity and an estimate of absorption due to oxygen and water vapor. The corresponding data product from CALIPSO (CALIOP) is the vertical feature mask (VFM) (Vaughan et al., 2004), a description of what features (cloud/aerosol/clear air and subcategories) were detected for a given footprint for each vertical level. To create the widely available 2B-GEOPROF-LIDAR combined product used by this study, the VFM product is simplified to a simple cloud/no cloud flag using a threshold of '20' (Mace et al., 2009) for each volumetric bin (1.4 km x 1.7 km x 240 m). The much smaller (100 m x 100 m x 30 m) CALIPSO bins are then matched with the CloudSat bins, where multiple CALIPSO bins are expected to fall within each CloudSat bin. The final 2B-GEOPROF-LIDAR result is the greater of the fraction of cloudy CALIPSO bins or a positive

hydrometeor result from CloudSat (Mace et al., 2009; Mace and Zhang, 2014). While this product combines the best aspects of both sensors, it is still possible to miss some types of cloud, particularly low-level cloud missed by CALIPSO due to obscuration by higher-level cloud or if it optically thin as CloudSat will not be able to distinguish these from ground clutter (Chan and Comiso, 2011; Mace and Zhang, 2014). This study uses active sensors instead of passive, such as MODIS, as they are less affected by the long polar night during winter time and do not suffer the same consistent cloud detection problems over ice surfaces (Frey et al., 2008). Analysis of four years and ten months of data (2006-06-19 to 2011-04-17) is presented.

Satellite track aggregation

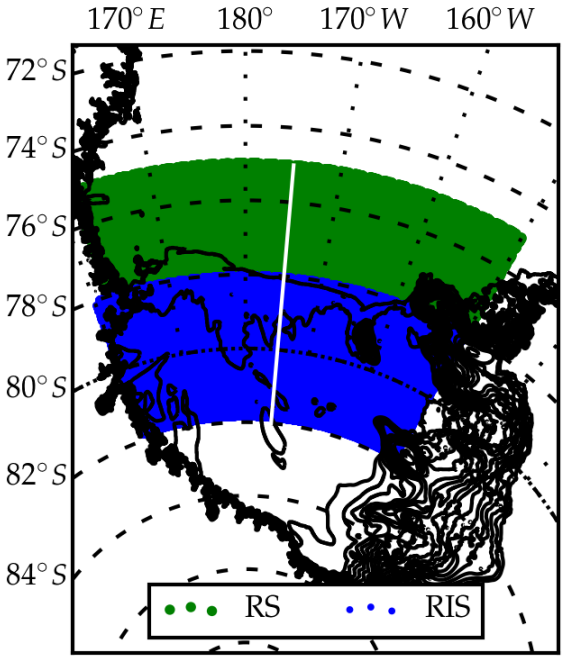

Figure 5.2: Ross Sea (RS) and Ross Ice Shelf (RIS) quadrant definitions. Data window is bounded by 75°S, 160°E (upper-left) and 82°S, −150°E (bottom-right); 82°S is the southern-most limit of CloudSat/CALIPSO passes. The Ross Sea/RIS boundary is defined as 78°S which roughly follows the edge of the RIS. The white line marks the approximate center of the sectors at −175°E.

The A-train 'passes' over the RIS 7 or 8 times each day, with a slight shift in track position day-to-day in a cycle that approximately repeats every 16 days. While coverage is more dense than most of the globe, it is still insufficient to build a reliable spatial (x/y) composite for the purposes of this study. Comparing 92 unique pass/day combinations for a series of weather regimes is infeasible, so two strategies were employed to reduce this: binning of individual measurements into quadrants (Fig. 5.2), and the creation of 'virtual tracks' of approximately co-located passes of

which two were ultimately selected (Fig. 5.4). The quadrants cover the RIS and part of the Ross Sea, loosely defined by the edges of the ice shelf (160°E to −150°E) and extending from the bottom of the A-train track (~82°S) to 75°S. The RIS/Ross Sea border is defined by the 78°S longitude line.

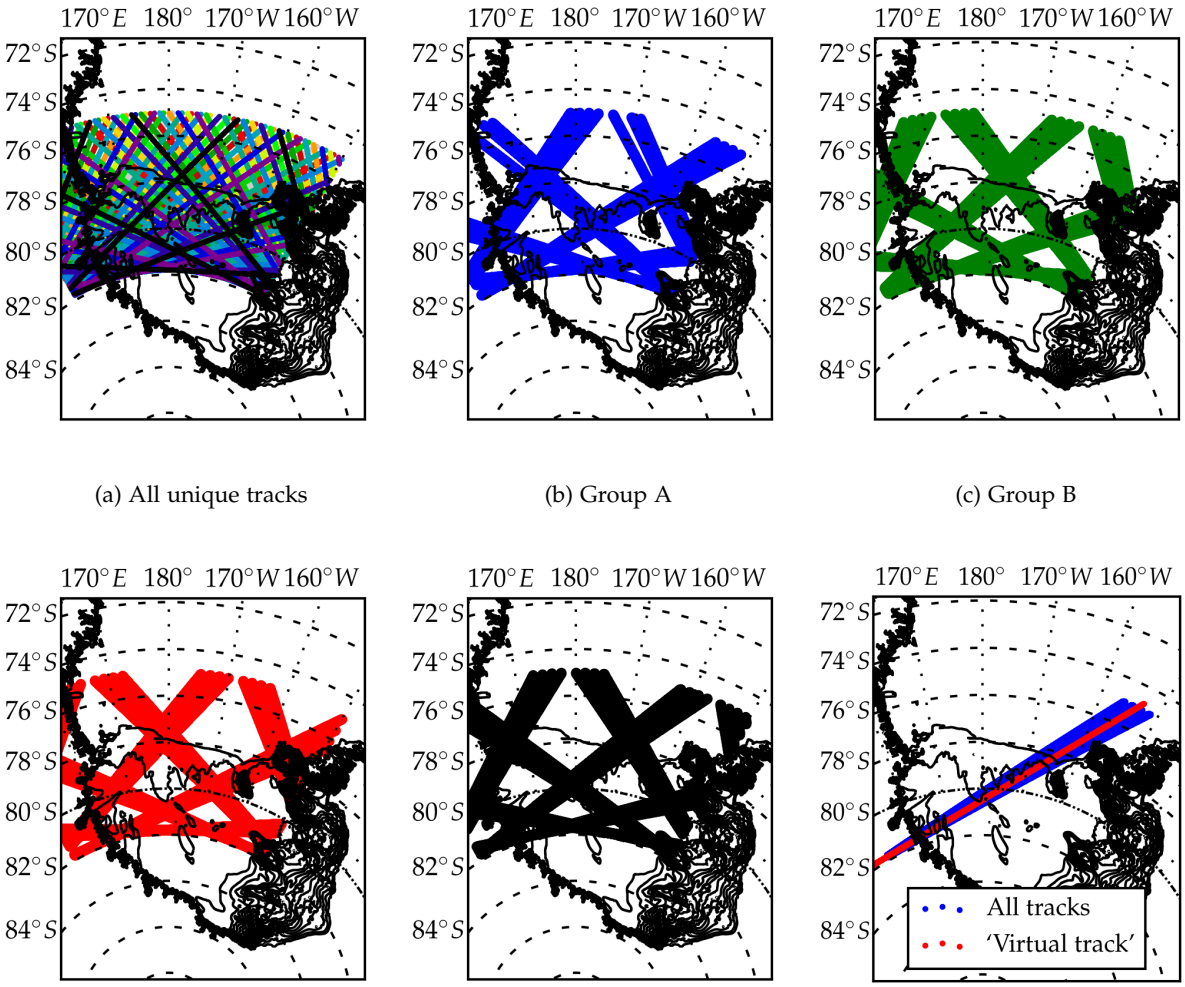

(a) All unique tracks (b) Group A (c) Group B

(d) Group C (e) Group D (f) Virtual track 5, group A

Figure 5.3: Process of definition of satellite swaths. Sub-figure (a) shows all unique satellite tracks (92 total), while (b) - (e) separate these into groups (4 total). Sub-figure (f) shows a single swath (blue) - the unique combination of group 'a' (b) and track '5' - and the corresponding 'mean track' for the swath (red).

The virtual tracks are defined by splitting the 16 unique daily patterns into 4 'groups', where each group consists of 7 or 8 sets of 4 approximately co-located 'tracks' for a total of 29 'virtual tracks'. This process is illustrated in Figure 5.3, where Figure 5.3a shows all unique passes and Figures 5.3b - (e) shows those same passes color-coded into the 4 groups.

While all four passes in a virtual track are close to each-other, the distance between any two is typically of the order of tens of kilometers. In order to compare these tracks their latitude/longitude-

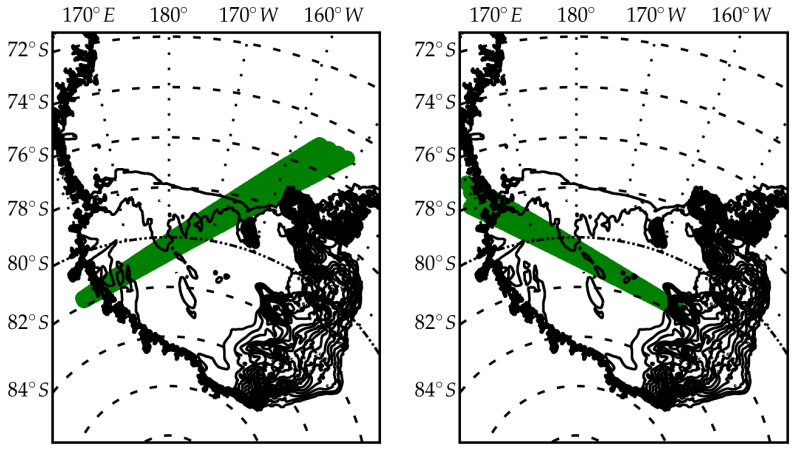

(a) Virtual track A_5 (b) Virtual track B_3

Figure 5.4: Virtual CloudSat/CALIPSO satellite tracks A_5 (a) and B_3 (b) - see Section 5.2.3 and Figure 5.3.

per-point coordinate system is converted to a one-dimensional distance-along-a-track coordinate system for every pass. A 'mean track' for the swath is determined (Figure 5.3f) and bins two kilometers in length are defined along the track. Each bin is infinitely wide and perpendicular to the mean track, thereby reducing the two-dimensional horizontal location information to a single dimension. Each pass is processed into the coordinate system described, preserving all vertical levels. The two kilometer bin size is designed such that most bins will contain between one and two data points, where the mean distance between raw data points sits between 1.0 and 1.1 kilometers (dependent on location). If multiple values are present within a bin the mean is taken. Finally, cloud fractions for each vertical bin are clipped to 100% or 0% with a cutoff threshold of 50% (consistent with Verlinden et al., 2011). Of the 29 virtual tracks, 2 were selected as the best candidates for further analysis based on their coverage of the RIS and are displayed in Figure 5.4.

RESULTS

Overview

As an initial point of comparison with the previous work of Verlinden et al. (2011) and Adhikari et al. (2012) (where both used CloudSat/CALIPSO data from a similar time period but over a far larger area), this study uses three-month seasons to reduce the granularity of the observations: December-January-February (DJF), March-April-May (MAM), June-July-August (JJA), and September-October-November (SON). Initial overall statistics for cloud incidence were calculated by splitting the area of interest into two sectors: the Ross Sea and the RIS (see Figure 5.2). Each

sector was also split into eastern/western halves to create four quadrants as indicated by the white line at −175°E in the figure. Cloud incidence was calculated for each sector and quadrant for each season and for each Coggins regime (Coggins and McDonald, 2015, see Fig. 5.1) and is presented in Table 5.1. Based on these results, the regimes and seasons were combined to produce cloud incidence values for binary 'summer' (DJFMAM) and 'winter' (JJASON) categories with spatial results presented in Table 5.2. These definitions were chosen to coincide with below/above mean levels of sea ice according to Parkinson and Cavalieri (2012). Vertical cloud distributions for each sector (Figure 5.5) were computed for seasons (Figure 5.5a), Coggins regimes (Figure 5.5b), and the combination presented in Table 5.2 (Figure 5.5c and Figure 5.5d). Distributions of cloud top height and longitude are examined in a two-dimensional histogram for both sectors for each Coggins regime in Figure 5.6. Finally, two of the 'virtual tracks' outlined in Section 5.2, illustrated in Figure 5.4, are investigated in greater detail using Figure 5.7 (refer Figure 5.4a) and Figure 5.8 (refer Figure 5.4b).

Spatial statistics

Table 5.1 shows seasonal cloud incidence below 10 km is highest during DJF and lowest during JJA by a large margin in the Ross Sea (9 to 16 percentage points (pp)) and to a lesser extent over the RIS (8 to 9 pp). Some differences are seen between MAM and SON but these are much smaller (0 to 5 pp). The maximum values presented by the Coggins regimes are more complicated, however the minimum cloud incidences are universally attributed to the WSC regime associated with relatively weak cyclones and mesocyclones positioned over the RIS. The dominant maximum cloud regime over the Ross Sea is SNC (see Figure 5.1), typically associated with deep synoptic cyclones to the north of, or over, the study area. Cloud over the western RIS appears to be more closely tied to the RAS regime (high winds and often large cyclone), however the low winds and weak forcing of the WS regime accounted for the highest incidence over the eastern portion; it is worth noting that this quadrant shows the least variation between regimes while the western Ross Sea shows the most. Across all regimes and seasons the Ross Sea was cloudier than the RIS, with the eastern halves of each sector typically cloudier than the west. The RIS also shows a smaller variation in cloud cover for both regimes and seasons, however the seasonal effect is the smaller (again) of those. All values in both Table 5.1 and Table 5.2 that are separated by at least 2 pp (and most that are separated by 1 pp) are statistically significant using a binomial test and a 99% confidence interval.

The Coggins regimes from Table 5.1 were divided further by splitting the calendar year into binary 'summer' (DJFMAM) and 'winter' (JJASON) categories. Presented in Table 5.2, this method of merging synoptic regimes with broad seasons explains more variance than either alone. There

Table 5.1: Cloud incidence by Coggins regime and season, defined as the percentage of sample points with any cloud fractions greater than 50% in any vertical bin below 10 km ASL. Values are calculated for the east and west halves of the Ross Sea (RS) and RIS sectors in Figure 5.2, where the dividing line is defined as −175°E (see white lines in Figures 5.2 and 5.6). Orange cells indicate maximum values for each column and group, while blue cells indicate minima. All differences greater than 2 percentage points (pp) are significantly different using a binomial significance test with a threshold of 99%.

	All	RS	RIS	W-RS	E-RS	W-RIS	E-RIS
WNC	63%	71%	59%	71%	71%	58%	60%
SNC	68%	80%	62%	75%	84%	62%	63%
RAS	66%	73%	63%	68%	78%	64%	62%
WSC	54%	58%	52%	48%	67%	47%	58%
WS	64%	71%	61%	67%	74%	58%	64%
DJF	69%	80%	65%	76%	83%	63%	67%
MAM	65%	70%	63%	67%	73%	62%	64%
JJA	59%	65%	57%	60%	69%	54%	59%
SON	62%	71%	58%	67%	75%	58%	59%
All	64%	71%	60%	67%	75%	59%	62%

are larger inter-regime differences (28 pp - SNC-WSC in winter over western Ross Sea) and more extreme minimum (41% WSC in winter over western halves) and maximum (88% SNC in summer over eastern Ross Sea) cloud values relative to Table 5.1. Once again, the SNC regime is responsible for the majority of maximum cloud incidence, however its effect over the RIS is reduced during winter when the RAS regime dominates. Again, WSC features the lowest cloud incidence of all the regimes, however the spatial variance is noticeably larger during winter than summer.

Dividing the Ross Sea and RIS sectors into east and west components revealed more about the various regime/season combinations. Regardless of season, the east/west differences for either sector are mainly non-significant during the WNC regime, however the other regimes do feature significant differences. The RIS tends to see less variation than the Ross Sea, particularly during winter SNC occurrences and summer RAS events. The largest overall difference between east

Table 5.2: As Table 5.1, except Coggins regimes are integrated with generalized 'Summer' and 'Winter' seasons defined by combining the months in Table 5.1 with sea ice extents - Summer covers December to May (below average sea ice cover) while Winter covers June to November (above average sea ice cover)(Zwally et al., 2002). Orange cells indicate maximum values for each column and group, while blue cells indicate minima. All differences greater than 2 pp are significantly different using a binomial significance test with a threshold of 99%.

		RS	RIS	W-RS	E-RS	W-RIS	E-RIS
Summer	WNC	73%	62%	73%	73%	61%	63%
	SNC	85%	67%	81%	88%	67%	67%
	RAS	73%	64%	67%	79%	64%	64%
	WSC	66%	59%	58%	73%	57%	60%
	WS	75%	66%	72%	79%	62%	69%
Winter	WNC	68%	56%	68%	68%	55%	57%
	SNC	75%	58%	69%	81%	58%	59%
	RAS	73%	62%	68%	77%	64%	60%
	WSC	53%	48%	41%	63%	41%	56%
	WS	66%	57%	63%	68%	54%	59%

and west occurs during the WSC regime in winter over the Ross Sea, where the western half experiences the minimum cloud incidence of all possible regime/season/location combinations at 41%, while the eastern half features an incidence rate 22 pp larger at 63%. The RIS also experiences a large difference (15 pp - the second-largest overall) in cloud incidence during WSC regimes during winter, although WSC remains the regime with the lowest incidence.

Vertical distribution

Vertical distributions of cloud incidence for each of Table 5.1 and Table 5.2 (except east/west distinction) are shown in Figure 5.5. Variations in vertical distribution of cloud incidence are seen for each season (Fig. 5.5a), with a more pronounced spread over the RIS, however the effect is visibly less than variation between regimes and season/regime combinations (Fig. 5.5 (b) - (d)). In

all seasons there is a local maximum in cloud incidence at ~0.5 km ASL, with another between this point and ~8.5 km ASL where there is a sharp decrease in cloud.

Figure 5.5b shows an advantage to using a classification scheme based on an observable physical property where one is available and meaningful. As with Figure 5.5a, Figure 5.5b shows cloud incidence is greater over the Ross Sea, however it also shows that much of this may be attributed to the SNC regime (the only regime that does not feature a local maximum at ~0.5 km ASL). The RAS and WNC regimes are comparable to the seasonal Ross Sea values, while the WSC and WS regimes show no second maximum at higher altitudes and feature low cloud incidence overall. Vertical distributions over the RIS show a reduction in inter-regime variability, opposite to the increase in inter-season variability seen in Figure 5.5a. The impact of the SNC regime is reduced, while the RAS impact increases. The other regimes, representing reduced synoptic forcing and lighter winds, all feature extremely similar distributions and have less cloud incidence overall, though the WNC and WS regimes both feature the largest amounts of low-level cloud with very distinct maxima around 0.5 km ASL.

Figures 5.5 (c) & (d) show the increased benefit again in combining the Coggins regimes with a form of seasonality. During 'winter' (JJASON - Fig. 5.5c) the vertical distribution of the maximum peak for the SNC, RAS, and WNC regimes rises toward ~8 km), decreasing mid-level cloud incidence relative to 'summer' (DJFMAM - Fig. 5.5d). This results in the WNC regime surpassing the RAS regime for upper-level cloud during winter, whereas during summer their upper-level vertical distributions are very similar. Closer inspection of low-level RAS cloud incidence shows that there is a large peak during winter over the Ross Sea that is not present during the summer and the low-level cloud incidences for the other regimes are more widely spread. The opposite effect is seen over the RIS, with no discernible difference in RAS low-level cloud incidence and a decrease in the overall spread of the regime low-level cloud incidences relative to summer. Finally, there is a small increase in mid-level cloud around 2.5 km ASL for the WSC and WNC regimes during summer over the RIS, though the effect is more pronounced for WSC.

Cloud top height

Figure 5.6 is a series of two-dimensional histograms investigating the distributions of cloud top height and longitude for both the Ross Sea (Figure 5.6a) and the RIS (Figure 5.6b) for each Coggins regime (Coggins and McDonald, 2015). The cloud top is taken as the highest vertical bin that contains a cloud concentration greater than 50% for each point, where points are grouped into 2°longitude bins. Vertical bins are at 250 m, 750 m, 1500 m, then every 1000 m until 15000 m to preserve some of the low-level structure seen in Figure 5.5. The vertical values for each longitude bin sum to the total cloud fraction for that longitude bin; the top-left plot of both sub-figures

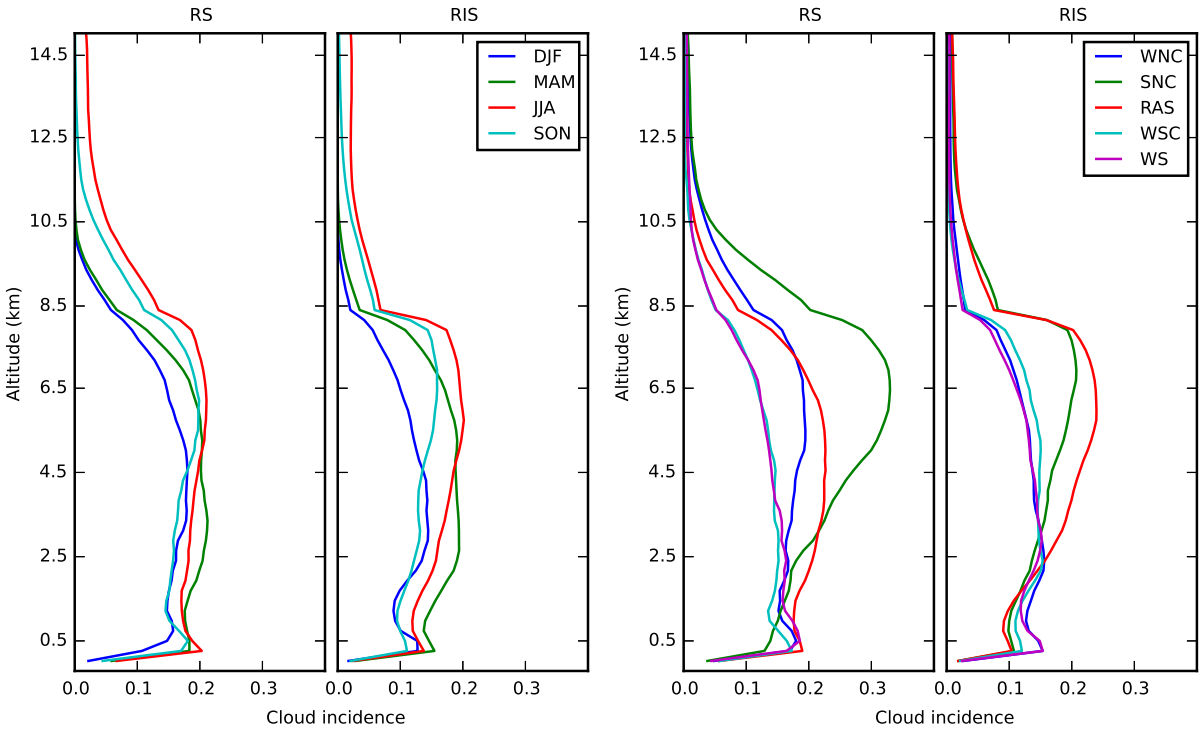

(a) Vertical distribution by season

(b) Vertical distribution by Coggins regime

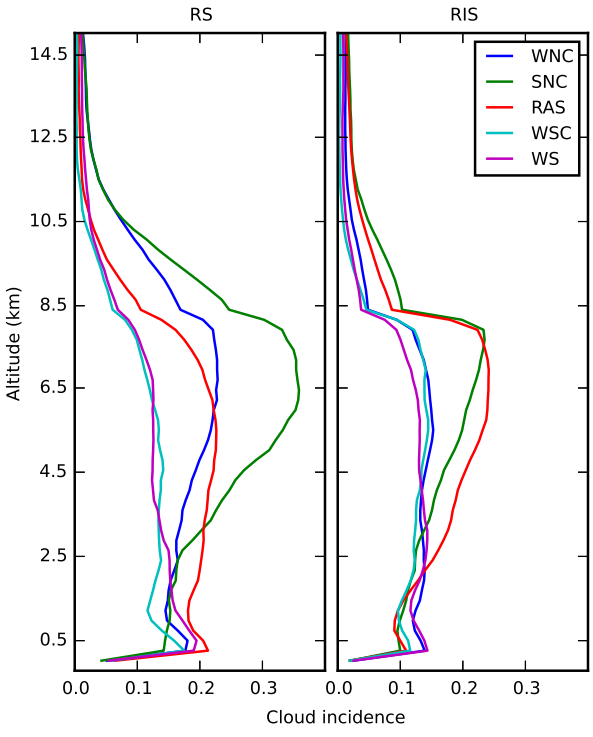

(c) Vertical distribution by regime - Winter

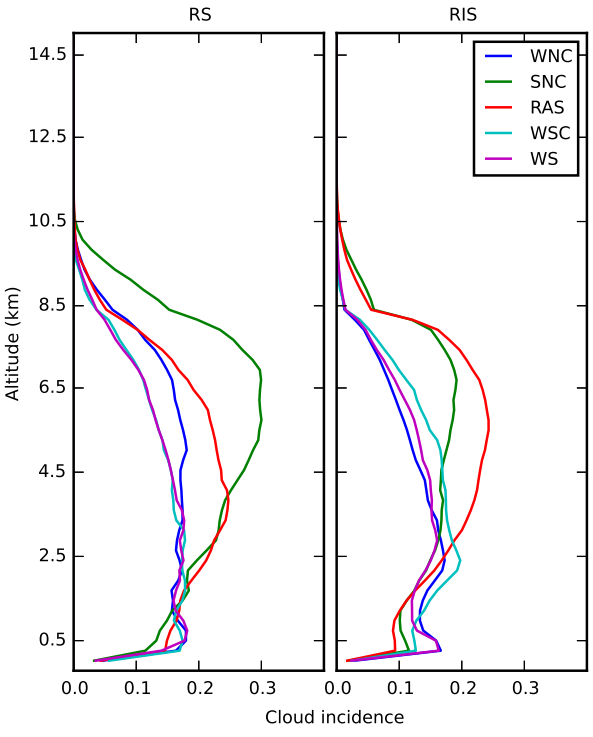

(d) Vertical distribution by regime - Summer

Figure 5.5: Cloud vertical distribution by season (a) and Coggins regime (b) for both Ross Sea (RS) and RIS sectors (Figure 5.2). Most vertical levels are significantly (95%) different between (a) and (b) (see Table 5.1).

shows the distributions for the entire period as a point of reference. Immediately noticeable is the noisier signal in Figure 5.6a (relative to Figure 5.6b), which is an unavoidable side-effect of a lower number of samples due to both the smaller area of this sector and the spatial distribution of satellite tracks. However, while the RIS longitude bins have approximately two-and-a-half times the number of points as the Ross Sea, the smallest Ross Sea bin population is still around 11,300 points.

There are two distinct bands of cloud top heights in almost all plots in Figure 5.6, however most regimes display a preference for one of the two. The SNC regime is strongly associated with a high cloud top height over both the Ross Sea and RIS, with a similar effect for the RAS regime that is stronger over the RIS. The WS regime features a lower cloud top height, however there is more variation over the full height range. Both the WNC and WSC regimes are a mix of the others. At higher cloud top heights there is a tendency for the distribution to shift further east across both areas, an effect which is most noticeable for the SNC and WSC regimes. Figure 5.6b shows a third distinct grouping of cloud top heights at around 3 km ASL which is present across all regimes. This feature is restricted to the western half of the RIS, beginning at the edge of each plot, and is likely associated with the presence of the TAM. Additionally, the surface-level cloud layer in this figure is associated with the eastern half to two-thirds of the RIS. The RAS regime cloud top height distribution over the Ross Sea has the largest bimodal signature which is consistent with Figure 5.5b (two large and distinct local maxima). Finally, the upper-level cloud top height over the RIS (Figure 5.6b) appears to have a hard ceiling around 8 km ASL which is not seen over the Ross Sea (Figure 5.6a).

Virtual tracks

To compare CloudSat/CALIPSO tracks in more detail, 'virtual tracks' were created as described in Section 5.2. Two of the most interesting tracks are presented here, named '`A_5`' and '`B_3`' for their corresponding 'group' and 'pass' names. These virtual tracks are plotted in Figure 5.4. Profiles from the SNC and WS Coggins regimes are presented as they represent extreme cases, as well as the RAS Coggins regime as it represents an interesting and otherwise well-studied surface wind regime (Parish et al., 2006; Steinhoff et al., 2009; Seefeldt and Cassano, 2012; Nigro and Cassano, 2014a). These figures present cloud incidence at each vertical bin, not cloud top height statistics as presented in Figure 5.6.

Virtual track `A_5` (Figure 5.4a) stretches from the TAM in the middle of the western edge of the RIS, out over the Ross Sea past Roosevelt Island and Cape Colbeck. Vertical profiles along the track for the SNC, RAS, and WS Coggins regimes are shown in Figure 5.7. They agree well with the distributions shown in Figure 5.5b, where the SNC regime features a substantial amount of higher-

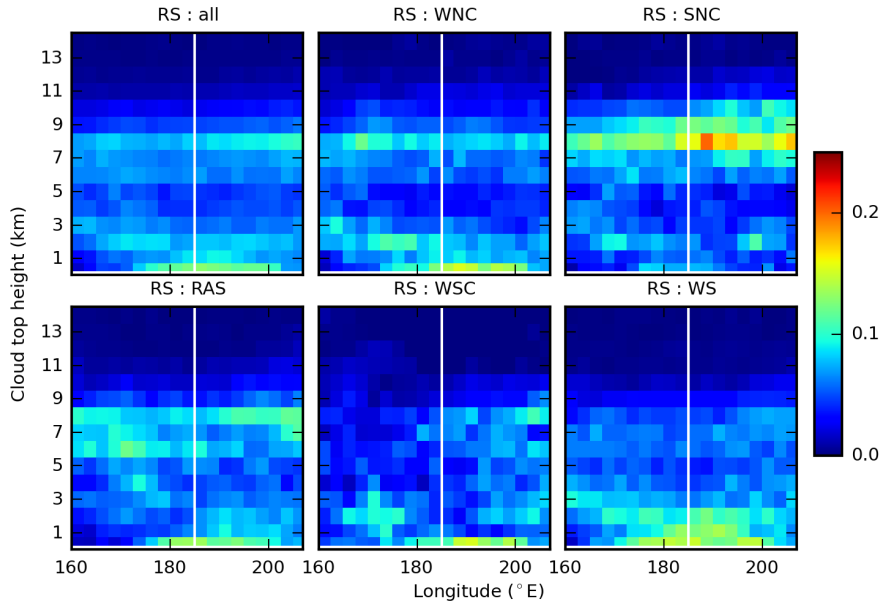

(a) Ross Sea

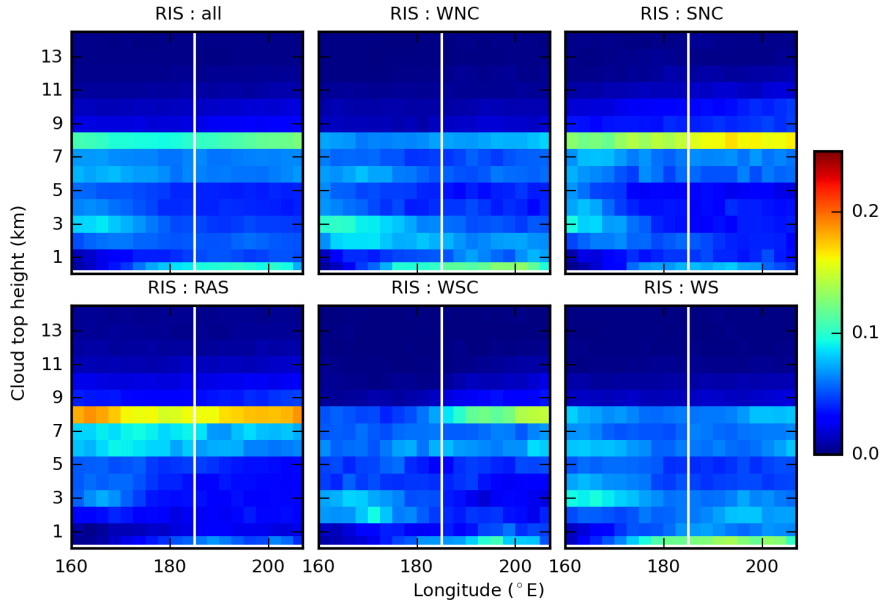

(b) Ross Ice Shelf

Figure 5.6: 2D histogram of cloud top height and longitude by Coggins regime for the Ross Sea (RS) (a) and Ross Ice Shelf (b). There are three smaller vertical bins near sea level - 0.25/0.75/1.5 km ASL - with the rest of the bins running from 1.5 km ASL to 14 km ASL in 1.0 km increments. The top-left plot in each sub-figure represents the entire period, while the others reflect distributions during each Coggins regime. Longitude bins are 2.5° wide and contain 9000 to 29000 (27000 to 73000) points over the Ross Sea (RIS), depending on the regime. The approximate center of the RIS is shown as a white line located at −175°E (same as Figure 5.2).

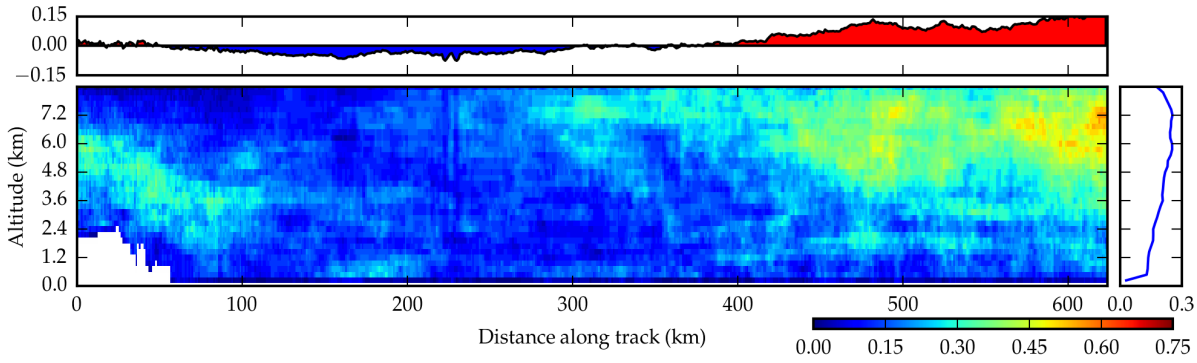

(a) SNC regime

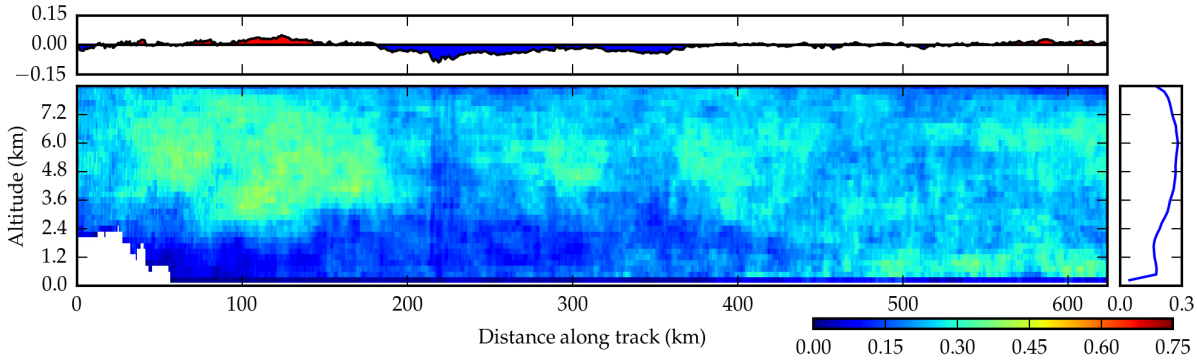

(b) RAS regime

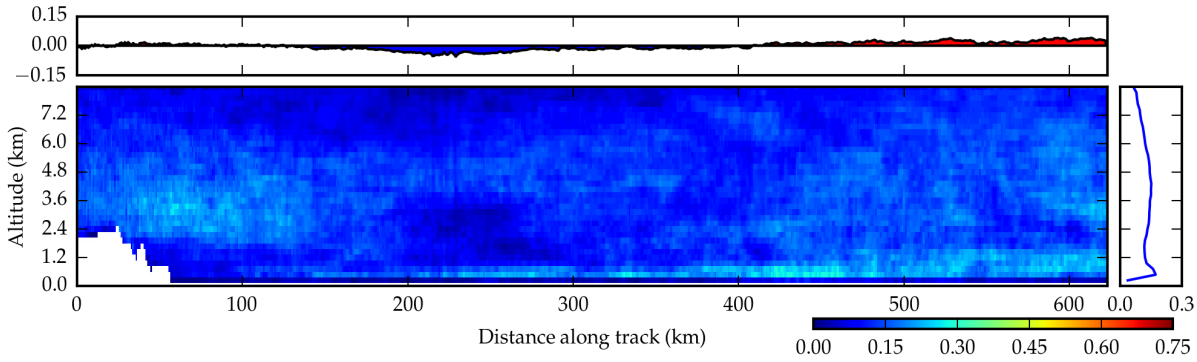

(c) WS regime

Figure 5.7: Vertical cloud profiles for virtual track A_5 (Figure 5.4a). Heat map shows cloud incidence (see color bar) for each ~250 m vertical bin along the track running east-west. Upper line plot shows vertically integrated cloud incidence anomaly from the track mean, with red/blue shading indicating sign. Right-hand line plot shows the vertical distribution of cloud. Data are clipped to <~8.5 km to enhance the visible structure as beyond this altitude cloud fractions decrease substantially.

level cloud over the Ross Sea and less over the RIS. The RAS regime shows a large concentration of higher-level cloud over ~2.5 km ASL near the TAM, reducing along the track further into the RIS. As the track reaches the sea/sea ice of the RIS, low-level cloud increases which is also seen in

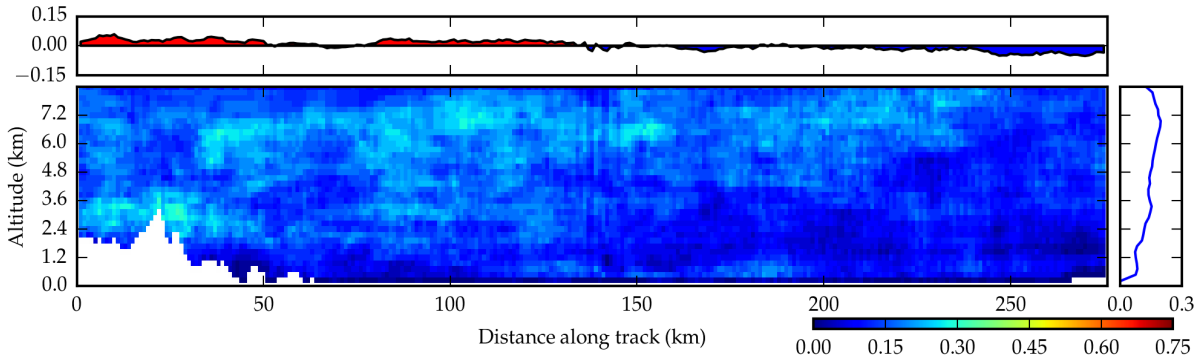

(a) SNC regime

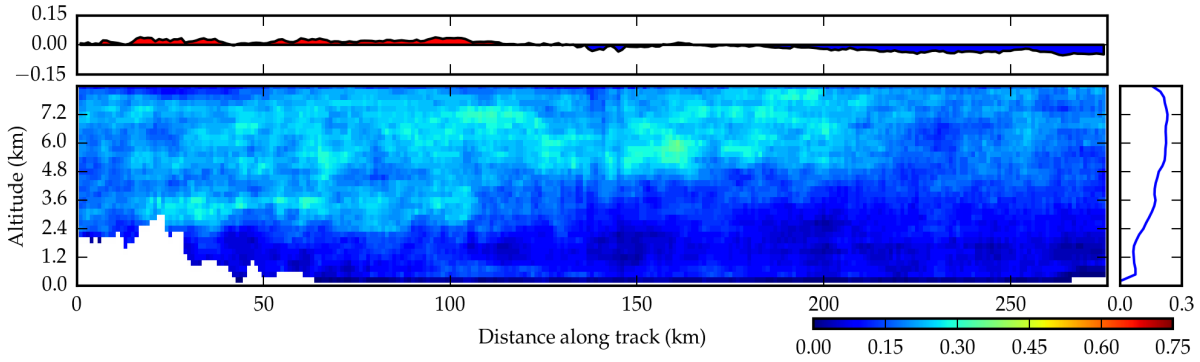

(b) RAS regime

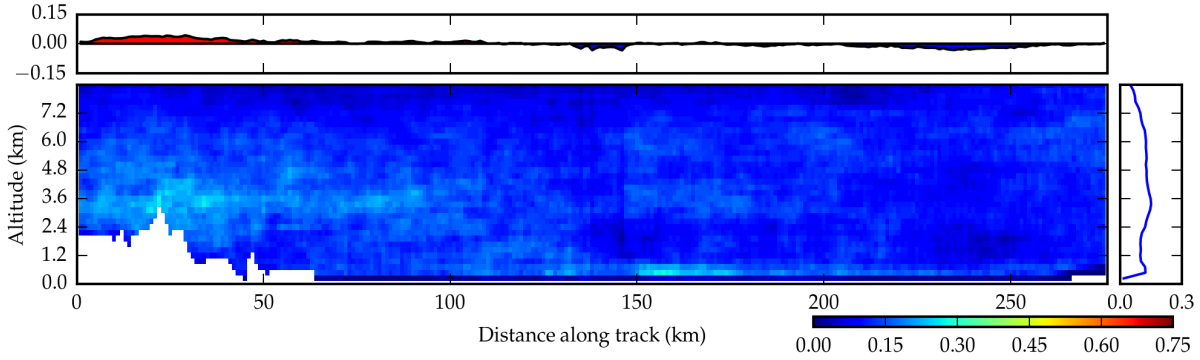

(c) WS regime

Figure 5.8: As Figure 5.7, but for virtual track B_3.

Figure 5.5b (Ross Sea) upon close inspection. There was little cloud during the WS regime, with some mid-level cloud near the TAM and some very low-level cloud over the RIS.

The profiles of virtual track B_3 in Figure 5.8 show reduced cloud levels in general which is expected over the RIS, especially the western half (see Table 5.1). For this track the RAS regime shows the highest cloud incidence, with most located above ~2.5 km ASL. The cloud floor lifts and the concentration of higher-level cloud decreases as the track heads south-east across the RIS. There is a patch of low-level (~750 m ASL) cloud between the 180 km and 220 km points along the track (approximately 80°S, 175°E) which can be associated with three of the six RAS sub-classes (presented in Coggins et al., 2014). The first, with the largest cloud incidence, is class (2,4) which

shows very calm conditions in that location, while the other two are classes (1,5) and (2,5) which feature narrow channels of medium-high winds through the location. The SNC regime features a similar pattern to the RAS but with higher heterogeneity, with low-level cloud features slightly further along the track that are associated with the two calmest of the three SNC sub-classes. The increasing concentration of low-level cloud toward the north-east seen in the WS regime in Figure 5.7c does not feature in the south-east running `B_3` track, however there is increased cloud near the TAM at the north-west end (beginning) of the track.

DISCUSSION

This study has demonstrated the value of using a synoptic climatology over seasons alone to quantify cloud cover over the greater RIS area with Table 5.1 and Figure 5.5 (a) & (b) showing more heterogeneity between the Coggins regimes (Coggins et al., 2014) compared to seasons. However, Table 5.2 and Figure 5.5 (c) & (d) show that a combination of the two approaches explains more variance again.

A spatial analysis of total cloud incidence in Table 5.1 and Table 5.2 shows the southern Ross Sea is cloudier than the RIS with higher spatial (east/west), seasonal, and inter-regime variation. The eastern halves of each sector featured more cloud than the west, however this difference was not as large as the one between the sectors. More cloud was observed during the summer (using both the DJF and the extended DJFMAM definitions), however higher variation (for north/south, east/west, and max/min) was seen during the extended winter (JJASON). Vertical distributions (Fig. 5.5 (c) & (d)) show that cloud height increased during winter for some regimes, consistent with (Adhikari et al., 2012). As cloud formation depends on the presence of moisture, finding more cloud over an ocean than an ice shelf is unsurprising, given that moisture levels in the Antarctic are typically driven by advection (Tietäväinen and Vihma, 2008). Additionally, the geography of the RIS is such that the only routes for moisture advection are from the north (Ross Sea) or the east WAIS in the form of occasional marine air intrusions (Nicolas and Bromwich, 2011). While air flows from the south and west (via the TAM and typically as katabatic flow), it comes from the extremely cold, high, and predominantly dry interior of Antarctica (Tietäväinen and Vihma, 2008; Bromwich et al., 2012). During the traditional winter and spring seasons (spanned by the extended 'winter' season used in this study) the Ross Sea is almost completely covered with sea ice (Parkinson and Cavalieri, 2012), removing a plentiful moisture source with a visible effect on cloud incidence.

The increased cloud incidence in summer relative to winter is consistent with the findings of Adhikari et al. (2012), but contrary to the findings of Verlinden et al. (2011). Both of these studies used the same data as the current study, however they cover different areas and at different scales

with different binning and collation methods. The vertical structure revealed by Figure 5.5 is consistent with the findings of Verlinden et al. (2011) who show distinct boundaries at ~8 km ASL for their 'Antarctic Interior Band' (between 75°S and 83°S) that do not exist for their 'Antarctic Coastal Band' (between 63°S and 75°S), even though the spatial scale is very different. It is worth noting that a low cloud top height in this case is dependent on no cloud existing above it (multiple layers in a single profile are not considered).

The combination of Table 5.2 and Figure 5.5 (c) & (d) shows that the SNC regime is responsible for the highest levels of cloud incidence over the Ross Sea for both extended (6 month) seasons, however most of this cloud is located above 2.5 km ASL (also shown by Figure 5.6 and Figure 5.7a). The RAS regime also features large amounts of cloud over the Ross Sea, however it has a greater effect over the RIS, particularly the western half where it is responsible for the periods of highest cloud incidence. The vertical distribution of the RAS during winter in Figure 5.5c is also seen in the virtual tracks (Fig. 5.7b & Fig. 5.8b), with mid-high level (and almost no low-level) cloud over the RIS combined with a relatively dense low-level cloud feature of the Ross Sea (toward the end of track `A_5`). Both of these regimes are associated with high surface-level southerly winds and strong synoptic-scale pressure gradients (Fig. 5.1 and Coggins et al., 2014) that are theoretically capable of transporting moist air larger distances relative to the WSC and WS regimes with their low wind speeds and more localized mesoscale forcing.

An important feature of the RAS regime is the development of a distinct layer of low-level cloud over the Ross Sea during winter time, visible in the vertical distributions of Figure 5.5c. Due to space and data constraints, summer and winter versions of Figure 5.6 and Figure 5.7 were not created. However both figures still show the layer of low-level cloud with Figure 5.6a suggesting that this occurs near the zonal center of the Ross Sea area, extending toward the east. The tail end of Figure 5.7b includes the eastern portion of the Ross Sea and the low-level cloud can be seen building from approximately 400 km onward. While normally covered by a vast area of sea ice, strong winds in this area associated with RAS events are known to create polynya - areas of open water surrounded by sea ice (Zwally et al., 1985; Bromwich et al., 1993; Drucker et al., 2011). Substantial amounts of heat and moisture are known to be exchanged in these areas leading to the formation of low-level cloud and fog (Andreas et al., 1979; Morales Maqueda et al., 2004; Schnell et al., 1989).

Despite a lower overall cloud incidence over the western half of the RIS, Figure 5.7 and Figure 5.8 both show an increased mean cloud incidence within 150 km of the TAM (situated at the western boundary of the RIS) relative to the rest of the RIS for each of the regimes shown. This cloud is predominantly located above 2.4 km ASL, roughly in line with the upper portion of the TAM, and is likely the result of air parcels from the RIS rising and cooling as they interact with the terrain (Houze, 2014). This effect is most pronounced during a RAS event (Fig. 5.7b & Fig. 5.8b) and is a

likely contributor to the fact that the RAS is responsible for the highest cloud incidence over the western RIS during summer.

The regime with the lowest cloud incidence for all quadrants at all times of year is WSC (Table 5.1 and Table 5.2). While some high-level (low-level) cloud over the eastern RIS (Ross Sea) is visible in Figure 5.6, overall cloud incidence is low. A likely contributor to this is the weak synoptic pressure gradient causing lower mean wind speeds in a generally south-westerly direction over the RIS (see Figure 5.1), where the majority of the air over the study area likely originated from the very dry interior of the continent. The WSC regime also tends to occur during winter and spring when sea ice cover is more extensive.

It is interesting to note that the WS regime, which features the lowest mean wind speeds and smallest synoptic pressure gradient (Coggins et al., 2014, Fig. 5.1 and), is responsible for higher cloud incidence over the study area than WSC. As shown by Figure 5.5, Figure 5.6, Figure 5.7c, and Figure 5.8c, the majority of cloud during the WS regime is very low-level with some mid-level occurring over the Ross Sea and near the TAM. A possible explanation for the presence of low-level cloud is radiation fog (Brown and Roach, 1976; Duynkerke, 1991; Houze, 2014), where air is radiatively cooled near the surface - a very common occurrence under low wind conditions in Antarctica (Savage and Stearns, 1985; Parish and Bromwich, 1986) - until the dew point is reached and fog forms. A similar vertical distribution can be seen for the WNC regime over the RIS (Fig. 5.6b, Fig. 5.5c, & Fig. 5.5d) which is unsurprising given the similar conditions experience over the RIS during both regimes (Fig. 5.1 (a), (e), (f), & (j)).

A factor to consider when addressing very low-level cloud is that it may be underestimated by the 2B-GEOPROF-LIDAR product, specifically when higher level cloud obscures the low-level cloud from the CALIOP sensor of CALIPSO while ground clutter confuses the lowest levels of the CloudSat radar returns. However, this is unlikely to have had a major impact on this study as the cloud has to be very low (<~1 km - Marchand et al., 2008) to be missed by CloudSat. The Coggins regimes that do not show a substantial or discrete low-level cloud signature show typically stronger winds over the study area which implies that the boundary layer air will be well-mixed via turbulent processes. Therefore lower-level cloud is more likely to be spread across a larger range of vertical levels and would be captured by CloudSat, as opposed to a fog-like clouds which are unlikely to form near sea-level under higher wind conditions. If there was consistent under-detection there would be a substantial (probably step-like) decrease from the ~1 km AGL level down, however this is not seen in any of the vertical distributions.

One point that is clear from all the results presented is that periods of strong synoptic forcing are associated with greater cloud incidence. While this effect is greater at mid- to high-levels within the troposphere, there are still substantial levels of low cloud over the Ross Sea during RAS regimes. The relative MSLP fields in Figure 5.1(f-j) show the presence of relatively deep

low pressure systems to the north and east of the RIS for the SNC and WSC (strongly forced) classes respectively. It is likely that much of the mid-to-high level cloud seen over the east of the Ross Sea and RIS is frontal cloud from these systems, in the case of the RIS it has likely traveled over the western tip of the WAIS. It is very likely that much of the cloud seen over the Ross Sea is at least linked to the Ross Ice Shelf Polynya during these strong forcing events, where the increased speeds of the southerly winds are known to create and expand or maintain the polynya (Zwally et al., 1985; Bromwich et al., 1993; Drucker et al., 2011) and the association of cloud in the lower troposphere is well-associated with polynya (Morales Maqueda et al., 2004, provide a good review). The surface-level cloud seen during the RAS regime over the Ross Sea lends weight to this theory.

CONCLUSIONS

This study has quantified cloud incidence over the RIS and southern Ross Sea in three dimensions using four years and ten months of CloudSat/CALIPSO combined data. It has shown that an analysis based on regimes derived from physical processes yields more useful information than a simple seasonal analysis, however the most useful results were produced using a combination of regimes and seasons. The highest cloud incidence was found over the eastern Ross Sea quadrant during the extended six-month 'summer' season definition, while the lowest cloud incidence was seen over the western halves of both the RIS and Ross Sea sectors during the extended six-month 'winter' season. A direct link was shown between strong synoptic forcing and greater incidence of high-level cloud, while calmer periods produced a greater incidence of low-level cloud. The cloud incidence maxima were largely controlled by a regime linked to a strong cyclone to the north in the Ross Sea for most cases, however RAS events were the biggest controlling factor during winter over the RIS. Cloud incidence minima, both including and excluding any seasonal component, were shown to occur during a regime with moderate synoptic forcing and wind speed. The mean wind and MSLP fields for this regime show the majority of air over the study area has likely originated from the Antarctic interior and is therefore cold and dry, with the presence of a marine air intrusion unlikely due to weaker synoptic forcing. The tendency for greater cloud levels to the east reflects the role that moisture transport plays in cloud formation in this area, where most southward (moist marine) air movement occurs to the east with northward (dry interior) air movement occurring to the west. The Ross Ice Shelf Polynya likely plays a significant role by contributing large amounts of heat and moisture to the atmosphere along the northern edge of the RIS during winter and spring - times when the open ocean is otherwise covered by sea ice for hundreds to thousands of kilometers from the RIS - however this was not quantifiable. Despite the lower cloud incidence to the west of the sector, there is a strong and persistent cloud signature

associated with the TAM over the RIS. This was particularly pronounced during RAS events, with very a very thick layer of high mean cloud incidence within 150 km of the mountains.

6

CONCLUSIONS AND FUTURE WORK

The aim of this thesis was *to investigate local-scale meteorology near Ross Island and explore connections with larger scale atmospheric processes*. To achieve this, four objectives were defined to guide research work and technical development with each forming the basis of a single chapter in this document:

1. to further development of the SNOWWEB system of weather stations, such that they may be deployed over a large area with good wireless communication (Chapter 2);
2. to use SNOWWEB to investigate surface-level conditions in the complex terrain near Ross Island (Chapter 3);
3. to validate the finest model grid output of AMPS using high resolution observational datasets created by SNOWWEB deployments (Chapter 4);
4. and to determine three-dimensional cloud structure over the RIS during given surface conditions so as to better understand the weather as experienced on the ground (Chapter 5).

The aim of the SNOWWEB project, central to the weather stations used in the research presented, was to create a weather station with a low component cost that nevertheless acquired a set of specific observations comparable with much larger, more complicated, and more expensive automatic weather stations (AWSs) (see Chapter 2). The reasoning behind this aim was to build a network of many less expensive weather stations that could be deployed in and around existing but sparse AWS networks. In order to achieve it certain compromises were necessary, the biggest being that the new stations would not be designed for permanent deployment. This was partly a logistical consideration, where supplying sufficient battery reserves to power the stations through the dark Antarctic winter would at least double or treble their weight and make it harder to deploy large numbers of them, but also allowed the use of less-robust instrumentation that did not need to withstand years of continuous abuse with little maintenance at mercy of Antarctic weather. The final SNOWWEB weather station (SWS) sensor package includes cup anemometers and simple potentiometer-based wind vanes for wind speed/direction observations. A silicon-based on-chip temperature (band-gap) and humidity (capacitive) sensor was used within a commercial stacked-

plate radiation shield, while a piezo-resistive on-chip pressure sensor was housed in the electronic enclosure. These sensors were found to equate well with much more expensive sensors on nearby University of Wisconsin-Madison Antarctic automatic weather station (UWAAWS) in chapters 3 and 4, though required individual lab-based calibration to account for DC offsets.

The final result of this technical development was a set of twenty fully functional SWS able to record and transmit observations at relatively high frequency (adjustable up to 1 Hz) reliably during the summer months. There was a failure on the part of antenna selection, where the extremely poor conductivity of the deep snow the stations were deployed on provided an inadequate ground-plane for the monopole omni-directional antennae used. While not quantifiable in the field, this would have greatly distorted the antennae beams which would explain some of the networking anomalies seen - especially some very long transmission distances from stations on the ice shelf to stations located on hard ground (with a good ground plane and thus a better-performing antenna) that otherwise did not make sense. This problem was very likely responsible for the communications failures during the final deployment in Chapter 4 despite the system working in New Zealand beforehand. A simple solution is to use dipole antennae instead as this will be much simpler than attempting to install a sufficient earthing system, this will be incorporated into future designs.

Chapter 3 investigated surface-level conditions in the complex terrain near Ross Island using output from the first (scientifically) successful deployment of the SWS system outlined in Chapter 2. Fourteen SWS were placed to the west and north of White Island and results confirmed the compromises in physical design did not substantially impact the ability of SWS to successfully observe surface wind, temperature, and pressure conditions during summer, where correlations between the SWS and a nearby UWAAWS were very good. This chapter introduced the use of the synoptic-scale 'Coggins regimes' (Coggins et al., 2014) - a set of weather regimes derived using k-means clustering on 33 years of ERA Interim reanalysis data on 10 m winds - to gain a wider perspective. These worked very well to identify the RAS event covered by the majority of the chapter. Local observed wind speeds at the beginning of the RAS matched with expectations, increasing steadily until some stations showed a (10 minute mean) peak of nearly 20 ms^{-1}. Observed temperatures also steadily rose, while the diurnal cycle was very much diminished. This was likely due to increased turbulent mixing caused by the high wind speed, though results from a later chapter (5) imply that cloud was likely also present with the associated temporally consistent down-welling longwave radiation helping to heat the surface and partially suppress the cycle. Spatial variability of wind speeds over the SWS network was high and itself very variable, illustrating the complexity of surface flows in the area.

The latter portion of the RAS event identified by the Coggins regimes featured a lull in surface winds over the SWS network that was not observed over the wider UWAAWS network, however a

short burst of high wind speeds for some of the SWS marked an interesting phenomenon. Over the period of a few hours, wind speeds for some of the western stations almost trebled while those on the northern portion of the network only saw a slight increase. There was a corresponding temporary decrease in station pressure for those stations that saw the spike in wind speed, while the stations that saw only a small increase in wind speed saw an increase in surface pressure. The single UWAAWS station in the area (Pegasus North) agreed with the SWS observations, while a UWAAWS further out onto the RIS (Lorne) showed no obvious similarities beyond a general increase in station pressure over the entire period. The spike in wind speeds is consistent with a gap wind between White Island and Black Island and was substantial enough to potentially cause blowing snow at Pegasus Airfield and disrupt air operations. Chapter 3 also compared SWS and UWAAWS observations with output from the Antarctic Mesoscale Prediction System (AMPS) domain 5 (1.1 km grid spacing), with generally good agreement between the model and observations. Two areas of difference, however, were the suppression of the diurnal cycle in the observations and the observed gap wind, neither of which were represented within AMPS. Both of these faults may be linked to local-scale processes and were likely caused by problems with AMPS' representation of the boundary layer; it is likely that poor initial conditions played some role in this.

Chapter 4 (accepted as a paper by Monthly Weather Review at time of writing - Jolly et al., 2016) utilized observations from another SNOWWEB deployment (15 SWS located to the east of Ross Island and White Island) to validate domain 5 of AMPS over the 2014/15 summer season. 'Virtual stations' were created from the AMPS output by selecting the nearest model grid point to each physical SWS location before both datasets were used to train the same self-organizing map (SOM) - an unusual step compared to most documented approaches that use either model output *or* observations not both. The resulting SOM classes were representative of both the SWS and AMPS input datasets, making them less reliable as a definitive climatology, however developing a climatology was not the aim of the chapter as the time period was too short (two months). Instead, this allowed a direct comparison of SOM classification time-series and statistics between the observations and the model. The resulting analysis showed that representation of surface-level winds within AMPS was poor during light wind conditions when synoptic-scale forcing was weak. However, the Polar Weather Research and Forecasting (WRF) model within AMPS did accurately predict the occurrence of the low wind *periods* well and these showed good temporal alignment with the synoptic-scale Coggins regimes, meaning that resolution of localized forcing during periods of low winds and weak synoptic forcing may be poor near areas of complex terrain. Insufficient resolution of available model initialization data, along with model grid length were possible contributors given the complex nature of the topography in this region, though cloud and associated impacts on the local radiation budget are also known problem areas for numerical weather prediction (NWP) models in Antarctica

Temperature, wind, and pressure correlations between SWS observations and AMPS output tended to increase with wind speed, where the highest wind speed class (identified as a RAS event) was also the best performing. SOM classes with a high frequency of occurrence and/or a high persistence (median duration) also tended to score more highly than neighboring (similar) classes. This highlighted a potential issue around the timing of events within AMPS, where classes that were not frequent or persistent were less likely to align in time between the two datasets. Analyzing the SOM classifications with respect to the Coggins regimes suggested that the strength and location of cyclones in the Ross Sea may be poorly resolved by the Polar WRF model within the AMPS operational system in some cases, however further investigation is needed. The regimes helped to confirm the highest wind speed SOM class as a RAS event and generally provided useful input.

Chapter 3 and Chapter 4 both highlight the utility of SNOWWEB when SWS are deployed intelligently near existing UWAAWS. While initially a very useful validation source for the SWS observations, the integration of observations from both networks provide both high resolution data from target areas as well as overall information about the wider area and specific common areas of interest such as Pegasus Airfield of Windless Bight. The UWAAWS network also contains observations spanning many years, potentially allowing further extrapolation from seasonal deployments of SNOWWEB if carried out appropriately. Future SNOWWEB deployments are planning to further leverage this integrated approach as opposed to treating the networks independently, with areas of interest near the Siple Coast already highlighted.

Finally, Chapter 5 quantified cloud incidence in three dimensions over the RIS and southern Ross Sea using the 2B-GEOPROF-LIDAR dataset constructed from observations from the CloudSat and CALIPSO satellites. While this dataset was well-known and applied over Antarctica before at a seasonal level, this study was the first to focus on the RIS and Ross Sea using regimes derived from physical processes (the Coggins regimes). Despite the fact that the Coggins regimes were derived using surface winds, they were found to be applicable to clouds throughout the troposphere and explained much more variance than a typical seasonal analysis. The highest levels of cloud incidence primarily occurred during SNC regimes, when a strong cyclone was present in the northern Ross Sea, however the RAS regime was the dominant contributor over the western RIS. Cloud present during both of these regimes tended to be above 2.5 km ASL. The regime with the weakest winds (WS) was not the least cloudy, thanks largely to a substantial amount of low-level cloud, with the least cloudy regime being WSC. This regime features some synoptic forcing but likely not enough to draw moisture over the WAIS. Additionally, mean wind directions indicate that most of the air over the RIS and Ross Sea likely originated from the cold and dry Antarctic interior thus moisture content was probably low.

When the Coggins regimes were further divided by binary 'summer' (DJFMAM) and 'winter' (JJASON) seasons (as defined by sea ice extent), more variability was explained again. The extended summer season showed the highest levels of cloud incidence, however while winter levels showed the lowest cloud incidence there was a larger difference between the minimum and maximum cloud incidences for each sector. The six-month seasons were chosen to coincide with below/above (summer/winter) the yearly average sea ice extent as advection has been shown to be the driving force behind the atmospheric moisture budget in Antarctica. Cloud incidence over the western RIS was now high during the SNC regime for the summer months, however this reverted back to the RAS regime during winter. The WSC regime was still responsible for the lowest cloud incidence. Vertical distributions also displayed some seasonality, with mid- high-level cloud maxima increasing in height during winter. Additionally, a local maximum cloud incidence at ~0.5 km appeared over the Ross Sea for the RAS regime during winter which was very likely linked to the development of the Ross Ice Shelf Polynya - an area of ice-free open water at the edge of the RIS created by high speed surface-level southerly winds. When viewing cloud incidence along 'virtual tracks' (created from multiple approximately co-located passes) it was possible to see a high incidence of very low-level cloud over the Ross Sea during RAS events, even though these tracks were not divided by season, which shows the strength of that signal. The virtual tracks also showed a persistent mid- to high-level cloud signature against the TAM (western RIS) which was most pronounced during the RAS regime. Some caution is required with the CloudSat/CALIPSO product when thick cloud is present at mid- to high altitudes as very low-level cloud can be missed (occluded from the CALIPSO lidar by high cloud and hidden in ground clutter from the CloudSat radar), however this is unlikely to have had a substantial impact on this study.

The technique of applying a SOM to a combined dataset for validation purposes - used in Chapter 4 - worked very well and is widely applicable. The analysis of observations from CloudSat and CALIPSO presented in Chapter 5 provided new information about cloud incidence over the RIS with relation to surface wind patterns. A logical progression of this research is to expand the scope to cover the entire Ross Sea as well, then use the result as a validation set for AMPS output. In addition to comparing satellite observations to model output using Coggins regimes and seasons, this presents a good opportunity to use the combined SOM technique on cloud data to validate historical AMPS output. Comparing the resulting SOMs with Coggins regimes could provide further information on the connection between surface processes and tropospheric clouds over the RIS. With or without input from SOMs, spatial cloud information for passive sensors such as MODIS and MISR or the International Satellite Cloud Climatology Project (ISCCP) analysis could help to further enhance the CloudSat and CALIPSO observations with an improved horizontal perspective in future studies, however some difficulties still remain in the process of extracting reliable cloud masks over ice and snow. There is an increasing focus on clouds over Antarctica and the Southern Ocean, with the Atmospheric Radiation Measurement: West Antarctic Radiation

Experiment (AWARE) project in particular providing extremely valuable observations from Ross Island and a mobile facility on the WAIS that can be incorporated into future studies as well.

This thesis has documented the development of the 'SNOWWEB' network of weather stations in Chapter 2 and presented analyses of high density meteorological observations from two successful summer field seasons in Antarctica (chapters 3 & 4), proving it is possible to build low-cost, easily deployable weather stations that can withstand Antarctic conditions. To properly investigate surface-level conditions near Ross Island, observations from nearby UWAAWSs were incorporated into the dataset produced by the SWS network as both a validation source and to gain larger scale context. For additional help with synoptic-scale context, Coggins regimes were used to classify surface winds from ERA Interim. This proved to be a largely successful dataset despite differences in spatial and temporal scales. Results from these surface-level investigations are presented in Chapter 3 and Chapter 4. Both chapters also incorporate comparisons with output from AMPS, with Chapter 4 performing a proper validation study. Finally, in an effort to discover more about the atmosphere over the wider RIS region, further analysis of nearly five years of satellite observations from CloudSat and CALIPSO quantified cloud incidence over the RIS and southern Ross Sea in Chapter 5.

The key science findings from this work are: that the complex terrain near Ross Island produces complicated interactions that can be difficult for the Polar WRF model to forecast, especially when large-scale forcing (and wind speed) is low and localized forcing has a larger impact; that dense observational networks provide very valuable data in areas with complicated flows, and that these spatially dense observations are extremely helpful when attempting to validate model output with a fine grid spacing; that cloud formation over the RIS appears to be sensitive to moisture transport, with more cloud during summer and autumn when the sea ice extent is below average; that periods of high winds and intense synoptic forcing result in more cloud over the RIS, with a link to the RAS low-level air stream, but that periods of minimal forcing still result in substantial cloud incidence at low altitudes; that there is a link between the RAS and low-level cloud over the Ross Sea during winter when sea ice is present, with the Ross Ice Shelf Polynya a likely contributor of moisture.

BIBLIOGRAPHY

Adhikari, L., Wang, Z., and Deng, M. Seasonal variations of Antarctic clouds observed by CloudSat and CALIPSO satellites. *Journal of Geophysical Research Atmospheres*, 117(4):1–17, 2012. ISSN 01480227. doi: 10.1029/2011JD016719.

Andreas, E. L., Paulson, C. A., William, R. M., Lindsay, R. W., and Businger, J. A. The turbulent heat flux from arctic leads. *Boundary-Layer Meteorology*, 17(1):57–91, 1979. ISSN 00068314. doi: 10.1007/BF00121937.

Andreas, E. L. and Cash, B. a. Convective heat transfer over wintertime leads and polynyas. *Journal of Geophysical Research*, 104(C11):25721, 1999. ISSN 0148-0227. doi: 10.1029/1999JC900241.

Ball, F. K. Winds on the Ice Slopes of Antarctica. In *Antarctic Meterology: Proceedings of the Symposium*, pages 9–16, Melbourne, 1960. Pergamon Press Ltd.

Barrenetxea, G., Ingelrest, F., Schaefer, G., Vetterli, M., Couach, O., and Parlange, M. Sensorscope: Out-of-the-box environmental monitoring. In *Information Processing in Sensor Networks, 2008. IPSN'08. International Conference on*, pages 332–343. IEEE, 2008. doi: 10.1109/IPSN.2008.28.

Bauguitte, S. J., Brough, N., Frey, M. M., Jones, A. E., Roscoe, H. K., and Wolff, E. W. A network of autonomous surface ozone monitors in Antarctica: technical description and first results. In *AGU Fall Meeting Abstracts*, volume 1, page 126, 2009.

Bosch Sensortec. BMP 085 Digital Pressure Sensor Datasheet. Technical report, Bosch Sensortec, 2009.

Bracegirdle, T. J. Climatology and recent increase of westerly winds over the Amundsen Sea derived from six reanalyses. *International Journal of Climatology*, 33(4):843–851, 2013. ISSN 08998418. doi: 10.1002/joc.3473.

Breckenridge, C. J., Radok, U., Stearns, C. R., and Bromwich, D. H. Katabatic winds along the Transantarctic Mountains. In Stearns, C. R. and Bromwich, D., editors, *Antarctic Meteorology and Climatology: Studies Based on Automatic Weather Stations*, pages 69–92. American Geophysical Union, 1993. doi: 10.1029/AR061p0069. URL http://www.agu.org/books/ar/v061/AR061p0069/AR061p0069.shtml.

Bromwich, D. H. A satellite study of barrier-wind airflow around Ross Island. *Antarctic Journal of the US*, 23:167–169, 1988.

Bromwich, D. H., Du, Y., and Parish, T. R. Numerical simulation of winter katabatic winds from West Antarctica crossing Siple Coast and the Ross Ice Shelf. *Monthly weather review*, 122(7): 1417–1435, 1994.

Bromwich, D. H., Steinhoff, D. F., Simmonds, I., Keay, K., and Fogt, R. L. Climatological aspects of cyclogenesis near Adélie Land Antarctica. *Tellus A*, 63(5):921–938, 2011.

Bromwich, D. H. Satellite analyses of Antarctic katabatic wind behavior. *Bulletin of the American meteorological society*, 70(7):738–749, 1989.

Bromwich, D. H. and Liu, Z. An observational study of the katabatic wind confluence zone near Siple Coast, West Antarctica. *Monthly weather review*, 124(3):462–477, 1996.

Bromwich, D. H., Carrasco, J. F., and Stearns, C. R. Satellite Observations of Katabatic-Wind Propagation for Great Distances across the Ross Ice Shelf. *Monthly weather review*, 120(9):1940–1949, 1992.

Bromwich, D. H., Carrasco, J. F., Liu, Z., and Tzeng, R.-Y. Hemispheric atmospheric variations and oceanographic impacts associated with katabatic surges across the Ross ice shelf, Antarctica. *Journal of Geophysical Research*, 98:13045, 1993. ISSN 0148-0227. doi: 10.1029/93JD00562.

Bromwich, D. H., Monaghan, A. J., Manning, K. W., and Powers, J. G. Real-Time Forecasting for the Antarctic: An Evaluation of the Antarctic Mesoscale Prediction System (AMPS)*. *Monthly Weather Review*, 133(3):579–603, 2005. ISSN 0027-0644. doi: 10.1175/MWR-2881.1.

Bromwich, D. H., Nicolas, J. P., Hines, K. M., Kay, J. E., Key, E. L., Lazzara, M. A., Lubin, D., McFarquhar, G. M., Gorodetskaya, I. V., Grosvenor, D. P., and Others. Tropospheric clouds in Antarctica. *Reviews of Geophysics*, 50(1), 2012. doi: 10.1029/2011RG000363.

Bromwich, D. H., Otieno, F. O., Hines, K. M., Manning, K. W., and Shilo, E. Comprehensive evaluation of polar weather research and forecasting model performance in the Antarctic. *Journal of Geophysical Research: Atmospheres*, 2013.

Brown, R. and Roach, W. T. The physics of radiation fog II - a numerical study. *Quarterly Journal of the Royal Meteorological Society*, 102(432):335–354, apr 1976. ISSN 00359009. doi: 10.1002/qj.49710243205. URL http://doi.wiley.com/10.1002/qj.49710243205.

Cassano, E. N., Glisan, J. M., Cassano, J. J., Gutowski Jr, W. J., and Seefeldt, M. W. Self-organizing map analysis of widespread temperature extremes in Alaska and Canada. *CLIMATE RESEARCH*, 62(3):199–218, 2015.

Chan, M. A. and Comiso, J. C. Cloud features detected by MODIS but not by CloudSat and CALIOP. *Geophysical Research Letters*, 38(24):1–8, 2011. ISSN 00948276. doi: 10.1029/2011GL050063.

Chenoli, S. N., Turner, J., and Samah, A. A. A climatology of strong wind events at McMurdo station, Antarctica. *International Journal of Climatology*, 2012.

Chenoli, S. N., Turner, J., and Samah, A. A. A Strong Wind Event on the Ross Ice Shelf, Antarctica: A Case Study of Scale Interactions. *Monthly Weather Review*, 143(10):4163–4180, 2015. ISSN 0027-0644. doi: 10.1175/MWR-D-15-0002.1. URL http://journals.ametsoc.org/doi/abs/10.1175/MWR-D-15-0002.1.

Chubb, T. H., Jensen, J. B., Siems, S. T., and Manton, M. J. In situ observations of supercooled liquid clouds over the Southern Ocean during the HIAPER Pole-to-Pole Observation campaigns. *Geophysical Research Letters*, 40(19):5280–5285, 2013. ISSN 00948276. doi: 10.1002/grl.50986.

Coggins, J. H. J., McDonald, A. J., Plank, G., Pannell, M., Jolly, B., Parsons, S., and Delany, T. SNOW-WEB: a new technology for Antarctic meteorological monitoring. *Antarctic Science*, 25 (04):583–599, 2013. ISSN 1365-2079. doi: 10.1017/S0954102013000011. URL http://journals.cambridge.org/article{_}S0954102013000011.

Coggins, J. H. J. and McDonald, A. J. The influence of the Amundsen Sea Low on the winds in the Ross Sea and surroundings: Insights from a synoptic climatology. *Journal of Geophysical Research: Atmospheres*, 120(6):2167–2189, 2015.

Coggins, J. H. J., McDonald, A. J., and Jolly, B. Synoptic climatology of the Ross Ice Shelf and Ross Sea region of Antarctica: k-means clustering and validation. *International Journal of Climatology*, 2014. doi: doi:10.1002/joc.3842.

Comiso, J. and Stock, L. Studies of Antarctic cloud cover variability from 1982 through 1999. In *IGARSS 2001. Scanning the Present and Resolving the Future. Proceedings. IEEE 2001 International Geoscience and Remote Sensing Symposium (Cat. No.01CH37217)*, volume 4, pages 1782–1785, 2001. ISBN 0-7803-7031-7. doi: 10.1109/IGARSS.2001.977070. URL http://ieeexplore.ieee.org/lpdocs/epic03/wrapper.htm?arnumber=977070.

Connolley, W. M. The Antarctic temperature inversion. *International Journal of Climatology*, 16(12): 1333–1342, 1996.

Corke, P., Wark, T., Jurdak, R., Hu, W., Valencia, P., and Moore, D. Environmental wireless sensor networks. *Proceedings of the IEEE*, 98(11):1903–1917, 2010.

Corporation, A. ATmega128/L Datasheet, jun 2011.

Dee, D. P., Uppala, S. M., Simmons, A. J., Berrisford, P., Poli, P., Kobayashi, S., Andrae, U., Balmaseda, M. A., Balsamo, G., Bauer, P., Bechtold, P., Beljaars, A. C. M., van de Berg, L., Bidlot, J., Bormann, N., Delsol, C., Dragani, R., Fuentes, M., Geer, A. J., Haimberger, L., Healy, S. B., Hersbach, H., Hólm, E. V., Isaksen, L., Kållberg, P., Köhler, M., Matricardi, M., McNally, A. P., Monge-Sanz, B. M., Morcrette, J.-J., Park, B.-K., Peubey, C., de Rosnay, P., Tavolato, C., Thépaut,

J.-N., and Vitart, F. The ERA-Interim reanalysis: Configuration and performance of the data assimilation system. *Quarterly Journal of the Royal Meteorological Society*, 137(656):553–597, 2011. ISSN 00359009. doi: 10.1002/qj.828.

Dethleff, D. Polynyas as a Possible Source for Enigmatic Bennett Island Atmospheric Plumes. *Washington DC American Geophysical Union Geophysical Monograph Series*, 85:475–483, 1994. doi: 10.1029/GM085p0475.

Drucker, R., Martin, S., and Kwok, R. Sea ice production and export from coastal polynyas in the Weddell and Ross Seas. *Geophysical Research Letters*, 38(17), 2011.

Duynkerke, P. G. Radiation Fog: A Comparison of Model Simulation with Detailed Observations, 1991. ISSN 0027-0644. URL http://journals.ametsoc.org/doi/abs/10.1175/1520-0493(1991)119{%}3C0324:RFACOM{%}3E2.0.CO;2.

Fogt, R. L. and Bromwich, D. H. Atmospheric Moisture and Cloud Cover Characteristics Forecast by AMPS*. *Weather and Forecasting*, 23(Mmm):914–930, 2008. ISSN 0882-8156. doi: 10.1175/2008WAF2006100.1.

Frey, R. A., Ackerman, S. A., Liu, Y., Strabala, K. I., Zhang, H., Key, J. R., and Wang, X. Cloud detection with MODIS. Part I: Improvements in the MODIS cloud mask for Collection 5. *Journal of Atmospheric and Oceanic Technology*, 25(7):1057–1072, 2008. ISSN 07390572. doi: 10.1175/2008JTECHA1052.1.

Gaberšek, S. and Durran, D. R. Gap Flows through Idealized Topography. Part I: Forcing by Large-Scale Winds in the Nonrotating Limit. *Journal of the Atmospheric Sciences*, 61(23):2846–2862, 2004. ISSN 0022-4928. doi: 10.1175/JAS-3340.1.

Genthon, C., Six, D., Favier, V., Lazzara, M., and Keller, L. Atmospheric temperature measurements biases on the Antarctic plateau. *Journal of Atmospheric and Oceanic Technology*, 2011.

Guo, Z., Bromwich, D. H., and Cassano, J. J. Evaluation of Polar MM5 simulations of Antarctic atmospheric circulation. *Monthly Weather Review*, 131(2):384–411, 2003.

Hart, J. K. and Martinez, K. Environmental Sensor Networks: A revolution in the earth system science? *Earth-Science Reviews*, 78(3):177–191, 2006.

Haynes, J. M., Jakob, C., Rossow, W. B., Tselioudis, G., and Brown, J. B. Major characteristics of Southern Ocean cloud regimes and their effects on the energy budget. *Journal of Climate*, 24(19):5061–5080, 2011. ISSN 08948755. doi: 10.1175/2011JCLI4052.1.

Hewitson, B. C. and Crane, R. G. Self-organizing maps: applications to synoptic climatology. *Climate Research*, 22(1):13–26, 2002.

Holmes, R. E., Stearns, C. R., Weidner, G. A., and Keller, L. M. Utilization of automatic weather station data for forecasting high wind speeds at Pegasus Runway, Antarctica. *Weather and forecasting*, 15(2):137–151, 2000.

Hoskins, B. J. and Hodges, K. I. A new perspective on Southern Hemisphere storm tracks. *Journal of Climate*, 18(20), 2005.

Houze, R. A. *Cloud Dynamics*. Academic Press, second edition, 2014. ISBN 9780123742667.

IEEE. IEEE Standard for Local and metropolitan area networks – Part 15.4: Low Rate Wireless Personal Area Networks (LR-WPANs). *IEEE Std 802.15.4-2011 (Revision of IEEE Std 802.15.4-2006)*, jun 2011. doi: 10.1109/IEEESTD.2011.6012487.

Inc, D. I. XBee/XBee-PRO ZB RF Modules, 2010.

Jackson, P. and Steyn, D. Gap winds in a fjord. Part I: Observations and numerical simulation., 1994.

James, I. N. The Antarctic drainage flow: implications for hemispheric flow on the Southern Hemisphere. *Antarctic Science*, 1(03):279–290, 1989. ISSN 0954-1020. doi: 10.1017/S0954102089000404. URL http://www.journals.cambridge.org/abstract{_}S0954102089000404.

Jolly, B., Willig, A., McDonald, A., Pannell, M., and Plank, G. SNOWWEB - Wirelessly Connected Weather Stations in Antarctica. In *Eighth IEEE Workshop on Practical Issues in Building Sensor Network Applications 2013 (IEEE SenseApp 2013)*, Sydney, Australia, oct 2013.

Jolly, B., McDonald, A. J., Coggins, J. H. J., Cassano, J., Lazzara, M., Zawar-Reza, P., Graham, G., Plank, G., Petterson, O., and Dale, E. A validation of the Antarctic Mesoscale Prediction System using Self-Organizing Maps and high density observations from SNOWWEB. *Monthly Weather Review - accepted but not yet published*, 2016.

Juang, P., Oki, H., Wang, Y., Martonosi, M., Peh, L.-S., and Rubenstein, D. Energy-Efficient Computing for Wildlife Tracking: Design Tradeoffs and Early Experiences with ZebraNet. In *Proc. 10th International Conference on Architectural Support for Programming Languages and Operating Systems*, San Jose, CA, oct 2002.

King, J. C. and Turner, J. *Antarctic Meteorology and Climatology*. Cambridge University Press, Cambridge, 1997. ISBN 9780511524967. doi: 10.1017/CBO9780511524967. URL http://ebooks.cambridge.org/ref/id/CBO9780511524967.

Kohonen, T. The Self-Organizing Map. *Proceedings of the IEEE*, 78(9):1464–1480, 1990.

Korolev, A. V., Isaac, G. A., Cober, S. G., Strapp, J. W., and Hallett, J. Microphysical characterization of mixed-phase clouds. *Q. J. Roy. Meteor. Soc.*, 129(587):39–65, 2003. ISSN 1477870X. doi: 10.1256/gj.01.204.

Lachlan-Cope, T. Antarctic clouds. *Polar Research*, 29(2):150–158, 2010. ISSN 08000395. doi: 10.1111/j.1751-8369.2010.00148.x.

Lawson, R. P. and Gettelman, A. Impact of Antarctic mixed-phase clouds on climate. *Proceedings of the National Academy of Sciences of the United States of America*, 111(51):18156–61, 2014. ISSN 1091-6490. doi: 10.1073/pnas.1418197111. URL http://www.ncbi.nlm.nih.gov/pubmed/25489069.

Lazzara, M. A., Weidner, G. A., Keller, L. M., Thom, J. E., and Cassano, J. J. Antarctic Automatic Weather Station Program: 30 Years of Polar Observation. *Bulletin of the American Meteorological Society*, 93(10):1519–1537, 2012.

Liu, X., Chen, H., Wang, M., and Chen, S. An XBee-Pro based energy monitoring system. In *Telecommunication Networks and Applications Conference (ATNAC), 2012 Australasian*, pages 1–6. IEEE, 2012.

Liu, Z., Vaughan, M., Winker, D., Kittaka, C., Getzewich, B., Kuehn, R., Omar, A., Powell, K., Trepte, C., and Hostetler, C. The CALIPSO lidar cloud and aerosol discrimination: Version 2 algorithm and initial assessment of performance. *Journal of Atmospheric and Oceanic Technology*, 26(7):1198–1213, 2009. ISSN 07390572. doi: 10.1175/2009JTECHA1229.1.

Lüpkes, C., Vihma, T., Bimbaum, G., and Wacker, U. Influence of leads in sea ice on the temperature of the atmospheric boundary layer during polar night. *Geophysical Research Letters*, 35(3):2–6, 2008. ISSN 00948276. doi: 10.1029/2007GL032461.

Mace, G. G. and Zhang, Q. The CloudSat radar-lidar geometrical profile product (RL-GeoProf): Updates, improvements, and selected results. *Journal of Geophysical Research: Atmospheres*, 119(15):9441–9462, 2014. ISSN 21698996. doi: 10.1002/2013JD021374.

Mace, G. G., Zhang, Q., Vaughan, M., Marchand, R., Stephens, G., Trepte, C., and Winker, D. A description of hydrometeor layer occurrence statistics derived from the first year of merged Cloudsat and CALIPSO data. *Journal of Geophysical Research Atmospheres*, 114(8):1–17, 2009. ISSN 01480227. doi: 10.1029/2007JD009755.

Manning, K. W. AMPS Configuration, 2015. URL http://www2.mmm.ucar.edu/rt/amps/information/configuration/configuration.html.

Marchand, R., Mace, G. G., Ackerman, T., and Stephens, G. Hydrometeor Detection Using Cloudsat - An Earth-Orbiting 94-GHz Cloud Radar. *Journal of Atmospheric and Oceanic Technology*, 25:519–533, 2008. doi: 10.1175/2007JTECHA1006.1.

Martinez, K., Ong, R., and Hart, J. Glacsweb: a sensor network for hostile environments. In *Sensor and Ad Hoc Communications and Networks, 2004. IEEE SECON 2004. 2004 First Annual IEEE Communications Society Conference on*, pages 81–87. IEEE, 2004.

Martinez, K., Padhy, P., Elsaify, A., Zou, G., Riddoch, A., Hart, J. K., and Ong, H. L. R. Deploying a sensor network in an extreme environment. In *Sensor Networks, Ubiquitous, and Trustworthy Computing, 2006. IEEE International Conference on*, volume 1, pages 8—-pp. IEEE, 2006.

McClelland, I. Inquiry AO-2013-009: RNZAF Boeing 757, NZ7571, landing below published minima. Technical report, Transport Accident Investigation Commission, Wellington, NZ, 2014.

Meyers, M. P., DeMott, P. J., and Cotton, W. R. New Primary Ice-Nucleation Parameterizations in an Explicit Cloud Model, 1992. ISSN 08948763.

Monaghan, A. J., Bromwich, D. H., Powers, J. G., and Manning, K. W. The climate of the McMurdo, Antarctica, region as represented by one year of forecasts from the Antarctic Mesoscale Prediction System*. *Journal of Climate*, 18:1174–1189, apr 2005.

Morales Maqueda, M. A., Willmott, A. J., and Biggs, N. R. T. Polynya dynamics: A review of observations and modeling. *Reviews of Geophysics*, 42(1), 2004.

Morley, B. M., Uthe, E. E., and Viezee, W. Airborne lidar observations of clouds in the Antarctic troposphere. *Geophysical Research Letters*, 16(6):491–494, 1989. doi: 10.1029/GL016i006p00491.

Naud, C. M., Booth, J. F., and Del Genio, A. D. Evaluation of ERA-Interim and MERRA cloudiness in the southern ocean. *Journal of Climate*, 27(5):2109–2124, 2014. ISSN 08948755. doi: 10.1175/JCLI-D-13-00432.1.

Nicolas, J. P. and Bromwich, D. H. Climate of West Antarctica and Influence of Marine Air Intrusions*. *Journal of Climate*, 24(1):49–67, 2011. ISSN 0894-8755. doi: 10.1175/2010JCLI3522.1. URL http://journals.ametsoc.org/doi/pdf/10.1175/2010JCLI3522.1{%}5Cnhttp://journals.ametsoc.org/doi/abs/10.1175/2010JCLI3522.1.

Nigro, M. A. and Cassano, J. J. Analysis of the Ross Ice Shelf Airstream Forcing Mechanisms Using Self-Organizing Maps. *Monthly Weather Review*, 142(12):4719–4734, 2014a.

Nigro, M. A. and Cassano, J. J. Identification of surface wind patterns over the Ross Ice Shelf, Antarctica using Self Organizing Maps. *Monthly Weather Review*, 140, 2014b.

Nigro, M. A., Cassano, J. J., and Seefeldt, M. W. A weather-pattern-based approach to evaluate the Antarctic Mesoscale Prediction System (AMPS) forecasts: Comparison to automatic weather station observations. *Weather and Forecasting*, 26(2):184–198, 2011.

Nigro, M. A., Cassano, J. J., and Knuth, S. L. Evaluation of Antarctic Mesoscale Prediction System (AMPS) cyclone forecasts using infrared satellite imagery. *Antarctic Science*, 24(02):183–192, 2012a. ISSN 1365-2079. doi: 10.1017/S0954102011000745. URL http://journals.cambridge.org/article{_}S0954102011000745.

Nigro, M. A., Cassano, J. J., Lazzara, M. A., and Keller, L. M. Case study of a barrier wind corner jet off the coast of the Prince Olav Mountains, Antarctica. *Monthly Weather Review*, 140 (7):2044–2063, 2012b.

O'Connor, W. P., Bromwich, D. H., and Carrasco, J. F. Cyclonically forced barrier winds along the Transantarctic Mountains near Ross Island. *Monthly weather review*, 122(1):137–150, 1994.

O'Connor, W. P. and Bromwich, D. H. Surface airflow around Windless Bight, Ross Island, Antarctica. *Quarterly Journal of the Royal Meteorological Society*, 114(482):917–938, 1988.

Organization, Z. S. ZigBee Specification, dec 2006.

Overland, J. E. and Walter, B. A. Gap Winds in the Strait of Juan de Fuca, 1981. ISSN 0027-0644. URL http://journals.ametsoc.org/doi/abs/10.1175/1520-0493(1981)109{%}3C2221:GWITSO{%}3E2.0.CO;2.

Parish, T. R. and Bromwich, D. H. The inversion wind pattern over West Antarctica. *Monthly weather review*, 114(5):849–860, 1986.

Parish, T. R. and Bromwich, D. H. The surface windfield over the Antarctic ice sheets. *Nature*, 328 (6125):51–54, 1987.

Parish, T. R. and Bromwich, D. H. Continental-scale simulation of the Antarctic katabatic wind regime. *Journal of Climate*, 4(2):135–146, 1991.

Parish, T. R. and Bromwich, D. H. On the forcing of seasonal changes in surface pressure. *Journal of geophysical research*, 102(D12):13–785, 1997.

Parish, T. R. and Bromwich, D. H. A Case Study of Antarctic Katabatic Wind Interaction with Large-Scale Forcing*. *Monthly weather review*, 126(1):199–209, 1998.

Parish, T. R. and Cassano, J. J. The role of katabatic winds on the Antarctic surface wind regime. *Monthly weather review*, 131(2):317–333, 2003.

Parish, T. R. Surface winds over the Antarctic continent: A review. *Reviews of Geophysics*, 26(1): 169–180, 1988.

Parish, T. R. On the Role of Antarctic Katabatic Winds in Forcing Large-Scale Tropospheric Motions, 1992. ISSN 0022-4928. URL http://journals.ametsoc.org/doi/abs/10.1175/1520-0469(1992)049{%}3C1374:OTROAK{%}3E2.0.CO;2?prevSearch={&}searchHistoryKey=.

Parish, T. R., Cassano, J. J., and Seefeldt, M. W. Characteristics of the Ross Ice Shelf air stream as depicted in Antarctic Mesoscale Prediction System simulations. *Journal of geophysical research*, 111(D12):D12109, 2006.

Parkinson, C. L. and Cavalieri, D. J. Antarctic sea ice variability and trends, 1979–2010. *The Cryosphere Discussions*, 6(2):931–956, 2012.

Perkins, C. E. and Royer, E. M. Ad hoc On-Demand Distance Vector Routing. In *Proc. 2nd IEEE Workshop on Mobile Computing Systems and Applications (WMCSA'99)*, New Orleans, LA, feb 1999.

Phillpot, H. R. and Zillman, J. W. The surface temperature inversion over the Antarctic continent. *Journal of Geophysical Research*, 75(21):4161–4169, 1970.

Pielke Sr, R. A. *Mesoscale meteorological modeling*, volume 98. Academic press, 2013.

Powers, J. G. Numerical prediction of an Antarctic severe wind event with the Weather Research and Forecasting (WRF) model. *Monthly Weather Review*, 135(9):3134–3157, 2007.

Powers, J. G., Manning, K. W., Bromwich, D. H., Cassano, J. J., and Cayette, A. M. A decade of Antarctic science support through AMPS. *Bulletin of the American Meteorological Society*, 2012.

Raphael, M. N., Marshall, G. J., Turner, J., Fogt, R. L., Schneider, D., Dixon, D. A., Hosking, J. S., Jones, J. M., and Hobbs, W. R. The Amundsen sea low: Variability, change, and impact on Antarctic climate. *Bulletin of the American Meteorological Society*, 97(1):111–121, 2016. ISSN 00030007. doi: 10.1175/BAMS-D-14-00018.1.

Renfrew, I. a. The dynamics of idealized katabatic flow over a moderate slope and ice shelf. *Quarterly Journal of the Royal Meteorological Society*, 130(598):1023–1045, 2004. ISSN 00359009. doi: 10.1256/qj.03.24. URL http://onlinelibrary.wiley.com/doi/10.1256/qj.03.24/abstract{%}5Cnhttp://doi.wiley.com/10.1256/qj.03.24.

Renfrew, I. A. and Anderson, P. S. The surface climatology of an ordinary katabatic wind regime in Coats Land, Antarctica. *Tellus, Series A: Dynamic Meteorology and Oceanography*, 54(5):463–484, 2002. ISSN 02806495. doi: 10.1034/j.1600-0870.2002.201397.x.

Reusch, D. B., Alley, R. B., and Hewitson, B. C. Relative performance of self-organizing maps and principal component analysis in pattern extraction from synthetic climatological data. *Polar Geography*, 29(3):188–212, 2005.

Riordan, A. J. Variations of Temperature and Air Motion in the 0- to 32- Meter Layer at Plateau Station, Antarctica. In Businger, J. A., editor, *Meteorological Studies at Plateau Station, Antarctica*, volume 25. American Geophysical Union, 1977.

Sammon, J. W. A nonlinear mapping for data structure analysis. *IEEE Transactions on computers*, 18(5):401–409, 1969.

Savage, M. L. and Stearns, C. R. Climate in the vicinity of Ross Island, Antarctica. *Antarct. JUS*, 20(1):1–9, 1985.

Schnell, R. C., Barry, R. G., Miles, M. W., Andreas, E. L., Radke, L. F., Brock, C. A., McCormick, M. P., and Moore, J. L. Lidar detection of leads in Arctic sea ice. *Nature*, 339(6225):530–532, 1989. ISSN 0028-0836. doi: 10.1038/339530a0. URL http://www.nature.com/doifinder/10.1038/339530a0.

Schwerdtfeger, W. *Weather and Climate of the Antarctic*. Elsevier, Amsterdam, 1984.

Scott, R. C. and Lubin, D. Mixed-phase cloud radiative properties over Ross Island , Antarctica : The influence of various synoptic-scale atmospheric circulation regimes. *Journal of Geophysical Research: Atmospheres*, 119(11):6702–6723, 2014. ISSN 21698996. doi: 10.1002/2013JD021132.

Scott, R. C. and Lubin, D. Unique manifestations of mixed-phase cloud microphysics over Ross Island and the Ross Ice Shelf, Antarctica. *Geophysical Research Letters*, pages 2936–2945, 2016. ISSN 19448007. doi: 10.1002/2015GL067246.

Seefeldt, M. W. and Cassano, J. J. An analysis of low-level jets in the greater Ross Ice Shelf region based on numerical simulations. *Monthly Weather Review*, 136(11):4188–4205, 2008.

Seefeldt, M. W., Tripoli, G. J., and Stearns, C. R. A high-resolution numerical simulation of the wind flow in the Ross Island region, Antarctica. *Monthly Weather Review*, 131(2):435–458, 2003.

Seefeldt, M. W., Cassano, J. J., and Parish, T. R. Dominant regimes of the Ross Ice Shelf surface wind field during austral autumn 2005. *Journal of Applied Meteorology and Climatology*, 46(11):1933–1955, 2007.

Seefeldt, M. W. and Cassano, J. J. A description of the Ross Ice Shelf air stream (RAS) through the use of self-organizing maps (SOMs). *Journal of Geophysical Research: Atmospheres (1984–2012)*, 117(D9), 2012.

Sensiron. Datasheet SHT7x. Technical report, Sensiron, 2011.

Sheridan, S. C. and Lee, C. C. The self-organizing map in synoptic climatological research. *Progress in Physical Geography*, 35(1):109–119, 2011. ISSN 0309-1333. doi: 10.1177/0309133310397582.

Sinclair, M. R. Local topographic influence on low-level wind at Scott Base, Antarctica. *New Zealand Journal of Geology and Geophysics*, 31(2):237–245, 1988. ISSN 0028-8306. doi: 10.1080/00288306.1988.10417772. URL http://www.tandfonline.com/doi/abs/10.1080/00288306.1988.10417772.

Smith, S. D., Anderson, R. J., Hartog, G. D., Topham, D. R., and Perkin, R. G. An investigation of a polynya in the Canadian Archipelago: 1. Introduction and oceanography. *Journal of Geophysical Research: Oceans*, 88(C5):2900, 1983. ISSN 0148-0227. doi: 10.1029/JC088iC05p02888. URL http://doi.wiley.com/10.1029/JC088iC05p02888.

Steinhoff, D. F., Bromwich, D. H., Lambertson, M., Knuth, S. L., and Lazzara, M. A. A Dynamical Investigation of the May 2004 McMurdo Antarctica Severe Wind Event Using AMPS*. *Monthly Weather Review*, 136(1):7–26, 2008.

Steinhoff, D. F., Chaudhuri, S., and Bromwich, D. H. A Case Study of a Ross Ice Shelf Airstream Event: A New Perspective*. *Monthly Weather Review*, 137(11):4030–4046, 2009.

Talzi, I., Hasler, A., Gruber, S., and Tschudin, C. PermaSense: investigating permafrost with a WSN in the Swiss Alps. In *Proceedings of the 4th workshop on Embedded networked sensors*, pages 8–12. ACM, 2007.

Taylor, K. E. Summarizing multiple aspects of model performance in a single diagram. *Journal of Geophysical Research: Atmospheres (1984–2012)*, 106(D7):7183–7192, 2001.

Tietäväinen, H. and Vihma, T. Atmospheric moisture budget over Antarctica and the Southern Ocean based on the ERA-40 reanalysis. *International Journal of Climatology*, 1995(March): 1977–1995, 2008. ISSN 1476-4687. doi: 10.1002/joc. URL http://cdiac.esd.ornl.gov/oceans/GLODAP/glodap{_}pdfs/Thermohaline.web.pdfhttp://dx.doi.org/10.1002/joc.1684.

van den Broeke, M. R. and van Lipzig, N. P. M. Factors Controlling the Near-Surface Wind Field in Antarctica*. *Monthly Weather Review*, 131(4):733–743, 2003. ISSN 0027-0644. doi: 10.1175/1520-0493(2003)131<0733:FCTNSW>2.0.CO;2.

Vaughan, M. A., Young, S. A., Winker, D. M., Powell, K. A., Omar, A. H., Liu, Z., Hu, Y., and Hostetler, C. A. Fully automated analysis of space-based lidar data: an overview of the CALIPSO retrieval algorithms and data products. *Proceedings of SPIE - The International Society for Optical Engineering*, 5575:16–30, 2004. ISSN 0277786X. doi: 10.1117/12.572024. URL http://www.scopus.com/inward/record.url?eid=2-s2.0-17644425718{&}partnerID=tZOtx3y1.

Verlinden, K. L., Thompson, D. W. J., and Stephens, G. L. The Three-Dimensional Distribution of Clouds over the Southern Hemisphere High Latitudes. *Journal of Climate*, 24(22):5799–5811, 2011. ISSN 0894-8755. doi: 10.1175/2011JCLI3922.1. URL http://journals.ametsoc.org/doi/abs/10.1175/2011JCLI3922.1.

Walter, B. A. A study of the planetary boundary-layer over the polynya downwind of St-Lawrence Island in the Bering Sea using aircraft data. *Boundary-Layer Meteorology*, 48(3):255–282, 1989. doi: 10.1007/BF00158327.

Wilson, A. B., Bromwich, D. H., and Hines, K. M. Evaluation of polar WRF forecasts on the arctic system reanalysis domain: 2. Atmospheric hydrologic cycle. *Journal of Geophysical Research Atmospheres*, 117(4):1–20, 2012. ISSN 01480227. doi: 10.1029/2011JD016765.

Zwally, H. J., Comiso, J. C., and Gordon, A. L. Antarctic offshore leads and polynyas and oceanographic effects. *Oceanology of the Antarctic Continental Shelf*, 43:203–226, 1985. doi: 10.1029/AR043p0203. URL http://www.agu.org/books/ar/v043/AR043p0203/AR043p0203.shtml.

Zwally, H. J., Comiso, J. C., Parkinson, C. L., Cavalieri, D. J., and Gloersen, P. Variability of Antarctic sea ice 1979–1998. *Journal of Geophysical Research: Oceans (1978–2012)*, 107(C5):1–9, 2002.